Quantum computation: algorithms and implementation in quantum dot devices

by

John King Gamble

A dissertation submitted in partial fulfillment of
the requirements for the degree of

Doctor of Philosophy
(Physics)

at the
University of Wisconsin – Madison
2013

Defended on 10 May 2013
Dissertation approved by the following members of the Final Oral Committee:

Susan N. Coppersmith · Professor of Physics
Mark G. Friesen · Senior Scientist of Physics
Mark A. Eriksson · Professor of Physics
Robert J. Joynt · Professor of Physics
Irena Knezevic · Associate Professor of
Electrical and Computer Engineering

Abstract

In this thesis, we explore several aspects of both the software and hardware of quantum computation. First, we examine the computational power of multi-particle quantum random walks in terms of distinguishing mathematical graphs. We study both interacting and non-interacting multi-particle walks on strongly regular graphs, proving some limitations on distinguishing powers and presenting extensive numerical evidence indicative of interactions providing more distinguishing power. We then study the recently proposed adiabatic quantum algorithm for Google PageRank, and show that it exhibits power-law scaling for realistic WWW-like graphs.

Turning to hardware, we next analyze the thermal physics of two nearby 2D electron gas (2DEG), and show that an analogue of the Coulomb drag effect exists for heat transfer. In some distance and temperature, this heat transfer is more significant than phonon dissipation channels. After that, we study the dephasing of two-electron states in a single silicon quantum dot.Specifically, we consider dephasing due to theelectron-phonon coupling andcharge noise, separately treating orbital and valley excitations. In an ideal system, dephasing due to charge noise is strongly suppressed due to a vanishing dipole moment. However, introduction of disorder or anharmonicity leads to large effective dipole moments, and hence possibly strong dephasing.

Building on this work, we next consider more realistic systems, including structural disorder systems. We present experiment and theory, which demonstrate energy levels that vary with quantum dot translation, implying a structurally disordered system. Finally, we turn to the issues of valley mixing and valley-orbit hybridization, which occurs due to atomic-scale disorder at quantum well interfaces. We develop a new theoretical approach to study these effects, which we name the disorder-expansion technique. We demonstrate that this method successfully reproduces atomistic tight-binding techniques, while using a fraction of the computational resources and providing considerably more physical insight. Using this technique, we demonstrate that large dipole moments can exist between valley states in disordered systems, and calculate corrections to intervalley tunnel rates.

Acknowledgements

This thesis and the degree it represents would not have been possible without the help and support of countless individuals. I would like to express my gratitude first for the support and guidance of my advisors, Prof. Susan Coppersmith and Dr. Mark Friesen. Ever since I started working with her the summer before my first year in graduate school, Sue has been a constant source of inspiration and an excellent guide to the maze of academia. Likewise, Mark has spent many hours patiently scrutinizing my work and making me think more rigorously, for which I am especially grateful. Mark is responsible for teaching me valley physics, which was and continues to be one of my most fruitful research topics. Without Sue and Mark's frequent guidance, many of the ideas in this thesis would have been left only half-developed. I hope that I will continue to collaborate frequently with both of them in the future.

I offer sincere thanks to Prof. Mark Eriksson, who, besides being a frequent collaborator, has generously offered me much advice and guidance, even though I wasn't his advisee. Mark has facilitated a large amount of theory-experiment cross-collaboration, which was one of the most rewarding parts of my graduate school experience. I also extend my thanks to my other collaborators for their efforts and assistance. On the theory side, I have greatly appreciated large collaborations with Kenneth Rudinger, Xuedong Hu, and Teck Seng Koh. Further, I owe a big debt to the long hours put in by my main experimental collaborators, Zhan Shi, Dan Ward, Xian Wu, and Robert Mohr.

I would like to express my appreciation to my thesis committee, Prof. Susan Coppersmith, Dr. Mark Friesen, Prof. Mark Eriksson, Prof. Robert Joynt, and Prof. Irena Knezevic, for their time and care with my thesis and the final portion of my PhD.

Of course, I could not have completed this thesis without the support from my friends and family. My wife Katherine has been an indomitable source of love and support, and I am and forever will be grateful to have her in my life. My parents, John and Clare, have always been there for me, especially in stressful times. My parents-in-law, Jonathan and Patricia, have become close family to me in the last few years, and have offered me support

and advice for almost the past decade. My brother- and sister-in-law, Tim and Lisa, are quickly becoming the siblings I never had, and for that I am grateful. Finally, I would like to thank my grandmothers Mary and Agnes, who sadly passed away during my graduate studies. I was truly blessed to have them both in my life for as long as I did.

Next year, Katherine and I will head to Albuquerque, NM, where I will start as a Harry S. Truman Fellow at Sandia National Laboratories in the Fall. We will both miss Madison greatly - we have made many wonderful friends and many great memories here.

I dedicate this thesis to Mary Brickman Gamble, my grandmother, who died a little over two years ago. She was ever a source of inspiration for me, and I will always be grateful for my memories of her.

Contents

List of Figures

List of Tables

Chapter 1

Introduction

Quantum computers have the capability to revolutionize the computation landscape in ways that incremental improvements to conventional computers cannot achieve. In order for quantum computation to make an impact, advances must be made at both the software and hardware level; we need both effective quantum algorithms and a machine on which to run them.

To that end, this thesis consists of two major parts. The first part, comprising of the first three chapters, discusses some advances in quantum algorithms, with a particular focus on developing algorithms beyond the circuit model. These alternative approaches to quantum information processing can prove valuable since certain computational problems, especially those that involve mathematical graphs, are much more easily expressed using them than the circuit approach. In particular, we examine the computational power of a many-body quantum random walk formalism, and investigate aspects of the quantum adiabatic algorithm.

The second part, consisting of the next four chapters, discusses practical issues that arise when we attempt to implement the hardware of a quantum computer. Although researchers have had recent success with small-scale devices in many architectures, the largest universal quantum computer demonstrated to date consists of 14 qubits [1], compared to the billions of bits found in classical computers. It is clear that, for quantum computers to have an impact,

they must be massively scaled up. Barriers to achieving this breakthrough are essentially the same across all architectures: disorder and imperfections in real physical systems ruin the idealized proposals to build a scalable quantum computer. In semiconducting architectures [2], due to the huge amount of infrastructure support, working around or eliminating this disorder is one of the main roadblocks to scalable systems. Therefore, it is vitally important to thoroughly understand the physics of the semiconductor systems that would host these qubits. The majority of the work done in this part has an emphasis on Si quantum dot devices, but some applies to other semiconductor systems or general heterostructures, as well.

1.1 Thesis outline

First, in chapter 2, we show that the quantum dynamics of interacting and noninteracting quantum particles are fundamentally different in the context of solving a particular computational problem. Specifically, we consider the graph isomorphism problem, in which one wishes to determine whether two graphs are isomorphic (related to each other by a relabeling of the graph vertices), and focus on a class of graphs with particularly high symmetry called strongly regular graphs (SRG's). We study the Green's functions that characterize the dynamical evolution single-particle and two-particle quantum walks on pairs of non-isomorphic SRG's and show that interacting particles can distinguish non-isomorphic graphs that noninteracting particles cannot. We obtain the following specific results: (1) We prove that quantum walks of two noninteracting particles, Fermions or Bosons, cannot distinguish certain pairs of non-isomorphic SRG's. (2) We demonstrate numerically that two interacting Bosons are more powerful than single particles and two noninteracting particles, in that quantum walks of interacting bosons distinguish all non-isomorphic pairs of SRGs that we examined. By utilizing high-throughput computing to perform over 500 million direct comparisons between evolution operators, we checked all tabulated pairs of non-isomorphic SRGs, including graphs with up to 64 vertices. (3) By performing a short-time expansion of the evolution operator, we derive distinguishing operators that provide

analytic insight into the power of the interacting two-particle quantum walk.

Next, in chapter 3 we extend the results of chapter 2 by focussing on quantum random walks of multiple non-interacting particles on SRGs. Here, we demonstrate numerically that three-particle non-interacting quantum walks have significant, but not universal, distinguishing power for pairs of SRGs, proving a fundamental difference between the distinguishing power of two-particle and three-particle non-interacting walks. We analytically show why this distinguishing power is possible, whereas it is forbidden for two-particle non-interacting walks. Based on sampling of SRGs with up to 64 vertices, we find no difference in the distinguishing power of bosonic and fermionic walks. In addition, we find that the four-fermion non-interacting walk has greater distinguishing power than the three-particle walks on SRGs, showing that increasing particle number increases distinguishing power. However, we also analytically show that no non-interacting walk with a fixed number of particles can distinguish all SRGs, thus demonstrating a potential fundamental difference between the distinguishing power of interacting and noninteracting walks.

In chapter 4, we move from quantum random walks to the quantum adiabatic algorithm, by considering an important method for search engine result ranking thatworks by finding the principal eigenvector of the "Google matrix." Recently, a quantum algorithm for preparing this eigenvector and evidence of an exponential speedup for some scale-free networks were presented. Here, we show that the run-time depends on features of the graphs other than the degree distribution, and can be altered sufficiently to rule out a general exponential speedup. For a sample of graphs with degree distributions that more closely resemble the Web than in previous work, the proposed algorithm for eigenvector preparation does not appear to run exponentially faster than the classical case.

In chapter 5, we change topics to quantum computer implementation, and address the issue of heat dissipation in current-carrying cryogenic nanostructures, which is problematic because the phonon density of states decreases strongly as energy decreases. There, we show that the Coulomb interaction can prove a valuable resource for carrier cooling via coupling to a nearby, cold electron reservoir. Specifically, we consider the geometry of an

electron bilayer in a silicon-based heterostructure, and analyze the power transfer. We show that across a range of temperatures, separations, and sheet densities, the electron-electron interaction dominates the phonon heat-dissipation modes as the main cooling mechanism. Coulomb cooling is most effective at low densities, when phonon cooling is least effective in silicon, making it especially relevant for experiments attempting to perform coherent manipulations of single spins.

In chapter 6, we study the dephasing of two-electron states in a single quantum dot in both GaAs and Si. We investigate dephasing induced by electron-phonon coupling and by charge noise analytically for pure orbital excitations in GaAs and Si, as well as for pure valley excitations in Si. In GaAs, polar optical phonons give rise to the most important contribution, leading to a typical dephasing rate of $\sim$ 5.9 GHz. For Si, intervalley optical phonons lead to a typical dephasing rate of $\sim$ 140 kHz for orbital excitations and $\sim$ 1.1 MHz for valley excitations. For harmonic, disorder-free quantum dots, charge noise is highly suppressed for both orbital and valley excitations, since neither has an appreciable dipole moment to couple to electric field variations from charge fluctuators. However, both anharmonicity and disorder break the symmetry of the system, which can lead to increased dipole moments and therefore faster dephasing rates.

In chapter 7, we measure the excited-state spectrum of a Si/SiGe quantum dot as a function of in-plane magnetic field and identify the spin of the lowest three eigenstates in an effective two-electron regime. We extract the singlet-triplet splitting, an essential parameter for spin qubits, from the data, and we find it to be tunable by lateral displacement of the dot, which is realized by changing two gate voltages on opposite sides of the device. We present calculations showing the data are consistent with a spectrum in which the first excited state of the dot is a valley-orbit state.

In chapter 8, we introduce a novel, systematic effective mass theory of valley-orbit coupling in disordered silicon systems. This theory successfully reproduces the results of atomistic tight-binding theories, while being much less computationally intensive and retaining the appealing physical intuition of effective mass models. This theory reveals

valley-orbit hybridization effects that are detrimental for storing quantum information in the valley degree of freedom, including non-vanishing dipole matrix elements between valley states and altered intervalley tunneling. These effects have ramifications for recent proposals for encoding quantum information in the valley degree of freedom.

Finally, in chapter 9 we offer concluding remarks.

1.2 Publications

Each of the main chapters in this thesis is based one either published or submitted work, each of which represents the work of many individuals. Here, I document my contribution to each work, as well as my collaborators.

Chapter 2 is based on Ref. [3], titled *Two-particle quantum walks applied to the graph isomorphism problem*, which I completed with Dr. Mark Friesen, Dr. Dong Zhou, Prof. Robert Joynt, and Prof. Susan Coppersmith. I carried out the analytic proofs and numerical calculations, and was assisted by Dr. Friesen, Dr. Zhou, Prof. Joynt, and Prof. Coppersmith.

Chapter 3 is based on Ref. [4], titled *Noninteracting multiparticle quantum random walks applied to the graph isomorphism problem for strongly regular graphs*, which I completed with Mr. Kenneth Rudinger, Mr. Mark Wellons, Prof. Eric Bach, Dr. Mark Friesen, Prof. Robert Joynt, and Prof. Susan Coppersmith. Mr. Rudinger and I jointly did the main analytic work on the paper, assisted by the other authors. Mr. Rudinger principally carried out the numerical work, assisted by me and the other authors.

Chapter 4 is based on Ref. [5], titled *Power law scaling for the adiabatic algorithm for search engine ranking*, which I completed with Mr. Adam Frees, Mr. Kenneth Rudinger, Prof. Eric Bach, Dr. Mark Friesen, Prof. Robert Joynt, and Prof. Susan Coppersmith. Mr. Frees principally carried out the numerical calculations with my guidance and direction, and with assistance from the other authors.

Chapter 5 is based on Ref. [6], titled *Cooling of cryogenic electron bilayers via the Coulomb interaction*, which I completed with Dr. Mark Friesen, Prof. Robert Joynt, and

Prof. Susan Coppersmith. Prof. Coppersmith originated the idea, and I carried out the calculations with much assistance and guidance from Dr. Friesen, Prof. Joynt, and Prof. Coppersmith.

Chapter 6 is based on Ref. [7], titled *Two-electron dephasing in single Si and GaAs quantum dots*, which I completed with Dr. Mark Friesen, Prof. Susan Coppersmith, and Prof. Xuedong Hu. The work was motivated by a need to characterize the decoherence in the new qubit architecture that we introduced in Ref. [8]. I performed the calculations with assistance and guidance from Dr. Friesen, Prof. Coppersmith, and Prof. Hu.

Chapter 7 is based on Ref. [9], titled *Tunable singlet-triplet splitting in a few-electron Si/SiGe quantum dot*, which I completed with Ms. Zhan Shi, Dr. Christine Simmons, Dr. Jonathan Prance, Dr. Mark Friesen, Dr. Don Savage, Prof. Max Lagally, Prof. Susan Coppersmith, and Prof. Mark Eriksson. Ms. Shi, Dr. Simmons, Dr. Prance, and Prof. Eriksson performed the experiment, Dr. Savage and Prof. Lagally grew the samples, and I performed the theoretical simulations with help and assistance from Dr. Friesen and Prof. Coppersmith.

Chapter 8 is based on work to be submitted, titled *Disorder-induced valley-orbit hybrid states in Si quantum dots*, which I completed with Prof. Mark Eriksson, Prof. Susan Coppersmith, and Dr. Mark Friesen. I developed the disorder-expansion technique used in this chapter and performed the calculations, based on the extensive studies of valley-orbit coupling carried out primarily by Dr. Friesen, and assisted by Prof. Eriksson and Prof. Coppersmith.

Chapter 2

Two-particle quantum walks applied to the graph isomorphism problem

2.1 Introduction

Random walks have been applied successfully to many problems in physics, as well as in many other disciplines, stretching from biology to economics [10, 11, 12, 13, 14]. Most of these applications use classical random walks (CRWs), in which quantum mechanical principles are not considered. However, more recently, researchers have found that CRWs and quantum random walks (QRWs) can exhibit qualitatively different properties [15, 16, 17]. From a standpoint of algorithms research, these disparities lead to situations in which algorithms implemented by QRWs can be proven to run faster than the fastest possible classical algorithm [18, 19, 20, 21, 22, 23, 24].

Besides being useful as theoretical models, simple QRWs have already been experimentally implemented in externally driven cavities [25], arrays of optical traps [26, 27], NMR systems [28], and ion traps [29, 30]. This, coupled with new ideas for realistic physical implementations of non-trivial walks [31], indicates that studying algorithms cast as QRWs

might lead to algorithms that are both powerful and experimentally viable.

Although QRWs are universal and therefore in principle can be used to implement any quantum algorithm [32], in practice some information-theoretic problems lend themselves to a QRW approach more easily than others. Many of the problems that have been investigated are expressed naturally using graphs, sets of vertices and edges, with each edge connecting two vertices. For example, the vertices of a graph might be taken to represent individuals, and the edges between them might indicate friendship. A question one could ask is whether there is a subset of friends that are isolated from the rest of the group, which translates to the graph-theoretic question of whether the graph is disconnected. Once the question to be answered is posed as a question about a graph, it is investigated by constructing a quantum Hamiltonian from that graph. The dynamics of the system is then analyzed using quantum mechanics, and is used to make statements about the original graph, hopefully giving insight to the answer of the original problem.

This chapter addresses the graph isomorphism (GI) problem, where, given two graphs, one must determine whether or not they are isomorphic (two graphs are isomorphic if one can be obtained from the other by a relabeling of the vertices). Although many special cases of GI have been shown to solvable in a time that scales as a polynomial of the number of vertices, the best general classical algorithm to date runs in time $\mathcal{O}\left(c^{N^{1/2}\log N}\right)$, where c is a constant and N is the number of vertices in the graphs being compared [33].

GI has several properties analogous to those of factoring. First, though it appears to be difficult, it is felt that it is unlikely to be NP-complete, since otherwise many complexity classes believed to be distinct would collapse.[1] Second, both GI and factoring can be viewed as hidden subgroup problems. In GI, one is looking for a hidden subgroup of the permutation group, while in factoring, one is looking for a hidden subgroup of the Abelian group. The success of Shor's polynomial-time algorithm for factoring [35] has led several groups to investigate a hidden-subgroup approach to GI. However, the obstacles facing such an approach have been shown to be formidable [36, 37].

[1] Specifically, it has been shown that graph isomorphism were NP-complete, the polynomial hierarchy collapses to level two [34].

Researchers have also recently attacked GI using various methods inspired by physical systems. Rudolph mapped the GI problem onto a system of hard-core atoms [38]. One atom was used per vertex, and atoms i and j interacted if vertices i and j were connected by edges. He showed that pairs of non-isomorphic graphs exist whose original adjacency matrices have the same eigenvalues, while the induced adjacency matrices describing transitions between three-particle states have different eigenvalues. Gudkov and Nussinov proposed a physically-motivated classical algorithm to distinguish non-isomorphic graphs [39]. Shiau *et al.* proved that the simplest classical algorithm fails to distinguish some pairs of non-isomorphic graphs [40] and also proved that continuous-time one-particle QRWs cannot distinguish some non-isomorphic graphs [40]. Douglas and Wang modified a single-particle QRW by adding phase inhomogeneities, altering the evolution as the particle walked through the graph [41]. Their approach was powerful enough to successfully distinguish many families of graphs considered to be difficult to distinguish, including all families of strongly regular graphs they tried. Most recently, Emms *et al.* used discrete-time QRWs to build potential graph invariants [42, 43]. Through numerical spectral analysis, they found that these invariants could be used to distinguish many types of graphs by breaking the eigenvalue degeneracies of many families of graphs that are difficult to distinguish.

In addition to studying single-particle QRWs, Shiau et al. [40] performed numerical investigations of two-particle QRWs and presented evidence that interacting Bosons can distinguish non-isomorphic pairs that single-particle walks cannot. There, it was also found numerically that two-Boson QRWs with noninteracting particles do not distinguish some non-isomorphic pairs of graphs. In contrast to the approaches in [41, 42, 43], the two-particle QRW algorithm does not lower the symmetry of the system.

In this chapter, we extend the results in [40] on two-particle quantum walks in several ways. First, we prove analytically that quantum walks of two non-interacting Bosons always fail to distinguish non-isomorphic pairs of strongly regular graphs (SRGs). This result is surprising, since it has been shown in [44, 45, 46] that non-interacting Boson QRWs on graphs can give rise to effective statistical interactions, which significantly alter the

dynamics of the system. Second, we show that analysis of the behavior of non-interacting Fermions requires a more subtle treatment than was done in [40]; the result in [40] that some non-isomorphic SRGs could be distinguished by two noninteracting Fermions and not by two noninteracting Bosons arose because of an ambiguity in the choice of basis. When the ambiguities involved with the basis choice for Fermions are accounted for, non-interacting Fermions fail to have any advantage over non-interacting Bosons. Third, we expand on the initial numerical results in [40], exhaustively verifying, where only sampling was used before, that two-particle interacting Boson walks distinguish all the non-isomorphic pairs of SRGs with up to 64 vertices that have been tabulated. To accomplish this, we used high-throughput computing techniques to perform over 500 million comparisons between evolution operators of graphs. Finally, we examine the small-time expansion of the evolution operator, and use the two-particle interacting evolution to derive candidates for graph invariants, which appear in the fourth and sixth orders in time.

Our results demonstrate unambiguously that two-particle Bosonic quantum walks have more computational power if the particles are interacting, because interacting walks can be used to distinguish non-isomorphic graphs that noninteracting particles cannot.

The chapter is organized as follows. Section 2.2 introduces relevant background and definitions to QRWs on graphs, including a brief overview of the strongly regular graphs (SRGs) on which the algorithms are tested and also a review of the one-particle QRW algorithm considered in [40]. Section 2.3 proves that QRWs of two non-interacting Bosons do not distinguish non-isomorphic SRGs with the same family parameters. Section 2.4 analyzes the QRW of two non-interacting Fermions. It shows that improper basis choice can lead to false-distinguishing, and that when the basis is chosen consistently, QRWs with two noninteracting fermions are unable to distinguish some pairs of non-isomorphic SRGs. Section 2.5 shows through exhaustive simulation that all tabulated families of SRGs are successfully distinguished by a two hard-core Boson QRW. In section 2.6 a short-time expansion of the evolution operator is computed, and distinguishing operators present in the two hard-core Boson QRW are identified. Finally, Section 2.7 summarizes and discusses the

possible implications of our results for the development of algorithms based on interacting QRWs for distinguishing non-isomorphic graphs.

2.2 Background & Definitions

This section describes the background and definitions necessary to study QRWs on graphs. First, we introduce the graph-theoretic concepts we will need, including the notions of of the adjacency matrix and the spectrum of a graph. Then, we consider how to use these tools to construct a physical process through the definition of Hamiltonian and Green's functions, for both one and two particles. Next, we detail the relevant properties of SRGs. Finally, we review the method used in [40] to use the properties of SRGs to show that the Green's functions of single-particle QRWs do not distinguish non-isomorphic SRGs with the same family parameters.

Constructing walks on graphs

In this section, we describe how to form QRWs on graphs. A graph $G = (V, E)$ is a set vertices V and edges E. The vertices are usually labeled by integer indices, and the edges are unordered pairs of vertices. Two vertices that share an edge are called *connected*, while two vertices that do not are called *disconnected*. The total number of neighboring vertices of a particular vertex is called its *degree*. For example, the graph $G = (\{1, 2, 3, 4\}, \{(1, 2), (2, 3), (3, 4), (4, 1)\})$ is a cycle graph with four vertices. Two graphs are *isomorphic* if they can be made identical by relabeling their vertices. For example, the graph $H = (\{1, 2, 3, 4\}, \{(1, 3), (3, 2), (2, 4), (4, 1)\})$ is isomorphic to G, since after relabeling $2 \leftrightarrow 3$, the two graphs are equivalent.

Graphs are conveniently expressed algebraically as *adjacency matrices*. An adjacency matrix A of a graph with N vertices is an $N \times N$ matrix in the basis of vertex labels, with $A_{ij} = 1$ if vertices i and j are connected by an edge, and zero otherwise. The adjacency

matrix for the graph G is

$$\mathbf{A}_G = \begin{pmatrix} 0 & 1 & 0 & 1 \\ 1 & 0 & 1 & 0 \\ 0 & 1 & 0 & 1 \\ 1 & 0 & 1 & 0 \end{pmatrix}. \tag{2.1}$$

The *spectrum* of a graph is the eigenvalue spectrum of its adjacency matrix. The spectrum of G is $\{-2, 0, 2\}$, with 0 two-fold degenerate.

To form a QRW on a graph, we first define a Hamiltonian. We will use the Hubbard model, with each site corresponding to a graph vertex. A particle can make a transition between two sites if the associated vertices are connected. In addition, if two walkers happen to simultaneously occupy a site, we impose a double-occupation energy cost U. Our Hamiltonian is

$$\mathbf{H} = -\sum_{i,j} A_{ij} c_i^\dagger c_j + \frac{U}{2} \sum_i \left(c_i^\dagger c_i\right)\left(c_i^\dagger c_i - 1\right), \tag{2.2}$$

where c and $c^\dagger$ are Boson or (spinless) Fermion creation and annihilation operators. If we restrict ourselves to single-particle states, we find matrix elements

$$\langle i| \mathbf{H} |j\rangle = -A_{ij}. \tag{2.3}$$

Hence, we can easily identify the a single-particle Hamiltonian

$$\mathbf{H}_{1P} = -\mathbf{A}. \tag{2.4}$$

Similarly, we can define two-particle Hamiltonians by their matrix elements. For these, we need to use either Bosonic or Fermionic basis states. The Boson states are

$$|ij\rangle_B \equiv \begin{cases} \frac{1}{\sqrt{2}} \left(|ij\rangle + |ji\rangle\right) & : i \neq j \\ |ii\rangle & : i = j \end{cases} \tag{2.5}$$

and the Fermion states are

$$|ij\rangle_F \equiv \frac{1}{\sqrt{2}} \left(|ij\rangle - |ji\rangle\right). \tag{2.6}$$

We now restrict ourselves to two particles, where we define $\mathbf{H}_{2B}$ and $\mathbf{H}_{2F}$ to be the two-particle Boson and Fermion Hamiltonians. These are special cases of eq. 2.2, with matrix elements

$$
\begin{aligned}
{}_B\langle ij|\mathbf{H}_{2B}\,|kl\rangle_B &\equiv {}_B\langle ij|\mathbf{H}\,|kl\rangle_B \qquad (2.7)\\
&= \begin{cases} -\delta_{ik}A_{jl} - \delta_{jl}A_{ik} - \delta_{il}A_{jk} - \delta_{jk}A_{il} & : \ i \neq j \text{ and } k \neq l \\ U\delta_{ik} & : \ i = j \text{ and } k = l \\ \frac{-1}{\sqrt{2}}\left(\delta_{ik}A_{jl} + \delta_{jl}A_{ik} + \delta_{il}A_{jk} + \delta_{jk}A_{il}\right) & : \ i = j \text{ xor } k = l \end{cases},\\
{}_F\langle ij|\mathbf{H}_{2F}\,|kl\rangle_F &\equiv {}_F\langle ij|\mathbf{H}\,|kl\rangle_F \qquad (2.8)\\
&= A_{ik}\delta_{jl} + A_{jl}\delta_{ik} - A_{il}\delta_{jk} - A_{jk}\delta_{il} \quad : \ i \neq j \text{ and } k \neq l,
\end{aligned}
$$

respectively, where the matrix elements are found directly from Eq. 2.2 through the application of appropriate commutation relations.

From each of these Hamiltonians, we define the QRW time-evolution operator as

$$\mathbf{U} = e^{-it\mathbf{H}}, \qquad (2.9)$$

where we set $\hbar = 1$ for notational convenience.

To study the dynamics of the system, we define the two-particle Green's function (GF), which relates the wavefunctions at a time t to those at time $t = 0$. For two-particle position states $|\psi\rangle$ and $|\psi'\rangle$, it is

$$\mathcal{G}\left(\psi(0), \psi'(t)\right) = \left\langle \psi(0) \middle| \psi'(t) \right\rangle = \langle\psi(0)|\,\mathbf{U}\,|\psi'(0)\rangle\,. \qquad (2.10)$$

Letting (ψ, ψ') run over a complete two-particle basis, $\mathcal{G}(\psi(0), \psi'(t))$ considered at a fixed time provides us with a set of $N^2(N+1)^2/4$ complex numbers for Bosons or $N^2(N-1)^2/4$ complex numbers for Fermions. These lists completely characterizes the dynamics of the system. Hence, when we analyze QRWs, we say that a particular scheme *distinguishes* two graphs if their Green's functions supply us with two different lists.

Strongly Regular Graphs

Our major results in this chapter focus on algorithms over strongly regular graphs (SRGs), which are difficult to distinguish. In this section, we develop the properties of SRGs we will need for our later analysis.

A SRG is a graph in which (a) all vertices have the same degree, (b) each pair of neighboring vertices has the same number of shared neighbors, and (c) each pair of non-neighboring vertices has the same number of shared neighbors. This definition permits SRGs to be categorized into families by four integers (N, k, λ, μ), each of which might contain many non-isomorphic members. Here, N is the number of vertices in each graph, k is the degree of each vertex (k-regularity), λ is the number of of common neighbors shared by each pair of adjacent vertices, and μ is the number common neighbors shared by each pair of non-adjacent vertices.

Using the stringent constraints placed on SRGs, one can show that, regardless of size, the spectrum of any SRG only has three distinct values [47]:

$$\lambda_0 = -k, \tag{2.11}$$

which is non-degenerate, and

$$\lambda_{1,2} = -\frac{1}{2}\left(\lambda - \mu \pm \sqrt{N}\right), \tag{2.12}$$

which are both highly degenerate. Both the value and degeneracy of these eigenvalues depend only on the family parameters, so within a particular SRG family, all graphs are cospectral [47]. Further, the spectra of the two-particle Hamiltonians formed from SRG adjacency matrices, as described in Eq. 2.7, are also highly degenerate. As shown in figure 2.1 for the family (16,6,2,2), the interacting case gives us the largest number of distinct energy levels. These highly degenerate spectra are one reason why distinguishing non-isomorphic SRGs is difficult—it is known that distinguishing non-isomorphic graphs with spectra with bounded degeneracy can be done with polynomially bounded resources [48].

The adjacency matrix of any SRG satisfies the useful relation [47]:

$$\mathbf{A}^2 = (k - \mu)\mathbf{I} + \mu\mathbf{J} + (\lambda - \mu)\mathbf{A}, \tag{2.13}$$

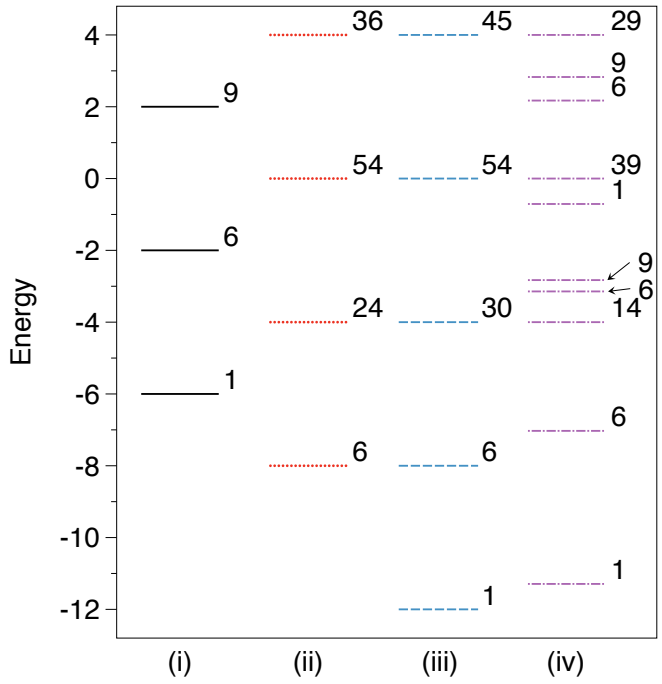

Figure 2.1: The energy spectra for (i) one particle, (ii) two non-interacting Fermion, (iii) two non-interacting Boson, and (iv) two hard-core Boson QRWs on the SRG family (16,6,2,2). Here, the units are the physical coupling between nodes, which is set to one in the text for simplicity. The parameters (N, k, λ, μ) define an individual SRG family, where N is the number of vertices in each graph, k is the degree of each vertex (k-regularity), λ is the number of of common neighbors shared by each pair of adjacent vertices, and μ is the number common neighbors shared by each pair of non-adjacent vertices. Both graphs in the family have the same spectra. In all four panels, the Hamiltonian used is the Hubbard model (eq. 2.2), with $U = 0$ in the noninteracting cases and $U \to \infty$ for the hard-core Bosons. The degeneracies are given to the right of each level.

where $\mathbf{I}$ is the identity and $\mathbf{J}$ is the matrix of all ones ($J_{ij} = 1$ for all i, j). Since $\mathbf{J}^2 = N\mathbf{J}$ and $\mathbf{I}^2 = \mathbf{I}$, this forms a three-dimensional algebra, and we can write

$$\mathbf{A}^n = \alpha_n \mathbf{I} + \beta_n \mathbf{J} + \gamma_n \mathbf{A}, \tag{2.14}$$

where α, β, and γ are functions only of the family parameters. That is, all SRGs of the same family have the same coefficients.

Although many SRGs are known [49], there are substantially fewer tabulated families with more than one non-isomorphic member. Complete and partial families of SRGs have

been tabulated through combinatorial techniques [50, 51], which we use in sec. 2.5 to perform numerical tests of our algorithms.

Review of one-particle algorithm

In this section, we review the method used in Ref. [40] to prove that a single-particle QRW cannot distinguish non-isomorphic members of SRG families. Formally, this means that we must show that any two SRGs of the same family parameters have the same single-particle Green's functions $\mathcal{G}_{1P}$.

First, we consider the adjacency matrix $\mathbf{A}$, and suppose it belongs to the strongly regular graph family (N, k, λ, μ). Then, by Eq. 2.4, we know that the single-particle hamiltonian is $\mathbf{H}_{1P} = -\mathbf{A}$, and so by Eq. 2.9, the QRW evolution operator is $\mathbf{U}_{1P} = e^{it\mathbf{A}}$. But since $\mathbf{A}$ is a SRG, we make use of the algebra defined in Eq. 2.14 to write

$$\mathbf{U}_{1P} = \alpha\mathbf{I} + \beta\mathbf{J} + \gamma\mathbf{A}, \tag{2.15}$$

where the coefficients depend only on the family parameters.

Following Shiau et al., we investigate the relevant Green's functions, $\mathcal{G}_{1P}(i,j) = \langle i| \mathbf{U}_{1P} |j\rangle$. We first consider the diagonal elements, each of which contains a contribution of α from $\mathbf{I}$ and β from $\mathbf{J}$. Note that there is no contribution from $\mathbf{A}$, because it is entirely off-diagonal. Hence, the N diagonal Green's functions are all equal to $\alpha + \beta$. For the off-diagonal elements, $\mathbf{I}$ never contributes and $\mathbf{J}$ always does. However, $\mathbf{A}$ contributes to only some of the elements. More precisely, each column of $\mathbf{A}$ contains exactly k ones (entirely in the off-diagonal), since each vertex is of degree k. Hence, there are kN off-diagonal Green's functions of the form $\beta + \gamma$, and the remaining $N^2 - N - kN$ are equal to β.

As can be seen from Eq. 2.14, α, β, and γ all depend only on the family parameters. Therefore, the one-particle evolution for any graph in the same family will have the same GFs, and the algorithm based on single-particle quantum evolution fails to distinguish any non-isomorphic SRGs that are in the same family.

2.3 Proof that QRWs with two non-interacting Bosons do not distinguish non-isomorphic SRGs in the same family

We now develop exact expressions for the time evolution operators for two non-interacting Bosons, and subsequently show that this evolution cannot be used to distinguish non-isomorphic SRGs in the same family. Although this result may seem expected, recent efforts [46, 44, 45] have demonstrated that non-interacting QRWs on non-translationally invariant graphs lead to effective, statistical interactions, resulting in rich physical phenomena such as Bose-Einstein condensation. The method used here is analogous to that used in Ref. [40] to show that one-particle QRWs cannot distinguish non-isomorphic SRGs from the same family, but with a more complex implementation.

First, we note that we may write the Hamiltonian for any two-Boson QRW as

$$\mathbf{H}_{2B} = -\frac{1}{2}\left(\mathbf{I}+\mathbf{S}\right)\left(\mathbf{A}\oplus\mathbf{A}\right)+U\mathbf{R}, \tag{2.16}$$

where $\mathbf{A}\oplus\mathbf{A} = \mathbf{A}\otimes\mathbf{I}+\mathbf{I}\otimes\mathbf{A}$ is a Kronecker sum, the matrix special case of a direct sum, and

$$\mathbf{S} = \sum_{i,j}\left|ij\right\rangle\left\langle ji\right|, \ \mathbf{R} = \sum_{i}\left|ii\right\rangle\left\langle ii\right|. \tag{2.17}$$

The demonstration that Eq. 2.16 is equivalent to Eq. 2.7 is given in appendix A.1. For noninteracting Bosons $U = 0$, and the evolution operator is

$$\begin{aligned}\mathbf{U}_{2B} &= e^{-it\mathbf{H}_{2B}} \\ &= \sum_{n=0}^{\infty}\frac{1}{n!}\left(it\frac{1}{2}\left(\mathbf{I}+\mathbf{S}\right)\left(\mathbf{A}\oplus\mathbf{A}\right)\right)^{n},\end{aligned} \tag{2.18}$$

where $\mathbf{U}_{2B}$ is shorthand to refer only to the non-interacting case. Now, by the definitions of the Kronecker sum and $\mathbf{S}$, it is easy to show that $\left[\left(\mathbf{I}+\mathbf{S}\right),\left(\mathbf{A}\oplus\mathbf{A}\right)\right] = \mathbf{0}$. Hence,

$$\mathbf{U}_{2B} = \sum_{n=0}^{\infty}\frac{1}{n!}\left(it\frac{1}{2}\right)^{n}\left(\mathbf{I}+\mathbf{S}\right)^{n}\left(\mathbf{A}\oplus\mathbf{A}\right)^{n}. \tag{2.19}$$

But note that $\mathbf{S}^2 = \mathbf{I}$, so $\left(\mathbf{I}+\mathbf{S}\right)^{n} = 2^{n-1}\left(\mathbf{I}+\mathbf{S}\right)$. It follows that

$$\mathbf{U}_{2B} = \frac{1}{2}\left(\mathbf{I}+\mathbf{S}\right)e^{it\mathbf{A}\oplus it\mathbf{A}}. \tag{2.20}$$

Since each matrix A in the Kronecker (direct) sum exponentiates in its own product space, we can write $e^{\mathbf{A}\oplus\mathbf{B}} = e^{\mathbf{A}} \otimes e^{\mathbf{B}}$, which leads to

$$\begin{aligned} \mathbf{U}_{2B} &= \frac{1}{2}\left(\mathbf{I}+\mathbf{S}\right) e^{it\mathbf{A}} \otimes e^{it\mathbf{A}} \\ &= \frac{1}{2}\left(\mathbf{I}+\mathbf{S}\right) \mathbf{U}^{1P} \otimes \mathbf{U}^{1P}, \end{aligned} \tag{2.21}$$

where the single-particle evolution operator $\mathbf{U}_{1P}$ is defined in Eq. 2.9 for $\mathbf{H} = -\mathbf{A}$. Since the Boson states are symmetric under particle interchange, we have matrix elements

$${}_B\langle ij|\mathbf{U}_{2B}\,|kl\rangle_B = {}_B\langle ij|\mathbf{U}_{1P} \otimes \mathbf{U}_{1P}\,|kl\rangle_B\,. \tag{2.22}$$

Expanding this using eq. 2.15, we have

$$\begin{aligned} {}_B\langle ij|\mathbf{U}_{2B}\,|kl\rangle_B &= {}_B\langle ij|\Big(\alpha^2\mathbf{I}\otimes\mathbf{I} + \beta^2\mathbf{J}\otimes\mathbf{J} \\ &+ \gamma^2\mathbf{A}\otimes\mathbf{A} + \alpha\beta\left(\mathbf{J}\oplus\mathbf{J}\right) + \alpha\gamma\left(\mathbf{A}\oplus\mathbf{A}\right) \\ &+ \beta\gamma\left(\mathbf{J}\otimes\mathbf{A} + \mathbf{A}\otimes\mathbf{J}\right)\Big)\,|kl\rangle_B\,. \end{aligned} \tag{2.23}$$

Now that we have determined the matrix elements of $\mathbf{U}_{2B}$, we can work out all the cases for eq. 2.23, which are the GFs of the system. We find that there are 22 possible values, each of which can be written as an explicit function of α, β, and γ. Since the values of the matrix elements are all only functions of SRG family parameters, they are the same for all graphs in the same SRG family. To show that the GFs are the same across a SRG family, we also need to show that the number of occurrences of each value is also a function only of SRG parameters. In Appendix A.2 we count all the types of these GFs in terms of SRG family parameters, with the results shown in table 2.1.

Because we have shown that both the values and number of occurrences of all of the two-particle Green's functions for noninteracting Bosons can be written in terms of the family parameters N, k, λ, and μ, we demonstrated that two noninteracting Bosons cannot distinguish non-isomorphic SRGs of the same family.

2.4 Analysis of the noninteracting two-Fermion evolution for SRGs

In this subsection we consider the analogous evolution generated by two non-interacting Fermions. This analysis is more complicated than for Bosons because changing the two-particle basis can introduce sign changes. If this sign ambiguity is not accounted for properly, the algorithm may falsely distinguish two graphs that are actually isomorphic.

The Hamiltonian for the two-Fermion QRW, $\mathbf{H}_{2F}$, is

$$\mathbf{H}_{2F} = \frac{1}{2}\left(\mathbf{I} - \mathbf{S}\right)\left(\mathbf{A} \oplus \mathbf{A}\right), \tag{2.24}$$

where, again, I is the identity, S is the operator that swaps the two particles, A is the adjacency matrix of the graph, and $\oplus$ denotes a direct sum. We follow the same logic we did for the Bosons but let $t \to -t$,

$$\mathbf{U}_{2F}(-t) \equiv \mathbf{U}_{2F}\ . \tag{2.25}$$

This way, the single-particle evolution operator $\mathbf{U}_{1P}$ still has time running forwards. The matrix elements of $\mathbf{U}_{2F}$ are given by

$$\begin{aligned} {}_F\langle ij|\mathbf{U}_{2F}\left|kl\right\rangle_F &= {}_F\langle ij|\Big(\alpha^2\mathbf{I}\otimes\mathbf{I} + \beta^2\mathbf{J}\otimes\mathbf{J} + \gamma^2\mathbf{A}\otimes\mathbf{A} \\ &+ \alpha\beta\left(\mathbf{J}\oplus\mathbf{J}\right) + \alpha\gamma\left(\mathbf{A}\oplus\mathbf{A}\right) \\ &+ \beta\gamma\left(\mathbf{J}\otimes\mathbf{A} + \mathbf{A}\otimes\mathbf{J}\right)\Big)\left|kl\right\rangle_F . \end{aligned} \tag{2.26}$$

We now show that there are sign ambiguities in $\mathbf{U}_F$ that arise from the choice of basis states that one uses when converting a graph to an adjacency matrix. As an example, consider the two isomorphic graphs shown in figure 2.2, which have adjacency matrices

$$\mathbf{A} = \begin{pmatrix} 0 & 1 & 0 \\ 1 & 0 & 1 \\ 0 & 1 & 0 \end{pmatrix},\ \mathbf{B} = \begin{pmatrix} 0 & 1 & 1 \\ 1 & 0 & 0 \\ 1 & 0 & 0 \end{pmatrix}. \tag{2.27}$$

We wish to write down the two-particle Hamiltonians using eq. 2.7. However, we must first pick a basis. That is, for each pair of sites $|ij\rangle \equiv |ji\rangle$, we are free to pick either ordering,

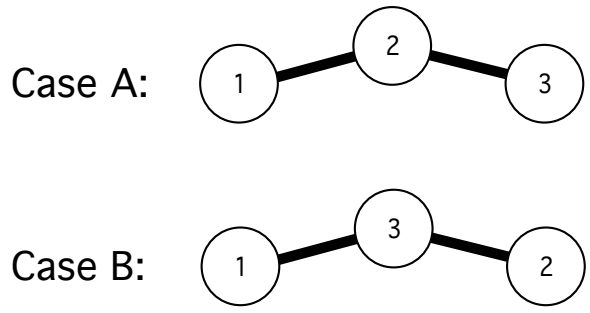

Figure 2.2: Two clearly isomorphic graphs. Graph A differs from graph B only by the labeling of vertices 2 and 3. Despite this, some matrix elements of two-particle Fermion evolution operators $\mathbf{U}_F$ of the two graphs have opposite signs. This result implies that using the numerical values of these matrix elements produces a false-positive: two isomorphic graphs are falsely distinguished.

but we cannot choose both. Supposing we pick $\{|12\rangle, |13\rangle, |23\rangle\}$, we get

$$\mathbf{H}_A = \begin{pmatrix} 0 & 1 & 0 \\ 1 & 0 & 1 \\ 0 & 1 & 0 \end{pmatrix}, \quad \mathbf{H}_B = \begin{pmatrix} 0 & 1 & -1 \\ 1 & 0 & 0 \\ -1 & 0 & 0 \end{pmatrix}. \tag{2.28}$$

Forming the evolution operators $\mathbf{U} = e^{-it\mathbf{H}}$, we have

$$\mathbf{U}_A = \begin{pmatrix} \left(\frac{\cos(\sqrt{2}t)}{2} + \frac{1}{2}\right) & -\frac{i\sin(\sqrt{2}t)}{\sqrt{2}} & \left(\frac{\cos(\sqrt{2}t)}{2} - \frac{1}{2}\right) \\ -\frac{i\sin(\sqrt{2}t)}{\sqrt{2}} & \cos\left(\sqrt{2}t\right) & -\frac{i\sin(\sqrt{2}t)}{\sqrt{2}} \\ \left(\frac{\cos(\sqrt{2}t)}{2} - \frac{1}{2}\right) & -\frac{i\sin(\sqrt{2}t)}{\sqrt{2}} & \left(\frac{\cos(\sqrt{2}t)}{2} + \frac{1}{2}\right) \end{pmatrix} \tag{2.29}$$

and

$$\mathbf{U}_B = \begin{pmatrix} \cos\left(\sqrt{2}t\right) & -\frac{i\sin(\sqrt{2}t)}{\sqrt{2}} & \frac{i\sin(\sqrt{2}t)}{\sqrt{2}} \\ -\frac{i\sin(\sqrt{2}t)}{\sqrt{2}} & \left(\frac{\cos(\sqrt{2}t)}{2} + \frac{1}{2}\right) & \left(\frac{1}{2} - \frac{\cos(\sqrt{2}t)}{2}\right) \\ \frac{i\sin(\sqrt{2}t)}{\sqrt{2}} & \left(\frac{1}{2} - \frac{\cos(\sqrt{2}t)}{2}\right) & \left(\frac{\cos(\sqrt{2}t)}{2} + \frac{1}{2}\right) \end{pmatrix}. \tag{2.30}$$

The values of the matrix elements of these two evolution operators clearly have sign differences. If we had taken into account that the second and third labels had been switched on graph B, we would have chosen the basis to be $\{|12\rangle, |13\rangle, |32\rangle\}$, fixing the factors of negative one. Unfortunately, in a situation where we are handed two graphs and asked whether or not they are isomorphic, we do not know *a priori* what the correct basis choice should be

for proper testing. Moreover, because the number of possible basis choices is 2^N, checking all of them is not feasible. We adopt here a simple strategy that eliminates this dependence of the sign on the choice of basis that arises for more than one fermion; we compare the absolute value of the elements, rather than the elements themselves. The absolute values of all the elements and their degeneracies are shown in Table 2.2. The absolute values and degeneracies can be expressed as explicit functions of family parameters, so we conclude that two non-interacting Fermions, as well as two non-interacting Bosons, fail to distinguish non-isomorphic SRGs from the same family. The enumeration of the three classes of matrix elements allowed by $\mathbf{U}_F$ are listed in table 2.2, where the $\pm$ symbol indicates that the count given is the total of elements of either sign.

2.5 Numerical testing of evolutions of random walks of interacting particles

In the preceding two subsections we have proven that QRWs with two noninteracting particles are not useful for distinguishing non-isomorphic SRGs from the same family. In this section we perform a systematic investigation of the ability of QRWs of two interacting Bosons to distinguish non-isomorphic SRGs. We go beyond the sampling performed in [40] by exhaustively checking the two-Boson interacting QRW on all tabulated SRG families with more than one member. Our work shows that this walk succeeded in all trials preformed, including successfully distinguishing the (36,15,6,6) SRG family, which has 32,548 non-isomorphic members. We used the following procedure for each pair of graphs in each family:

1. Begin with the evolved (complex) evolution matrix $\mathbf{U}_A$.
2. Take the magnitude of each element.
3. Write all the (real) entries to a list, $\mathbf{X}_A$.
4. Sort the list.

5. Compare the list using

$$\Delta = \sum_j \left| \mathbf{X}_A [j] - \mathbf{X}_B [j] \right| . \tag{2.31}$$

Note that for any two isomorphic graphs, $\Delta = 0$, so if $\Delta \neq 0$, we can conclude that the graphs are not isomorphic. Table 2.3 presents our results, which show that QRWs of two hard-core Bosons successfully distinguished all pairs of non-isomorphic graphs in all SRG families tested.

The process of numerically checking that each pair of non-isomorphic graphs was indeed distinguished by our algorithm was computationally intensive. First, in order to calculate $\mathbf{U} = e^{-it\mathbf{H}}$, one must diagonalize $\mathbf{H}$. For the $N = 64$ cases we considered, since the two-particle space has dimension $64 \cdot (64 + 1)/2 = 2080$, we needed to diagonalize large, non-sparse matrices. Further, we needed to perform many comparisons to generate all the candidates for the minimum Δ. For example, for the (36,15,6,6) family, one needs to perform $32,548 \cdot 32,547/2 = 529,669,878$ comparisons to check each pairwise Δ. To accomplish this, we used high-throughput computing environment Condor running on the University of Wisconsin's Center for High Throughput Computing cluster. The numerical error on Δ was between 10^{-14} and 10^{-9} for all families we analyzed.

In addition to our calculations with hard-core Bosons, we also investigated non-interacting Fermions numerically using the numerical procedure described above. As discussed above, comparing absolute values of matrix elements eliminates the sign discrepancy brought on by basis choice. As one expects given the results in section 2.4, the result $\Delta = 0$ is obtained for all cases tested (the first six SRG families appearing in table 2.3).

2.6 Small-time expansion and possible distinguishing operators

In this section we attempt to gain more insight into the behavior of the QRWs of two interacting Bosons by expanding the evolution operator for short times. By forming such an expansion and listing all the forms that appear, we can investigate which of these opera-

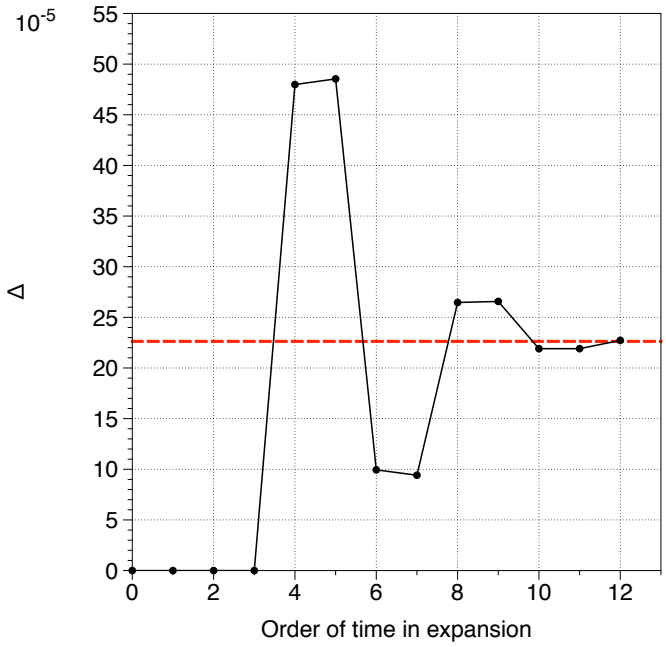

Figure 2.3: Small-time expansion comparison for the two non-isomorphic SRGs in the family (16,6,0,2) using the interacting two-Boson Hamiltonian $\mathbf{H}_{2B} = -1/2 \cdot (\mathbf{I}+\mathbf{S})(\mathbf{A}\oplus\mathbf{A}) + U\mathbf{R}$ with $U = 50$, evaluated with $t = 0.01$. The evolution operator was expanded to the different orders in t, and Δ, a dimensionless measure of differences in evolution operator matrix elements, is plotted versus the order of the expansion. The actual value of Δ obtained numerically using the full evolution operator is given by the dashed line. The distinguishing operator $U(\mathbf{A}\oplus\mathbf{A})\mathbf{R}(\mathbf{A}\oplus\mathbf{A})^2 + U(\mathbf{A}\oplus\mathbf{A})^2\mathbf{R}(\mathbf{A}\oplus\mathbf{A})$, where $\mathbf{A}$ is the adjacency matrix of the graph, and $\mathbf{R}$ counts double-occupation, causes the two graphs to be distinguished at fourth order in time.

tors contribute to the distinguishing power of the evolution operator. The operators that contribute are called distinguishing operators, and below we work out the first one, which appears in the fourth order in time. We then briefly investigate a sixth-order term, which succeeds in some instances when the fourth-order term fails.

We begin with the exact evolution operator for the interacting Boson case, which is

$$\mathbf{U} = e^{-it\left(-\frac{1}{2}(\mathbf{I}+\mathbf{S})(\mathbf{A}\oplus\mathbf{A})+U\mathbf{R}\right)}. \tag{2.32}$$

Expanding as a power series in t, we have

$$\mathbf{U} = \sum_{n=0}^{\infty} \frac{(-it)^n}{n!} \left(-\frac{1}{2}(\mathbf{I}+\mathbf{S})(\mathbf{A}\oplus\mathbf{A}) + U\mathbf{R}\right)^n. \tag{2.33}$$

Since we know from simulation that this evolution operator distinguishes SRGs, we expect that there will be an order in t at which there are terms that are not functions of only the SRG family parameters. Numerically, as shown in figure 2.3, we calculate that in the case shown these terms first appear at fourth order in time, so we endeavor to analyze the matrix elements of the first five terms of the expansion for the evolution operator,

$$\mathbf{U} \sim \mathbf{U}_0 - it\mathbf{U}_1 - \frac{t^2}{2}\mathbf{U}_2 + \frac{it^3}{6}\mathbf{U}_3 + \frac{t^4}{24} \,. \tag{2.34}$$

We first expand the terms to simplify the evolution operator, taking $\mathbf{A} \oplus \mathbf{A} = \mathbf{B}$.

$$\mathbf{U}_1 = \frac{1}{2}\left(\mathbf{I}+\mathbf{S}\right)\left(U\mathbf{R}-\mathbf{B}\right), \tag{2.35}$$

$$\mathbf{U}_2 = \frac{1}{2}\left(\mathbf{I}+\mathbf{S}\right)\left(U^2\mathbf{R}+\mathbf{B}^2-U\mathbf{RB}-U\mathbf{BR}\right), \tag{2.36}$$

$$\begin{aligned}\mathbf{U}_3 &= \frac{1}{2}\left(\mathbf{I}+\mathbf{S}\right)\left(U^3\mathbf{R}+U\mathbf{B}^2\mathbf{R}-U^2\mathbf{BR}\right.\\ &- \left.U^2\mathbf{RB}-\mathbf{B}^3+U\mathbf{RB}^2+U\mathbf{BRB}\right),\end{aligned} \tag{2.37}$$

where we used the fact that any term containing the product $\mathbf{RBR}$ vanishes due to the construction of $\mathbf{B}$. Finally,

$$\begin{aligned}\mathbf{U}_4 &= \frac{1}{2}\left(\mathbf{I}+\mathbf{S}\right)\left(U^4\mathbf{R}+U^2\mathbf{B}^2\mathbf{R}-U^3\mathbf{BR}-U\mathbf{B}^3\mathbf{R}\right.\\ &+ U^2\mathbf{RB}^2\mathbf{R}-U^3\mathbf{RB}-U\mathbf{B}^2\mathbf{RB}+U^2\mathbf{BRB}\\ &+ \left.U^2\mathbf{RB}^2+\mathbf{B}^4-U\mathbf{RB}^3-U\mathbf{BRB}^2\right).\end{aligned} \tag{2.38}$$

Numerically, we determined that the fourth order operators that successfully distinguished (16,6,0,2), and thus could not be counted in terms of SRG family parameters, was the combination of $U\mathbf{BRB}^2 + U\mathbf{B}^2\mathbf{RB}$. If either of these operators is removed from the fourth order term, Δ drops to zero. Upon further investigation, graphs with more vertices, starting with (25,12,5,6), are not necessarily distinguished by the fourth order in t. For some, a sixth order expansion was necessary, where we found that at least the term $\mathbf{B}^2\mathbf{RB}^3$ helped to distinguish these graphs. We tried a sampling of graphs from the families up to $N = 40$, and found that this sixth order term succeeded in every instance we tried.

2.7 Discussion

This chapter takes several steps towards characterizing the additional power that quantum walks of interacting particles have for distinguishing non-isomorphic strongly regular graphs, as compared to quantum random walks of noninteracting particles. We prove analytically that quantum random walks of two noninteracting particles, either bosons or fermions, cannot distinguish non-isomorphic strongly regular graphs from the same family. We investigate numerically the quantum time-evolution operator for a quantum random walk with two interacting bosons and show that the resulting Green's functions can be used to distinguish all non-isomorphic pairs of strongly regular graphs that were investigated. We perform a much more comprehensive numerical test of the interacting particle algorithm than has been done previously, and find that quantum random walks of two hard-core bosons successfully distinguish all known non-isomorphic pairs of SRGs, which include graphs with up to 64 vertices, and family sizes as large as 32,548 non-isomorphic members.

We now discuss how our results are relevant to possible algorithms for solving GI. If our algorithm for two hard-core Bosons does indeed distinguish arbitrary graphs, then GI is in P, since the number of particles is fixed, and only the lattice size increases with number of vertices. But, if GI is not in P, then for some pair of graphs, our two particle algorithm must break. Hence, if such a case was identified, then one could try increasing particle number, which could potentially place GI in BQP, the complexity class solvable efficiently on a quantum computer. Unfortunately, we exhausted our test cases (the SRGs), so we could not test this hypothesis.

Although we found that two non-interacting Bosons were not helpful for distinguishing SRGs, we suspect that at larger numbers of non-interacting particles, QRWs might be able to distinguish SRGs. This suspicion is due to refs. [46, 44, 45], where non-interacting QRWs generate an effective external field in the statistical limit. The resulting effective particle-field interactions might produce distinguishing power comparable to our explicit hard-core particle-particle interaction, while providing for an easier analysis. It would be interesting

to examine the several-particle non-interacting QRW to see if this is indeed the case.

Table 2.1: This table enumerates the Green's functions for the QRW with two non-interacting Bosons on a SRG with family parameters (N, k, μ, λ). The Hamiltonian considered is $\mathbf{H}_B = -1/2 \cdot (\mathbf{I} + \mathbf{S})(\mathbf{A} \oplus \mathbf{A})$, where $\mathbf{S}$ swaps the two particles and $\mathbf{A}$ is the adjacency matrix of the graph. Because the $\mathbf{A}$, $\mathbf{I}$, and $\mathbf{J}$ form an algebra, the parameters α, β, and γ are the same for every graph in an SRG family (Eq. (2.14). The evolution operator for noninteracting Bosons, $\mathbf{U}_B = 1/2\,(\mathbf{I} + \mathbf{S})\,\mathbf{U}^{1P} \otimes \mathbf{U}^{1P}$, contains terms bilinear in $\mathbf{I}$, $\mathbf{J}$, and $\mathbf{A}$, with coefficients that can be written in terms of α, β, and γ. The GFs, formed by taking matrix elements of $\mathbf{U}_B$ (Eq. (2.10), are divided into symmetry classes (a, b), where a indicates the number of distinct basis indices and b is the number of indices shared between the left and right sides. For example, $\langle 34|_B U_B |24\rangle_B$, where $|ij\rangle_B$ indicates identical Bosons on vertices i and j, falls into the symmetry class $(3, 1)$, since it has three distinct indices (2,3,4) and the left and right side have one index in common (2). Since the total number of entries with any given particular value can be counted in terms of numbers that are constant for a given set of family parameters, the GFs generated by non-isomorphic members of the same SRG family must have the same values and the same degeneracies.

Element Class	Value of Element	Number of Occurrences
(4,0)	$4\beta\gamma + 2\gamma^2 + 2\beta^2$	$1/4 \cdot N\big(k^2(\mu+1) + k\left(\lambda^2 - \lambda(\mu+2) + \mu - 1\right) -2(N-1)\mu\big)$
	$3\beta\gamma + \gamma^2 + 2\beta^2$	$N\mu(N-k-1)(k+\lambda-\mu)$
	$2\beta\gamma + 2\beta^2 + \gamma^2$	$1/(2k) \cdot \left[N(N-k-1)\left(k^3 - 2k^2\mu + (N-1)\mu^2\right)\right]$
	$2\beta\gamma + 2\beta^2$	$1/k \cdot \left[N(N-k-1)\left(k^3 - k^2(2\mu+1) + (N-1)\mu^2\right)\right]$
	$\beta\gamma + 2\beta^2$	$1/k \cdot [N(k-N+1)(k-\mu)(k(2k-N+2) - N\mu + \mu)]$
	$2\beta^2$	$1/(4k) \cdot \big[N(N-k-1)\big(k(-3kN + k(3k+8) +N^2 - 5N + 6) - 2k(k+1)\mu + (N-1)\mu^2\big)\big]$
	Subtotal:	$1/4 \cdot N(N-1)(N-2)(N-3)$
(3,0)	$4/\sqrt{2} \cdot \beta\gamma + 2/\sqrt{2} \cdot \beta^2 +2/\sqrt{2} \cdot \gamma^2$	$kN(k-\lambda-1) + kN\lambda$
	$2/\sqrt{2} \cdot \beta\gamma + 2/\sqrt{2} \cdot \beta^2$	$2kN(N-k-1)$
	$2/\sqrt{2} \cdot \beta^2$	$N(k-N+1)(k-N+2)$
	Subtotal:	$N(N-1)(N-2)$
(3,1)	$\alpha\beta + \alpha\gamma + 3\beta\gamma + 2\beta^2 + \gamma^2$	$kN\lambda$
	$\alpha\beta + 2\beta\gamma + 2\beta^2 + \gamma^2$	$N(N-1-k)\mu$
	$\alpha\beta + \alpha\gamma + 2\beta\gamma + 2\beta^2$	$2N(N-1-k)\mu$
	$\alpha\beta + \alpha\gamma + \beta\gamma + 2\beta^2$	$kN(-2k+N+\lambda)$
	$\alpha\beta + \beta\gamma + 2\beta^2$	$2kN(-2k+N+\lambda)$
	$\alpha\beta + 2\beta^2$	$N(1+k-N)(2+2k-N-\mu)$
	Subtotal: 2	$N(N-1)(N-2)$
(2,0)	$2\beta\gamma + \beta^2 + \gamma^2$	kN
	β^2	$N(N-k-1)$
	Subtotal:	$N(N-1)$
(2,1)	$2/\sqrt{2} \cdot \left(\alpha\beta + \alpha\gamma + \beta\gamma + \beta^2\right)$	$2kN$
	$2/\sqrt{2} \cdot \left(\alpha\beta + \beta^2\right)$	$2N(N-k-1)$
	Subtotal:	$2N(N-1)$
(2,2)	$\alpha^2 + 2\alpha\beta + 2\beta\gamma + 2\beta^2 + \gamma^2$	$1/2 \cdot kN$
	$\alpha^2 + 2\alpha\beta + 2\beta^2$	$1/2 \cdot N(N-k-1)$
	Subtotal:	$1/2 \cdot N(N-1)$
(1,2)	$\alpha^2 + 2\alpha\beta + \beta^2$	N
Total:		$1/4 \cdot N^2(N+1)^2$

Table 2.2: Enumeration of the Green's functions for QRWs of two non-interacting Fermions. The Hamiltonian for two noninteracting Fermions is $\mathbf{H}_{2F} = 1/2 \cdot (\mathbf{I} - \mathbf{S})(\mathbf{A} \oplus \mathbf{A})$, where $\mathbf{S}$ swaps the two particles and $\mathbf{A}$ is the adjacency matrix of the graph. Hence, the two-Fermion evolution operator, defined with $t \to -t$ to keep U^{1P} running with forward time, is $\mathbf{U}_F = 1/2\,(\mathbf{I} - \mathbf{S})\,\mathbf{U}^{1P} \otimes \mathbf{U}^{1P}$. It contains terms bilinear in $\mathbf{I}$, $\mathbf{J}$, and $\mathbf{A}$, with coefficients written as combinations of α, β, and γ, where the parameters α, β, and γ, are defined in Eq. (2.15). We divide the matrix elements $\langle ij|_F\, U_{2F}\, |kl\rangle_F$ of the GFs into classes (a, b), where a indicates the number of distinct indices and b is the number of indices shared between the left and right sides. For example, $\langle 34|_F\, U_F\, |24\rangle_F$ falls into class $(3, 1)$, since it has the three distinct indices (2,3,4) and the left and right side have the index (2) in common. The $\pm$ next to some of the element values indicates that the count applies to all elements with the given magnitude; this is done because the number of elements with each sign depends on the choice of two-particle basis. The total number of matrix elements with a given absolute value can be expressed in terms of the SRG family parameters. Therefore, we conclude that the matrix elements of the GFs of two non-isomorphic members of the same SRG family must be equivalent up to sign differences.

Element Class	Value of Element	Number of Occurrences
(4,0)	0	$n/(4k)\big(-6k^4 + 2k^3(5n + 6\mu - 7) - 4k^2(n-1)(n + 3\mu - 2)$ $+k(n-1)\left((n-5)n - 6\mu^2 + 6\right) + 6(n-1)^2\mu^2\big)$
	$\pm\left(\beta\gamma + \gamma^2\right)$	$N\mu \cdot (N - k - 1)(k + \lambda - \mu)$
	$\pm\left(\gamma^2 + 2\beta\gamma\right)$	$1/k \cdot \left[N(N-k-1)\left(k^3 - 2k^2\mu + (N-1)\mu^2\right)\right]$
	$\pm\beta\gamma$	$1/k \cdot [N(k - N + 1)(k - \mu)(k(2k - N + 2) - N\mu + \mu)]$
	Subtotal:	$1/4 \cdot N(N-1)(N-2)(N-3)$
(3,1)	$\pm\left(\alpha\beta + \alpha\gamma - \beta\gamma - \gamma^2\right)$	$kN\lambda$
	$\pm\left(\alpha\beta - 2\beta\gamma - \gamma^2\right)$	$N(N - 1 - k)\mu$
	$\pm\left(\alpha\beta + \alpha\gamma\right)$	$2N(N - 1 - k)\mu$
	$\pm\left(\alpha\beta + \alpha\gamma + \beta\gamma\right)$	$kN(-2k + N + \lambda)$
	$\pm\left(\alpha\beta - \beta\gamma\right)$	$2kN(-2k + N + \lambda)$
	$\pm\alpha\beta$	$N(1 + k - N)(2 + 2k - N - \mu)$
	Subtotal:	$N(N-1)(N-2)$
(2,2)	$\alpha^2 + 2\alpha\beta - 2\beta\gamma - \gamma^2$	$1/2 \cdot kN$
	$\alpha^2 + 2\alpha\beta$	$1/2 \cdot N(N - k - 1)$
	Subtotal:	$1/2 \cdot N(N-1)$
Total:		$1/4 \cdot N^2(N-1)^2$

Table 2.3: Numerical simulations of QRWs of two hard-core Bosons on many SRG families with multiple non-isomorphic members. The Hamiltonian used was $\mathbf{H}_B = -1/2 \cdot (\mathbf{I} + \mathbf{S})(\mathbf{A} \oplus \mathbf{A}) + U\mathbf{R}$, where $\mathbf{S}$ swaps the two particles, $\mathbf{A}$ is the adjacency matrix of the graph, and $\mathbf{R}$ counts double-occupation. To evaluate the hard-core limit, we took $\mathbf{U} \to \infty$. All non-isomorphic graphs in the families indicated were compared pairwise, with Δ is a measure of how different the matrix elements of the evolution operator are, defined precisely in eq. 2.31. When $\Delta = 0$, the list of matrix elements of the two evolution operators being compared have the same magnitudes. The minimum values of Δ were non-zero for all pairs of non-isomorphic graphs that were examined.

SRG family (N, k, μ, λ)	non-isomorphic members	minimum Δ
(16,6,2,0)	2	94.273
(16,9,4,6)	2	2.723
(25,12,5,6)	15	3.636
(26,10,3,4)	10	7.356
(28,12,6,4)	4	27.607
(29,14,6,7)	41	4.017
(35,18,9,9)	227	5.243
(36,14,4,6)	180	2.621
(36,15,6,6)	32,548	1.512
(37,18,8,9)	6,760	4.310
(40,12,2,4)	28	3.065
(45,12,3,3)	78	5.868
(64,18,2,6)	167	2.574

Chapter 3

Non-interacting multi-particle quantum random walks applied to the graph isomorphism problem for strongly regular graphs

3.1 Introduction

There has long been interest in algorithms that use random walks to solve a variety of mathematical and scientific problems [10, 11, 12, 13, 14]. Typically, the random walks in question have been classical random walks (CRWs). However, there is increasing interest in random walks with quantum walkers. In particular settings, these quantum random walks (QRWs) have been shown to have computational advantages over CRWs [15, 16, 17]. Certain algorithms utilizing QRWs have been proven to have faster runtimes than their best known classical counterparts [18, 19, 20, 21, 22, 23, 24].

Additionally, QRWs have been experimentally demonstrated in a variety of physical settings, such as ion traps [30], atom traps [52], quantum optics [53, 54], and NMR systems [28]. Recent works have experimentally realized QRWs with two walkers, demonstrating the

potential for implementing QRWs with many walkers [55, 56, 57, 58]. Moreover, there are proposed methods for physically implementing non-trivial walks [31], indicating that there may be many QRW algorithms to be developed that would both be physically realizable and computationally powerful.

Often the context for QRWs is one in which the walks occur on graphs. It has been shown that QRWs are universal; any quantum algorithm can be mapped onto a QRW on such a graph [32]. It is also the case that many interesting computational problems are easily expressed in graph theoretic terms [3]. Thus there is considerable interest in further exploring QRWs on graphs, with the hope that we may be able to use such a framework to solve certain problems.

There are also interesting physical phenomena associated with many particles walking on a graph. It is known that QRWs of non-interacting bosons on graphs can give rise to effective statistical interactions [44, 45, 46]. It has even been shown that Bose-Einstein condensation can occur at finite temperature in less than two dimensions if the bosons are placed on a particular kind of graph [46]. Therefore, there is motivation in further exploring the dynamics of multi-particle ensembles on graphs.

This chapter addresses the graph isomorphism problem, which is, given two graphs, to determine if they are isomorphic; that is, if one can be transformed into the other by a relabeling of vertices. This problem is of note for several reasons. While many graph pairs may be distinguished by a classical algorithm which runs in a time polynomial in the number of vertices of the graphs, there exist pairs which are computationally difficult to distinguish. Currently, the best general classical algorithm has a runtime of $O(c^{\sqrt{N}\log N})$, where c is a constant and N is the number of vertices in the two graphs [33]. Graph isomorphism (GI) is believed to be similar to factoring in that both are thought to be NP-Intermediate problems [34]. Additionally, both problems may be approached as hidden subgroup problems, though this approach has had limited success for GI [37]. Due to these similarities, and the known quantum speedup available for factoring [35], there is hope that there similarly exists a quantum speedup for GI.

Strongly regular graphs (SRGs) are a particular class of graphs that are difficult to distinguish classically [33]. (See Section 3.2 for a formal definition.) Shiau *et al.* showed that the single-particle continuous-time QRW fails to distinguish pairs of SRGs with the same family parameters [40]. Gamble *et al.* extended these results, proving that QRWs of two non-interacting particles will always fail to distinguish pairs of non-isomorphic strongly regular graphs with the same family parameters [3]. They also demonstrated numerically the distinguishing power of the two-boson interacting QRW; it successfully distinguished all tested pairs of SRGs [3]. Since the publication of Gamble *et al.*, Smith proved that for any fixed number of bosons p, there exist non-isomorphic graph pairs which the p-boson interacting walk fails to distinguish [59]. These counterexample graphs are not strongly regular; whether or not the two-boson interacting walk successfully distinguishes non-isomorphic strongly regular graphs is still an open question.

Investigations into discrete-time QRW algorithms for GI have also been made [43, 60, 61]. Berry and Wang numerically showed that a discrete-time non-interacting QRW of two particles could distinguish some SRGs, something its continuous-time counterpart cannot do. However, this distinguishing power is not universal on SRGs, nor is an analytic explanation of the distinguishing power given [61]. The discrete-time algorithm proposed by Emms *et al.* successfully distinguished all tested SRGs [43], but it has been shown to not be universal [59]; it is unknown if it is universal on SRGs. Additionally, for the same number of particles, the discrete-time QRWs require Hilbert spaces larger than the ones required by continuous-time QRWs [61]. In an effort to relate discrete-time and continuous-time QRWs, it has been noted that the coin state of a discrete-time walk may be thought of as a relativistic particle's internal degree of freedom; such a feature is absent from continuous-time QRWs [62]. The relationship between discrete-time and continuous-time quantum random walks in the context of the graph isomorphism problem has been examined as well [63]. It remains an open question as to whether or not discrete-time walks in general have fundamentally greater distinguishing power than continuous-time walks, or if they are better candidates for a universal GI algorithm.

This chapter extends the results of Chapter 2 to address continuous-time multi-particle non-interacting quantum walks on SRGs, with a particular focus on understanding the role of particle number in determining the distinguishing power of the walks. We have several main results. We numerically demonstrate that three-particle non-interacting walks have significant (but not universal) distinguishing power on hard-to-distinguish pairs of SRGs. Additionally, we find that a four-fermion non-interacting walk has even greater (but still not universal) distinguishing power on SRG pairs. We analytically explain where this distinguishing power comes from, and how these multi-particle non-interacting walks are fundamentally different from single-particle and two-particle non-interacting walks. This is done by showing that a particular feature present in the smaller walks which limits their distinguishing power is not present in walks of three or more non-interacting particles. Further, we analytically show that, even though the distinguishing power of non-interacting walks increases with particle number, there is no non-interacting walk with a fixed number of particles that can, with our comparison algorithm, distinguish all strongly regular graphs.

This chapter is organized as follows. Section 3.2 covers the requisite background, including graph theoretic definitions and concepts, a review of strongly regular graphs, and a formal definition of the quantum random walk. In Section 3.3, we first demonstrate analytically how two-particle non-interacting walks are fundamentally different from three-particle non-interacting walks. We then present the numerical results for non-interacting three-particle and four-particle walks on SRGs. In the final part of Section 3.3, we demonstrate that a p-particle non-interacting QRW cannot distinguish all SRGs for any fixed p. We discuss our conclusions in Section 3.4.

Appendix A discusses a fundamental difference between non-interacting walks of two particles and non-interacting walks of more than two particles. Appendix B provides details necessary to show that a non-interacting p-particle walk cannot distinguish all SRGs for a fixed p. In Appendix C, we show that the number of unique evolution operator elements for a p-particle non-interacting walk is super-exponential in p. Lastly, we explain in Appendix D how we ensure numerical stability and determine numerical error in our simulations.

3.2 Background

Basic Graph Definitions

Here we develop the background and definitions necessary to discuss multi-particle QRWs on graphs. This chapter only considers simple, undirected graphs. A graph $G = (V, E)$ is a set of vertices V and edges E. The vertices are a set of labels, usually integers, and the edges are a list of unordered pairs of vertices. If a pair of vertices appears in E, then the vertices are connected by an edge; otherwise there is no edge between the vertices and they are considered disconnected. The terms "adjacent", "neighboring", and "connected" may be used interchangeably to refer to a vertex pair which shares an edge. It is convenient to represent a graph by its adjacency matrix $\mathbf{A}$, defined as:

$$A_{ij} = \begin{cases} 1 & \text{if vertices } i \text{ and } j \text{ are connected.} \\ 0 & \text{if vertices } i \text{ and } j \text{ are disconnected.} \end{cases} \tag{3.1}$$

A graph of N vertices has an $N \times N$ adjacency matrix. For the undirected and simple graphs considered here, $\mathbf{A}$ is symmetric, with zeros on the diagonal.

Two graphs are isomorphic if one graph is transformed into the other by a relabeling of vertices. More formally, given two adjacency matrices $\mathbf{A}$ and $\mathbf{B}$, the graphs represented by $\mathbf{A}$ and $\mathbf{B}$ are isomorphic if and only if a permutation matrix $\mathbf{P}$ exists such that $\mathbf{B} = \mathbf{P}^{-1}\mathbf{A}\mathbf{P}$.

Strongly Regular Graphs

This chapter addresses strongly regular graphs (SRGs), which we examine because they are difficult to distinguish classically, and because of their simple algebraic properties [33, 47]. An SRG is characterized by four parameters, denoted (N, k, λ, μ). N is the number of vertices in the graph, and each vertex is connected to k other vertices (the graph is k-regular, or has degree k). Each pair of neighboring vertices shares λ common neighbors, while each pair of non-adjacent vertices shares μ common neighbors. The set of SRGs sharing the same set of four parameters is referred to as an SRG *family*; correspondingly, the four parameters are often called the family parameters. While some SRG families may

have only one non-isomorphic member, there are many families of SRGs with multiple non-isomorphic graphs. These are the families which are of interest to us.

The adjacency matrix of any SRG has at most three eigenvalues. As these eigenvalues and their multiplicities are functions of the family parameters, the adjacency matrices of SRGs in the same family are always cospectral [47]. This contributes to the difficulty of distinguishing non-isomorphic SRGs.

The adjacency matrix of any SRG satisfies the particularly useful algebraic identity [47]:

$$\mathbf{A}^2 = (k-\mu)\mathbf{I} + \mu\mathbf{J} + (\lambda-\mu)\mathbf{A}, \tag{3.2}$$

where $\mathbf{I}$ is the identity and $\mathbf{J}$ is the matrix of all ones. Because $\mathbf{J}^2 = N\mathbf{J}$, $\mathbf{JA} = \mathbf{AJ} = k\mathbf{A}$, and $\mathbf{I}$ acts trivially on $\mathbf{I}$, $\mathbf{J}$, and $\mathbf{A}$, we see that $\{\mathbf{I}, \mathbf{J}, \mathbf{A}\}$ forms a commutative three-dimensional algebra, so we conclude that for any positive integer n:

$$\mathbf{A}^n = \alpha_n\mathbf{I} + \beta_n\mathbf{J} + \gamma_n\mathbf{A}, \tag{3.3}$$

where α_n, β_n, and γ_n depend only on n and the family parameters.

Defining the quantum random walk

Now we discuss how we form a continuous-time non-interacting quantum random walk on a graph. As in [3], we use the Hubbard model, where each site corresponds to a graph vertex. A particle can move from one vertex to another if the two vertices are connected. Thus, for a graph on N vertices with adjacency matrix $\mathbf{A}$, our non-interacting Hamiltonian is given by

$$\mathbf{H} = -\sum_{i,j}^{N} A_{ij} c_i^\dagger c_j, \tag{3.4}$$

where $c_i^\dagger$ and c_i are the creation and annihilation operators, respectively, for a boson or (spinless) fermion at site i. For bosons, they satisfy the commutation relations $[c_i, c_j^\dagger] = \delta_{ij}$ and $[c_i, c_j] = [c_i^\dagger, c_j^\dagger] = 0$. For fermions, they satisfy the anti-commutation relations $\{c_i, c_j^\dagger\} = \delta_{ij}$ and $\{c_i, c_j\} = \{c_i^\dagger, c_j^\dagger\} = 0$.

For walks of p bosons, we use basis states of the form $|j_1 \dots j_p\rangle_B$, which is the appropriately symmetrized basis state with bosons on vertices j_1 through j_p. These vertices need not

be distinct, since vertices may be multiply occupied. Similarly, for walks of p fermions, we use basis states of the form $|j_1 \dots j_p\rangle_F$, which is the appropriately anti-symmetrized basis state with fermions on vertices j_1 through j_p. These vertices must be distinct, because the Pauli exclusion principle implies that no vertex can be occupied by multiple fermions. We refer to these bases as the particles-on-vertices bases.

Following [3] and [59], it is straightforward to show that the elements of the p-boson or p-fermion non-interacting Hamiltonian ($\mathbf{H}_{p,B}$ and $\mathbf{H}_{p,F}$, respectively) are, in their respective particles-on-vertices bases:

$$\begin{aligned} {}_B\langle i_1 \dots i_p|\mathbf{H}_{p,B}|j_1 \dots j_p\rangle_B = \\ -{}_B\langle i_1 \dots i_p|\mathbf{A}^{\oplus p}|j_1 \dots j_p\rangle_B, \end{aligned} \tag{3.5}$$

$$\begin{aligned} {}_F\langle i_1 \dots i_p|\mathbf{H}_{p,F}|j_1 \dots j_p\rangle_F = \\ {}_F\langle i_1 \dots i_p|\mathbf{A}^{\oplus p}|j_1 \dots j_p\rangle_F, \end{aligned} \tag{3.6}$$

where

$$\begin{aligned} \mathbf{A}^{\oplus p} = \underbrace{\mathbf{A} \otimes \mathbf{I} \otimes \mathbf{I} \dots \otimes \mathbf{I}}_{p} \\ + \mathbf{I} \otimes \mathbf{A} \otimes \mathbf{I} \dots \otimes \mathbf{I} + \dots + \mathbf{I} \otimes \mathbf{I} \otimes \mathbf{I} \dots \otimes \mathbf{A}. \end{aligned} \tag{3.7}$$

The evolution operator is defined in the standard manner:

$$\mathbf{U}(t) = e^{-it\mathbf{H}}, \tag{3.8}$$

where $\hbar = 1$ for convenience.

Comparison algorithm

Our method for comparing two graphs in an attempt to determine if they are isomorphic or not is the same as the one used in [3]. Given two graphs with adjacency matrices $\mathbf{A}$ and $\mathbf{B}$, we compute in the particles-on-vertices basis $\mathbf{U_A}(t)$ and $\mathbf{U_B}(t)$, respectively, for the same number and type of particle, as well as the same time t. The absolute value of each element

of $\mathbf{U_A}(t)$ and $\mathbf{U_B}(t)$ are written to lists $\mathbf{X_A}$ and $\mathbf{X_B}$, respectively. Both lists are sorted, and we compute the distance between the lists, Δ:

$$\Delta = \sum_{\nu} |\mathbf{X_A}[\nu] - \mathbf{X_B}[\nu]|. \tag{3.9}$$

We say that $\mathbf{A}$ and $\mathbf{B}$ are distinguished by a particular walk if and only if that walk yields $\Delta \neq 0$; isomorphic graphs and non-isomorphic non-distinguished graphs both yield $\Delta = 0$ [3]. We note that we lose phase information by taking the absolute value of the elements, but it makes our comparison procedure more tractable, and seems to do no harm, see [3]. Lastly, for all simulations presented in this chapter, $t = 1$.

3.3 Quantum random walks on strongly regular graphs

Comparing distinguishing power of two- and three-particle non-interacting walks

In this subsection we show analytically that there is a fundamental difference between two-particle non-interacting walks and three-particle non-interacting walks on strongly regular graphs, because three-particle non-interacting walks are capable of distinguishing SRGs from the same family, unlike two-particle non-interacting walks. To show this difference, we recall the proof used by Gamble *et al.* to demonstrate the inadequacy of two-particle walks [3].

The proof in Gamble *et al.* first shows that the value of every element in the two-particle evolution operators (${}_B\langle ij|\mathbf{U}_{2B}(t)|kl\rangle_B$ or ${}_F\langle ij|\mathbf{U}_{2F}(t)|kl\rangle_F$) must be a function only of the SRG family parameters and the time t. Then it is shown that the multiplicity of each element value in the evolution operator is also a function of SRG family parameters. We begin similarly here for the three-particle walk, and find that while the values of the elements are all functions of the SRG family parameters, the multiplicities of the values are not.

We first address the element values. We refer to each element of each evolution operator (computed in the particles-on-vertices basis) as a *Green's function*, following the nomenclature of Gamble *et al.* [3]. Because the three-particle walk in question is non-interacting, we

know that the evolution operator for the walk factorizes into three single-particle evolution operators:

$$ {}_B\langle ijk|\mathbf{U}_{3B}|lmn\rangle_B = {}_B\langle ijk|{\mathbf{U}_{1P}}^{\otimes 3}|lmn\rangle_B, \tag{3.10} $$

$$ {}_F\langle ijk|\mathbf{U}_{3F}|lmn\rangle_F = {}_F\langle ijk|\overline{\mathbf{U}_{1P}}^{\otimes 3}|lmn\rangle_F, \tag{3.11} $$

where ${\mathbf{U}_{1P}}^{\otimes 3} = \mathbf{U}_{1P} \otimes \mathbf{U}_{1P} \otimes \mathbf{U}_{1P}$; $\mathbf{U}_{1P}$ is the evolution operator for the single-particle walk, that is, $\mathbf{U}_{1P} = e^{i\mathbf{A}t}$ and $\overline{\mathbf{U_{1P}}} = e^{-i\mathbf{A}t}$.

Recalling Eq. (3.3), and expanding $e^{i\mathbf{A}t}$ as a Taylor series in powers of $\mathbf{A}t$, we note that:

$$ \mathbf{U}_{1P} = \alpha\mathbf{I} + \beta\mathbf{J} + \gamma\mathbf{A}, \tag{3.12} $$

where α, β, and γ are functions of the family parameters and the time t. Therefore, we conclude that all possible values of the elements of $\mathbf{U}_{3B}$ and $\mathbf{U}_{3F}$ (the Green's functions) are determined by the family parameters. Thus, the set of all potential values for the Green's functions are the same for any two graphs in the same family. Any distinguishing power of the walks must come from the existence of at least one Green's function with different *multiplicities* for non-isomorphic graphs in the same family.

Gamble *et al.*, prove that the multiplicity of each Green's function for two-particle non-interacting walks is a function of the SRG family parameters. In Appendix A, we show that there exist Green's functions for the three-particle non-interacting walk on SRGs whose multiplicities are *not* functions of the family parameters. This is because the multiplicity of a Green's function in a p-particle walk depends on how many shared neighbors a collection of up to p vertices has. For $p = 2$, strong regularity uniquely determines the number of shared neighbors: λ if the vertices are connected, and μ if they are not. However, for $p \geq 3$, the multiplicity is dependent on the number of shared neighbors among sets of p vertices. Thus the multiplicity is not uniquely determined by strong regularity, so the multiplicity for such a Green's function need not be a function of the family parameters.

The definition of SRGs does not directly constrain the number of neighbors of a set of p vertices with $p \geq 3$. However, this difference from the two-particle case does not guarantee that walks of three or more particles can distinguish non-isomorphic SRGs, only that they

have the potential to do so. Our numerical investigations of the distinguishing power of these walks are presented in Section 3.3.

Numerical results

Table 3.1: Numerical results for the three-particle non-interacting walks on twelve families of SRGs. The first column lists the family parameters for the particular SRG family being examined. The second column lists the number of graphs in the family that we compared. This number is equal to the number of graphs in the family, with the exception of (49,18,7,6), where we only examined a subset of the family. The third column gives the number of comparisons made for each family, which is equal to the number of graphs in that family that we examined choose 2. The fourth and fifth columns list the number of graph pairs which the three-boson and three-fermion walks fail to distinguish, respectively. We see that out of 70 712 graph comparisons, both the boson and fermion walks fail a total of 256 times, corresponding to a success rate of greater than 99.6%

SRG Family (N, k, λ, μ)	Number of Graphs	Comparisons	Boson Failures	Fermion Failures
(16, 6, 2, 2)	2	1	0	0
(16, 9, 4, 6)	2	1	0	0
(25, 12, 5, 6)	15	105	0	0
(26, 10, 3, 4)	10	45	1	1
(28, 12, 6, 4)	4	6	0	0
(29, 14, 6, 7)	41	820	0	0
(35, 18, 9, 9)	227	25651	38	38
(36, 14, 4, 6)	180	16110	89	89
(40, 12, 2, 4)	28	378	8	8
(45, 12, 3, 3)	78	3003	7	7
(49, 18, 7, 6)	147	10731	21	21
(64, 18, 2, 6)	167	13861	92	92

Table 3.2: Numerical results for four-fermion non-interacting walks on 136 graph pairs that are not distinguished by three-particle non-interacting walks. Of the 136 graph pairs tested, only one pair is not successfully distinguished. We therefore see that increasing the number of non-interacting particles beyond three continues to increase the distinguishing power of the non-interacting QRWs.

Family (N, k, λ, μ)	3 Particle Failures	4 Fermion Failures
(26, 10, 3, 4)	1	0
(35, 18, 9, 9)	38	0
(36, 14, 4, 6)	89	1
(40, 12, 2, 4)	8	0

In this subsection, we present our numerical results for three-particle and four-fermion walks on SRGs. To simulate a walk on a graph, we compute the appropriate Hamiltonian

and exponentiate it to compute its corresponding evolution operator, following the algorithm described in Section 3.2. Then, to compare pairs of non-isomorphic graphs from the same family, we compute the list distance Δ, defined in Equation (3.9). We find our error on Δ to be no greater than 10^{-6}, so two non-isomorphic graphs are considered distinguished if and only if $\Delta > 10^{-6}$. Further details of numerical error analysis are provided in Appendix D.

Because the Hamiltonians are very large, we must use a sparse matrix exponentiation routine [64] to make exponentiation computationally tractable. (The largest evolution operators we compute have a dimension of 91 390, and correspond to the four-fermion walks on graphs of 40 vertices.) Additionally, in order to be able perform these exponentiations sufficiently quickly, we parallelize the computations, utilizing the Open Science Grid and the University of Wisconsin-Madison's Center for High Throughput Computing Cluster.

Our numerical results for three-particle walks are presented in Table 3.1. For the 70 712 pairs of SRGs compared, the boson and fermion walks distinguish all but 256 pairs, corresponding to a success rate of greater than 99.6%. Thus we see that both the three-boson and three-fermion walks have significant (but not universal) distinguishing power on SRGs, while the two-particle non-interacting walks fail on *all* pairs of non-isomorphic graphs in the same family [3].

The bosonic and fermionic walks fail to distinguish the same pairs of non-isomorphic graphs that we tested; we have found no graph pair that one kind of particle successfully distinguishes while the other does not. Thus, despite having a state space of smaller dimension (due to Pauli exclusion), the three-fermion walk has the same distinguishing power as the three-boson walk on all tested graph pairs. It remains an open question whether graph pairs exist for which this is not true.

Having identified some graph pairs that three non-interacting particles fail to distinguish, we want to know if non-interacting walks exist that can distinguish these graphs. However, it is computationally expensive (even with speedup provided by parallelization) to simulate four-particle walks. We therefore simulated only fermion walks, and only on

a subset of the three-particle counterexample graph pairs. Our results are summarized in Table 3.2. We simulated four-fermion non-interacting walks on 136 counterexample pairs, finding that all but one pair are distinguished.

Since increasing the number of non-interacting particles in the walk apparently increases the distinguishing power, it is natural to ask "Does there exist a p such that the p-particle non-interacting walk can distinguish all strongly regular graphs?" The next subsection shows that the answer to this question is no.

Limitations of non-interacting walks

In this subsection, we show that pairs of non-isomorphic strongly regular graphs exist that are not distinguished by any p-particle non-interacting quantum walk with fixed p in conjunction with the comparison algorithm described by Equation (3.9). This is because for a fixed p, there exists an N such that the number of strongly regular graphs with N vertices is larger than the maximum number of graphs distinguishable by the p-particle non-interacting walk.

To prove this claim, we define $S(N)$, the number of strongly regular graphs in a particular family with N vertices, and $Z(p, N)$, the number of distinct "graph fingerprints" that the p-boson walk can generate for an SRG family whose graphs have N vertices. By a "graph fingerprint," we mean a sorted list of the absolute value of every element of an evolution operator (Eq. (3.10)). We examine the boson walk here, because its state space is strictly larger than the fermion walk of the same number of particles. Thus the p-boson walk generates more fingerprints than the p-fermion walk (even though we have seen no evidence yet that it distinguishes more graph pairs). Therefore, $Z(p, N)$ bounds from above the maximum number of SRGs with N vertices in a particular family that non-interacting walks of either p fermions or bosons can distinguish.

We now define the ratio $R(p, N)$:

$$R(p, N) = \frac{S(N)}{Z(p, N)}. \tag{3.13}$$

We will show that for any fixed p, R is greater than 1 for large enough N, thus demonstrating that there exist more SRGs than the p-particle walk can distinguish.

It is shown in [65] that there is a mapping between Latin squares of size n and SRGs of size n^2 with family parameters $(n^2, 3(n-1), n, 6)$. The results of [66, 65], imply that when N is large enough, the number of non-isomorphic Latin square SRGs of size N is bounded below by:

$$S(N) \geq \frac{1}{6}(\sqrt{N}!)^{2\sqrt{N}-3} N^{\frac{-N}{2}}. \tag{3.14}$$

As for $Z(p, N)$, we show in Appendix B that for a fixed p, Z satisfies the inequality:

$$Z(p, N) < N^{2X_p(p+1)}, \tag{3.15}$$

where X_p is the number of unique values a Green's function for a p-boson walk can assume. While it can be shown that X_p is super-exponential in p, it does not depend on N. This is because the value of a Green's function for a non-interacting p-particle QRW on an SRG is determined by a configuration of up to $2p$ vertices in that SRG, as discussed in Section 3.3 and Appendix A.

To examine the behavior of R in the limit of large N, we use Stirling's formula:

$$x! = \sqrt{2\pi} e^{-x} x^{x+1/2}(1 + O(x^{-1})). \tag{3.16}$$

This allows us compute a lower-bound for R in the limit of large N:

$$\lim_{N\to\infty} R \geq \frac{1}{6}(2\pi)^{\sqrt{N}-\frac{3}{2}} e^{-2N+3\sqrt{N}} N^{\frac{N}{2}-\sqrt{N}-\frac{3}{4}-2X_p(p+1)}. \tag{3.17}$$

Taking the logarithm of Eq. (3.17) yields:

$$\lim_{N\to\infty} \log R(p, N) \geq \lim_{N\to\infty} \frac{N}{2} \log N + O(N), \tag{3.18}$$

which diverges as $N \to \infty$. Therefore, for a fixed p, R approaches ∞ as N increases, showing that no p-particle non-interacting walk can distinguish all SRGs.

One can let p grow slightly with N and achieve the same result. Indeed, we show in Appendix C that

$$\log_2(X_p) = p^2 + O(p \log p). \tag{3.19}$$

Using this, we find our argument remains valid for
$p < C\sqrt{\log_2 N}$, for any $C < 1$.

We can contrast these results to those of Gamble *et al.*. They found that the hard-core two-boson walk distinguished all graph pairs in a dataset of over 500 million pairs of SRGs [3]. This distinguishing power was shown to arise from an underlying algebra that is fundamentally different than that of the noninteracting two-boson or two-fermion walks. As we see no obvious way to extend the proof presented in this section to include hard-core walks, it is an open question as to whether or not the two-boson hard-core walk has universal distinguishing power on SRGs. Even if does not, it is still possible that there exists a fixed $p > 2$ such that the p-boson hard-core walk could distinguish all SRGs. If this is the case, then this would be a marked difference between the non-interacting and hard-core walks.

3.4 Discussion

We have shown how three-particle non-interacting quantum random walks are qualitatively different from two-particle non-interacting quantum random walks; the latter will always fail to distinguish non-isomorphic strongly regular graphs from the same family, whereas the former successfully distinguish many (but not all) non-isomorphic pairs of strongly regular graphs. We have analytically identified a fundamental difference between these two classes of quantum walks. The three-particle walks have potential distinguishing power because the shared connectivity of triples of vertices in SRGs is not governed by the SRG family parameters. We have also demonstrated numerically that three-particle non-interacting walks have significant, but not universal, distinguishing power on SRGs. We observe numerically that bosonic and fermionic walks distinguish the same pairs of non-isomorphic pairs of graphs. Increasing the number of non-interacting fermions to four further increases distinguishing power. However, this distinguishing power is not limitless; we have shown that for any fixed number of non-interacting particles, there exist non-isomorphic pairs of SRGs that cannot be distinguished.

Lastly, we discuss the implications of these results in terms of the computational complexity of the graph isomorphism problem. Not only are there graph pairs on which the three- and four-particle walks fail, but we know that for any fixed particle number, there will be SRGs that such non-interacting walks cannot distinguish. It is still possible that, given any non-isomorphic SRG pair of a fixed size N, there exists a p such that the p-particle non-interacting walk will succeed in distinguishing the graphs. However, the lower bound given at the end of Section 3.3 rules out the possibility of our algorithm providing a classical polynomial-time solution to GI for SRGs.

Chapter 4

Power law scaling for the adiabatic algorithm for search engine ranking

4.1 Introduction

Quantum algorithms, which run on quantum computers, are known to be able to outperform classical algorithms for certain computational problems [35, 67]. Thus, finding a new algorithm that exhibits a quantum speedup, in particular an exponential speedup, is of great interest [68]. An extremely important problem in computer science is calculating ranking for search engine results. PageRank, first proposed by Brin and Page [69] underlies the success of the Google search engine [70]. In this algorithm, websites are represented as nodes on a network graph, connected by directed edges that represent links. The matrix of network connections is constructed, and the PageRank vector is its principal eigenvector. Currently, computing the PageRank vector requires a time $O(n)$, where n is the number of websites in the network considered (e.g. the World Wide Web) [71]. Obtaining a quantum algorithm for PageRank that runs exponentially faster than the classical algorithm would be of great interest.

Recently, Garnerone, Zanardi, and Lidar (GZL) proposed an adiabatic quantum algorithm [72] to prepare the PageRank vector for a given network [71]. Remarkably, GZL

present evidence that this algorithm can prepare the PageRank vector in time $O\left[\text{polylog}(n)\right]$, exponentially faster than classical algorithms for certain networks. This runtime is due to the apparent logarithmic scaling of the gap between the two smallest eigenvalues of the Hamiltonian used in the algorithm (the energy gap). This scaling emerged on graphs constructed using adapted versions of two established methods of network construction: the preferential attachment model [73] and the copying model [74]. Both of these models yield graphs that are similar to the connectivity of the World Wide Web in that they are sparse (the total number of edges scales at most proportionally to the number of nodes) and scale-free (the probability of finding a node with a specified in- or out-degree scales as a power law in those degrees). These features lead to networks that exhibit large-scale structure similar to that of the internet, such as being small-world [75] and loosely hierarchical [76]. GZL studied sets of networks that exhibited both logarithmic scaling and polynomial scaling of the gap in the system size. However, they did not demonstrate that the networks with the favorable logarithmic gap scaling are scale-free over the region studied numerically.

Here, we study the scaling of the GZL algorithm for graphs with degree distributions consistent with the internet. A realistic network model of the World Wide Web must be scale-free in both the in- and the out-degree [77, 78]. We consider a broad variety of scale-free networks constructed by different methods. Choosing three well-known models for constructing random, scale-free networks, we control for both the mean degree and the exponent of the power-law governing the degree distribution. We find that graphs with the same degree distribution can have different energy gap and run-time behaviors. Finally, we focus on degree distributions described by power laws consistent with those measured for the Web, both for the in-degree and the out-degree. We find that the relevant energy gap scales as a power of the system size, rather than logarithmically. These results demonstrate that for Web-like graphs, the GZL adiabatic algorithm does not yield an exponential quantum speedup for preparing the PageRank vector compared to current classical algorithms.

4.2 Network growth models

We generate samples of graphs with prescribed degree distributions using three different network growth models. GZL [71] use modified versions of two network construction algorithms: the preferential attachment model [73] and the copying model [74]. In addition to these two models, here we include also the more complex α-preferential attachment model described by Bollobás *et al.* [77, 79]. All three models grow random networks using probabilistic rules at discrete construction steps, which are detailed in Fig. 4.1.

All three of these models produce sparse, scale-free directed networks, in which the probability of the in-degree (the number of incoming edges) and out-degree (the number of outgoing edges) of node i being equal to k are each proportional to a power law:

$$P(d_{in}(i) = k) \sim k^{-\gamma_{in}} \tag{4.1}$$

$$P(d_{out}(i) = k) \sim k^{-\gamma_{out}}, \tag{4.2}$$

where $d_{in}(i)$ and $d_{out}(i)$ are the in- and out-degrees of node i, respectively, and the exponents γ_{in} and γ_{out} are typically between 2 and 4 [73]. The GZL versions [71] of the preferential attachment and copying models [73, 80] produce networks that are scale-free in the limit of large graph size. However, due to the addition procedure described below, the networks are not necessarily scale-free for the sizes of graphs studied numerically here and in Ref. [71]. To achieve networks that are scale-free in the out-degree, GZL suggest to construct two networks, X and Y, independently. X and Y are each generated as in Fig. 4.1, except that for Y the direction of the edges added is reversed. The networks can then be added together, and the weights and loops discarded [71, 81]. The resulting composite network is scale-free in both in-degree and out-degree, provided X and Y have the same number of edges per node. (See Appendix C for details.) In contrast to Ref. [71], the graphs studied here are all constrained in this way. However, the graphs exhibiting logarithmic scaling in [71] are not so constrained [81], and so they do not exhibit truly scale-free degree distributions over the numerically studied region. On the other hand, the α-preferential attachment model (considered here but not in [71]) constructs a network which is scale-free

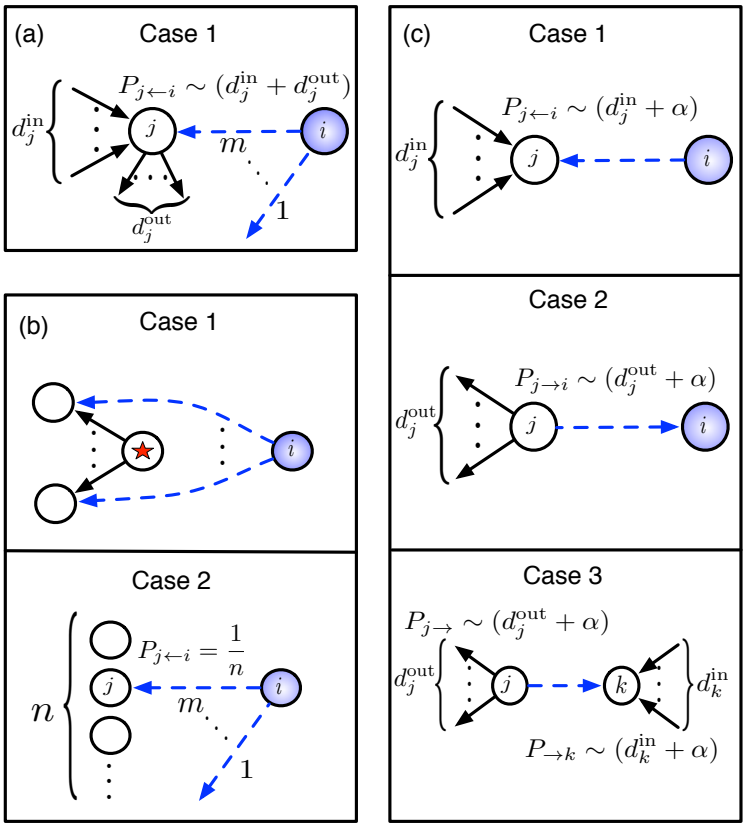

Figure 4.1: Illustrations of the three network generation models used. (a): GZL [71] preferential attachment, (b): GZL copying, and (c): α-preferential attachment [77, 79]. In all three models, a network is constructed by adding vertices and edges sequentially. (a): At each time step a new vertex i is added with m outgoing edges. The probability that one of these edges connects to a node j is proportional to the total degree of j. (b): At each time step there are two possible actions. With probability $(1-p)$, the new vertex points to all of the same vertices as the "star vertex," which is a pre-existing vertex chosen uniformly at random at each time step. With probability p, m outgoing edges are added to the new vertex, each pointing to vertices chosen uniformly at random. (c): There are three possible actions at each time step. With probability p_1, a new vertex is added with a single outgoing edge, pointing to a node j with probability proportional to the in-degree of j plus a parameter α. With probability p_2, a new vertex is added with a single incoming edge, pointing from a node j with probability proportional to the out-degree of j plus α. With probability $(1-p_1-p_2)$, no vertex, only an edge, is added. Its ending and starting points are determined as in cases 1 and 2, respectively. In all panels, the newly-added edges are indicated by dashed lines.

in both in- and out-degrees without requiring an additional combination step. As with the GZL preferential attachment model, all weights and loops are removed from the final α-preferential attachment network.

The exponents γ_{in} (Eq. 4.1) and γ_{out} (Eq. 4.2) of the degree distribution are model-dependent. In the GZL preferential attachment model the number of edges added at each construction step controls the sparsity, and it is always the case that $\gamma_{in} = \gamma_{out} = 3$ [73]. Both the GZL copying model and α-preferential attachment allow for independently tunable exponents and mean degree. (See Appendix C for details.) This flexibility enables us to create three ensembles of model networks that have nearly identical degree distributions for $\gamma_{in} = \gamma_{out} = 3$. Further, the last two models can be set with the exponents estimated for the World Wide Web [74, 77], namely $\gamma_{in} = 2.1$ and $\gamma_{out} = 2.72$ [78].

4.3 Algorithm description

The Google matrix is constructed by taking as input an unweighted, simple network with n nodes [69], and representing it as an adjacency matrix A, where $A(i, j) = 1$ if a directed edge points from node i to node j, and 0 otherwise. From this, one defines the matrix P:

$$P(i,j) = \begin{cases} 1/d_{out}(i) & \text{if } A(i,j) = 1 \quad (4.3a) \\ 1/n & \text{if } \forall j, A(i,j) = 0 \quad (4.3b) \\ 0 & \text{otherwise} \quad (4.3c) \end{cases}$$

The matrix P is stochastic because $\sum_j P(i, j) = 1$ for all i. P can be thought of as a random walk (i.e. a web-surfer), where the walker follows the network with equal likelihood of traversing all allowed links. If the walker ever reaches a dangling node (a node with $d_{out} = 0$), Eq. 4.3b implies that it can randomly hop to any vertex with equal probability. To prevent the walker from becoming trapped in an isolated portion of the network (a sink), the probability $(1 - \alpha_g)$ of moving to a node uniformly at random (including the possibility of staying still) is included, where $0 < \alpha_g < 1$; Google uses $\alpha_g = 0.85$, which we also use here [71]. The Google matrix G is defined as the transpose of this resulting transition matrix:

$$G = \alpha_g P^T + (1 - \alpha_g) J, \tag{4.4}$$

where J is the matrix of all ones. The PageRank vector $\vec{p}$ is the unique eigenvector associated with the largest eigenvalue of G, which is 1. The runtime of the best classical algorithm, which calculates the PageRank vector via power iteration, is $O(n)$ [69, 71].

To formulate an adiabatic quantum algorithm, GZL construct the Hamiltonian $h(G)$:

$$h(G) = (\mathbb{I} - G)^\dagger (\mathbb{I} - G), \tag{4.5}$$

which is Hermitian, even though G is not. The ground state of this Hamiltonian is the normalized PageRank vector. The adiabatic algorithm is completely defined by the interpolation Hamiltonian $H(s) = sh(G) + (1 - s)h(G_c)$, where $s \in [0, 1]$, and G_c is the Google matrix for the complete network (including loops), whose ground state is a uniform superposition. The adiabatic theorem guarantees that if we initialize our system in the ground state of $h(G_c)$ and change s from 0 to 1 sufficiently slowly, the system remains in the ground state [72]. Since the PageRank vector is the ground state of $H(1) = h(G)$, the PageRank vector is obtained when $s = 1$. The required slowness is also determined by the adiabatic theorem: as long as $s(t)$ is a smooth function of the time t with $0 \leq t \leq T$, the runtime $T \sim \delta^{-b}$, where b is $O(1)$ and δ is the energy gap between the ground and first excited state of $H(s)$, minimized over s [72]. Thus, an exponential speedup over the classical case is possible if δ^{-1} is $O[\log(n)]$, since then T is $O[\text{polylog}(n)]$.

4.4 Numerical results

To study the scaling of the minimum energy gap δ with the network size n, we compute δ for the GZL Hamiltonian $H(s)$, averaging the results over many network realizations (typically 1000). Specifically, we calculate the minimum value of δ over $s \in [0, 1]$ using the Nelder-Mead method [82], where each objective function call calculates directly the eigenvalue spectrum of $H(s)$. We find that for most, but not all, network choices the minimum gap occurs when $s = 1$. Since $H(s)$ is a dense matrix, this process is computationally intensive.

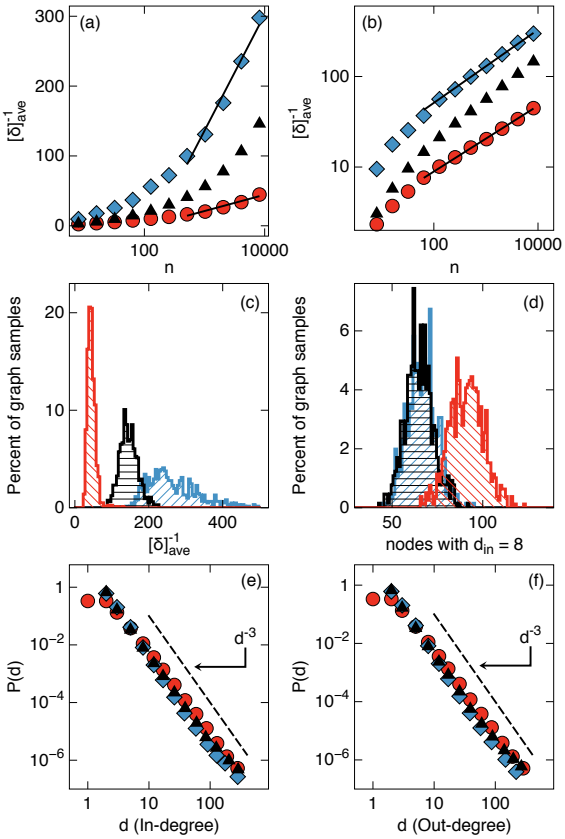

Figure 4.2: Comparison of the scaling of the inverse energy gap δ^{-1} for the GZL [71] preferential attachment model (triangles, horizontal hatching), GZL copying model (diamonds, upward-sloping hatching), and α-preferential attachment model [77] (circles, downward-sloping hatching), shown on (a): Semilog and (b): Log-Log scales, demonstrating that δ^{-1} is not proportional to $\log(n)$ for these models. Results are averaged over 1000 random instances for $n < 8192$, and over 500 random instances at $n = 8192$. The fitting lines showed in (a) are $72.2 \cdot \ln(n) - 363$ for the copying model and $10.1 \cdot \ln(n) - 48.8$ for the α-preferential attachment model. In (b), the fits shown are $8.0 \cdot n^{0.4}$ for the copying model and $1.7 \cdot n^{0.4}$ for the α-preferential attachment model. If we fit the data instead to a power of a logarithm (not shown), we obtain $0.56 \cdot \ln^{2.9}(n)$ for the copying model and $0.18 \cdot \ln^{2.5}(n)$ for the α-preferential attachment model. (c): Histogram of the inverse energy gaps for the data shown in panels (a)-(b) at $n = 8192$. (d): Histogram showing the distribution of number of vertices with in-degree $d_{in} = 8$ for $n = 8192$. (e)-(f): Degree-distributions of the three models, demonstrating scale-free behavior and indicating that $\gamma_{\text{in}} = \gamma_{\text{out}} = 3$. Adaptive binning was used, as described in Appendix C. In all cases, both the mean in- and out-degree of each graph are 2 edges per node. These results demonstrate that δ^{-1} differs significantly for the different graph construction methods, while the degree distributions are very similar.

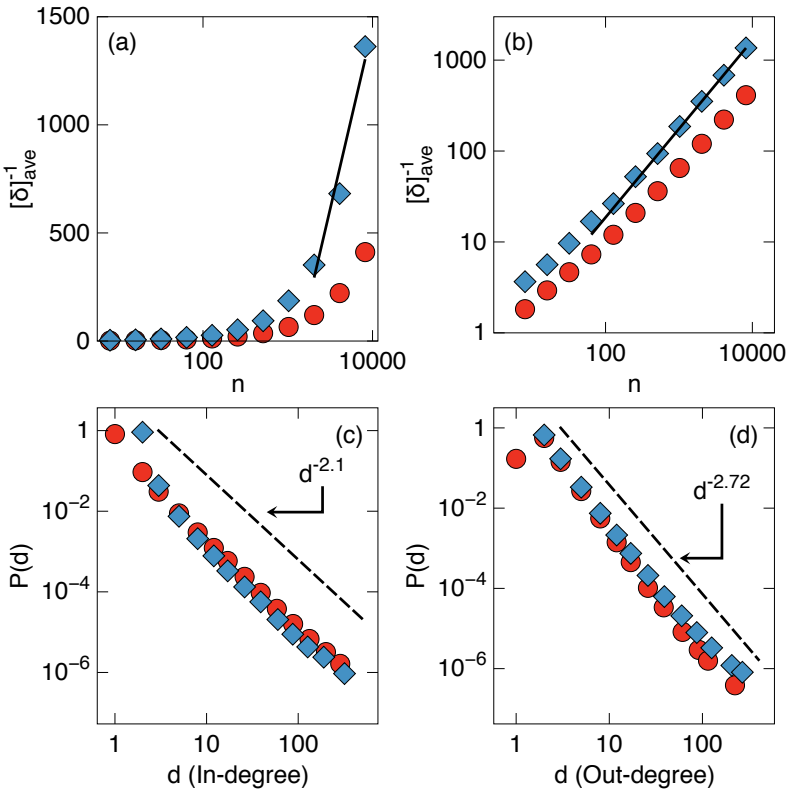

Figure 4.3: Inverse energy gap scaling for GZL [71] copying model (diamonds), and α-preferential attachment model [77] (circles) of WWW-like networks, shown on (a): Semilog and (b): Log-Log scales. Results are averaged over 1000 random instances for $n < 8192$, and over 500 random instances at $n = 8192$. In (a), the line fit shown is $730 \cdot \ln(n) - 5300$, while in (b) the line fit is $0.2 \cdot n^{0.97}$. If we fit the data to a power of a logarithm (not shown), for the copying model we obtain $3 \times 10^{-5} \cdot \ln^{8.0}(n)$. Because of the large power of the logarithm required for the polylogarithmic fit, the power-law dependence on n appears more natural and plausible. (c)-(d): Degree-distributions of the two models, histogrammed using adaptive binning (see Appendix C), indicating that $\gamma_{\text{in}} = 2.1$ and $\gamma_{\text{out}} = 2.72$, corresponding to the estimates for the degree distribution of the World Wide Web [78]. In all cases, the mean in- and out-degree of each network were each 2 edges per node.

We use the University of Wisconsin-Madison Center for High Throughput Computing and Open Science Grid to perform the simulations.

To assess whether the inverse energy gap δ^{-1} scales logarithmically or as a power-law in n, we plot in Fig. 4.2 δ^{-1} versus the network size on both log-linear and log-log scales, with data for the GZL preferential attachment, GZL copying, and α-preferential attachment models. The model parameters are tuned (see Appendix C) so that all three

have $\gamma_{in} = \gamma_{out} = 3$ and have an average of 2 in- and 2 out-edges per node. Despite having nearly identical degree distributions (shown in Figs. 4.2(e) and 4.2(f)), the scaling of δ^{-1} depends significantly on the method used to construct the graphs when viewed in Fig. 4.2(a). In Fig. 4.2(c), we show the distribution corresponding to the final data points in Fig. 4.2(a), where we see that the distributions are well-separated and hence the construction models give different values of δ^{-1}. By contrast, the degree distributions are difficult to distinguish, as shown in Fig. 4.2(d). Finally, we conclude that for all three models, the data are more consistent with δ^{-1} scaling as a power law or a high-order polylogarithm, rather than a logarithm, as consistent with the data presented by GZL in the supplemental information of Ref. [71].

We next perform a similar analysis for degree distributions more closely related to the network of primary interest, the World Wide Web, for which a realistic set of degree parameters is given by $\gamma_{in} = 2.1$ and $\gamma_{out} = 2.72$ [78]. As mentioned above, the preferential attachment model cannot be tuned to obtain degree parameters other than 3. However, the other two network models can be adjusted to match these values [74, 77]. More details on this are discussed in Appendix C. As before, we set the mean degree to be 2 in- and 2 out-edges per node.

Fig. 4.3 presents the results of these simulations, clearly indicating that δ^{-1} scales at least as a power of n. In particular, we note that the prefactor of the logarithmic fit is over 700 and the power of the logarithm in the polylogarithmic fit is 8, while the power law fit exponent is close to one. The results do not change substantially when the mean degree is varied and the degree distributions exponents are fixed. These data indicate that for graphs with degree distributions similar to those measured for the World Wide Web, the GZL adiabatic algorithm for PageRank vector preparation is unlikely to provide an exponential speedup over the classical case.

4.5 Discussion

We have investigated the recently proposed adiabatic quantum algorithm for preparing the PageRank vector using an adiabatic quantum algorithm [71]. We find that the eigenvalue gap that determines the algorithm runtime depends on the method of construction of the network, even when the feature believed to be critical for large-scale network structure, the degree distribution, is held fixed. The exponent governing the variation of the gap with graph size does not vary significantly with the method of construction only if power-law scaling of the gap with size is assumed. For networks that are scale-free in their in- and out-degree distributions, and particularly when the degree distributions similar to those measured for the World Wide Web, our numerical results indicate strongly that the GZL adiabatic algorithm for PageRank vector preparation does not offer an exponential speedup over current classical algorithms.

Chapter 5

Cooling of cryogenic electron bilayers via the Coulomb interaction

5.1 Introduction

As researchers continue to probe smaller electronic devices at lower temperatures, a detailed understanding of heat management applicable on such length and energy scales becomes increasingly important. For example, recent experiments to detect the spin resonance of a single electron [83] and to perform fast charge sensing in few-electron quantum dots [84] are both limited by heating effects. Other applications, such as the search for the $\nu = 5/2$ non-abelian quantum Hall state, are expected to require very low temperatures [85], making the development of schemes for cooling such devices a necessary challenge.

The main problem is that whenever current is applied to a device to perform a measurement, the conduction electron temperature increases due to Joule heating [86]. In devices operating near room temperature, heat can be readily dissipated through phonons, as the conduction electrons and lattice are strongly coupled. However, as temperature is decreased, the conduction electrons decouple from the lattice. The phonon modes contribute less and

less to cooling because the phonon density of states decreases as energy is decreased [87]. Hence, as the system gets colder, it becomes more difficult to cool via conventional means.

Besides phonon cooling, systems can be cooled by electron diffusion through the leads [88]. However, in common nanoscale devices, the leads extend hundreds of microns from critical regions to regions that are well cooled. This large distance scale limits the effectiveness of electron diffusion for device cooling [88].

Here, we investigate using the Coulomb interaction directly, a strategy for cooling that remains largely unexplored. Electron diffusion through grounded, close proximity leads can effectively cool samples to about 10 mK [89]. However, experiments with electrically sensitive structures, such as quantum dots [84], make this direct cooling impractical. To bypass this problem, we consider placing a cold conductor nearby the hot conduction electrons, using the Coulomb interaction for heat transfer. In analogy with a macroscopic heat exchanger, the cold conductor is a heat sink for the hot conduction electrons, enabling cooling without electrical disruption to the experiment. It is important to note that lowering the electron temperature of the 2DEG is of crucial importance to quantum dot experiments, even though the dot electrons are typically isolated from the leads. This is because increased electron temperature results in thermal-broadening in charge sensing measurements[86], as well as phonon-mediated backaction in the dot [90].

While it may seem that remote Coulomb interactions are not strong enough to facilitate meaningful power transfer, several recent experiments have shown that remote interactions can indeed drastically affect electron relaxation. For instance, the widely studied Coulomb drag (CD) effect [91, 92, 93] involves the transfer of momentum from one two-dimensional electron gas (2DEG) to another via the Coulomb interaction, due to the layers' close proximity. Another example of the importance of remote Coulomb interactions arises in the metal-oxide-semiconductor (MOS) geometry, where it has been found that device performance can be reduced due to interactions of the conduction electrons with those in the gate when the distances are too small [94, 95, 96].

In this chapter, we consider two parallel, silicon 2DEGs, separated by tens of nanome-

ters. We make the simplifying approximation that both 2DEGs are of zero thickness. Similar devices have been implemented experimentally in the form of silicon electron-hole bilayers [97, 98]. One of the layers is taken to have a temperature on the order of tens to hundreds of mK; this is the active layer that we are interested in cooling. The second, auxiliary layer is taken to be the heat sink, and is assumed to be at temperature $T = 0$ K. As we mentioned, the auxiliary layer can be effectively cooled through close proximity, grounded leads. Since the two layers are electrically decoupled, this would not interfere with electrical measurements on the active layer.

We study the temperature, separation, and carrier density dependencies of the heat transfer, and compare it to experimental results for heat dissipation due to phonons. The Coulomb interaction is found to be competitive and even dominant over phonons for a range of temperatures and densities, for separations up to several tens of nanometers. Specifically, we find that lowering the electron density enhances the power transfer due to the Coulomb interaction, but decreases the power dissipation due to phonons.

This chapter is organized as follows. Section 5.2 uses a formalism similar to that used for CD to formulate the physical problem. Next, Sec. 5.3 finds an expression for the power transfer and discusses its asymptotic behavior in both near and far distance regimes. Section 5.4 compares the results of the previous sections to experimental results for phonon-mediated cooling. Finally, Sec. 5.5 discusses the implications of cooling nanosystems using carrier-carrier interactions, and suggests directions for future study.

5.2 Formulation of the problem

In this section, we describe the physical situation we will consider throughout this chapter: two parallel 2DEGs, one serving as a heat sink for the other. We then review the standard scattering formalism that is used to perform Coulomb drag (CD) calculations. Using this Boltzmann transport formalism, we write down an equation for power transfer, which we will evaluate in subsequent sections.

The physical situation we consider here is very similar to that which has been well-

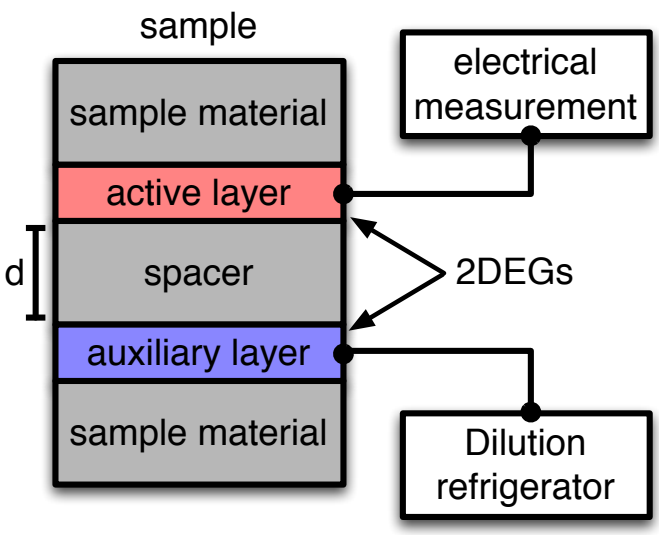

Figure 5.1: Illustration of our proposed cooling scheme. Two 2DEGs, an active layer and an auxiliary layer, are separated by a distance d. The active layer is involved in an electrical experiment, and is heated by hot electrons that enter the sample through the measurement leads. The auxiliary layer is wired to the dilution refrigerator, and is held at its base temperature. Heat is transferred from the active to auxiliary layer via the Coulomb interaction. For mathematical simplicity, in this work we take the sample material, spacer, and both layers to be Si. Further, we approximate the two 2DEGs to have zero thickness.

studied in the CD literature [91, 92, 93, 99]. Specifically, we have a sample that contains two 2DEGs that are parallel but spatially separated by some distance d. In the case of CD, one of the 2DEGs is driven by a current, while the other is not. Because of the current flow, the distribution function in the active layer is out of equilibrium, and the resulting charge fluctuations generate a response in the auxiliary layer, mediated by the Coulomb interaction between the layers. Although complicated by screening, the basic picture is that the presence of the current in the active layer "drags" electrons in the auxiliary layer, creating a net voltage.

In our case, we do not consider the non-equilibrium effects of a current flowing. Rather, we suppose that each layer is internally at thermal equilibrium, but at different temperatures. We will consider the active layer to be at a finite temperature T, and the auxiliary layer (the heat sink) to be at $T = 0$ K. Intuitively, we expect that energy should be

transferred from the active layer to the heat sink. Microscopically, this is due to density fluctuations in the hot, active layer causing responses in the cold, auxilary layer, mediated by the Coulomb interaction. Fortunately, we can borrow much of the initial setup of the problem from the CD formalism. However, the evaluation of the resulting expression is quite different because we focus on energy between 2DEGS of unequal temperature, rather than momentum transfer due to a driving electric field. In Fig. 5.1, we show an illustration of our proposed cooling cooling scheme.

Since we will be working at very low temperatures (< 1 K), binary Coulomb collisions are the primary method of heat transfer between layers. If we were to consider temperatures $T \gtrsim 0.2E_F/k_B$, where E_F is the Fermi energy, we would also need to take into account collective scattering effects, the so-called plasmon enhancement [99]. Hence, we consider interactions that transfer energy from an electron in the active layer 2DEG to an electron in the auxiliary layer 2DEG. Below, we denote quantities for the active layer with a subscript one, and quantities for the auxiliary layer with a subscript two. The electrons involved in the interaction have initial (2D) momenta $(\mathbf{k}_1, \mathbf{k}_2)$ and final momenta $(\mathbf{k}_1', \mathbf{k}_2') = (\mathbf{k}_1 + \mathbf{k}, \mathbf{k}_2 - \mathbf{k})$, where $\mathbf{k}$ is the transferred momentum. This carrier-carrier scattering falls into the category of distinguishable particle scattering since events only occur between particles in different layers. The formalism for treating such a scattering problem is well known [100], and the power transfer is shown in appendix D.1 to be

$$P = \frac{16A^3}{(2\pi)^6} \int d^2k_1 d^2k_2 d^2k \cdot E \cdot \Gamma, \tag{5.1}$$

where A is the sample area, E is the transfer energy for an individual event, and Γ is the scattering rate. In the next section, we evaluate Eq. (5.1) using the Thomas-Fermi approximation to describe screening (which in this context is equivalent to the RPA approach taken in Ref. [99]).

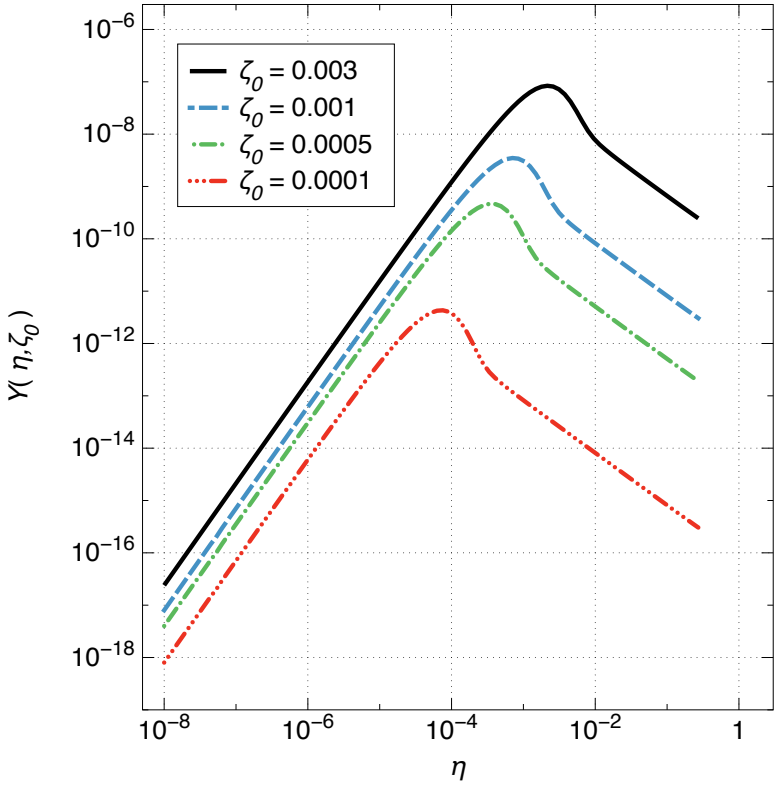

Figure 5.2: The dimensionless function $Y(\eta, \zeta_0)$ (Eq. (5.3)) plotted over η for various values of ζ_0 and with layer densities $n_1 = n_2$. Here, $\eta = k/k_F$ is a scaled momentum and $\zeta_0 = k_B T/E_F$ is the characteristic magnitude of energy fluctuations due to temperature. The function follows a power law for both low and high η, with a maximum occurring for an intermediate η, which we denote as η^*.

5.3 Results

In this section, we evaluate Eq. (5.1), using some standard methods incorporated into the calculation of CD. However, the resulting expression is quite different, so we work through its derivation in appendix D.3. We set the temperature of the active layer to T, the temperature of the auxiliary layer to absolute zero, the Fermi level of the active layer to E_F, and the Fermi level of the auxiliary layer to E_F/x, where $x = n_1/n_2$, the ratio of carrier densities between active and auxiliary layers. The power transfer is then

$$\frac{P}{A} = \frac{E_F^4}{64\hbar}\left(\frac{\epsilon_0\epsilon_b}{q^2}\right)^2 \int d\eta \left(\frac{\eta}{\sinh(\eta/\eta_0)}\right)^2 Y(\eta, \zeta_0), \tag{5.2}$$

where

$$
\begin{aligned}
Y(\eta,\zeta_0) = \int_0^\infty d\zeta \frac{\zeta}{\eta^3}\left[\coth\left(\zeta/\zeta_0\right)-1\right] \\
\times \mathrm{Re}\Big(\sqrt{2(2+\zeta)\eta^2-\eta^4-\zeta^2} \\
-\sqrt{2(2-\zeta)\eta^2-\eta^4-\zeta^2}\Big) \\
\times \mathrm{Re}\Big(\sqrt{2\left(\frac{2}{x}+\zeta\right)\eta^2-\eta^4-\zeta^2} \\
-\sqrt{2\left(\frac{2}{x}-\zeta\right)\eta^2-\eta^4-\zeta^2}\Big),
\end{aligned}
\tag{5.3}
$$

and the dimensionless parameters are $\zeta \equiv E/E_F$, $\eta \equiv k/k_F$, $\zeta_0 \equiv k_BT/E_F$ and $\eta_0 \equiv 1/(k_Fd)$, with $k_F = \sqrt{2m^*E_F}/\hbar$ the Fermi momentum. Here, the $\eta/\sinh(\eta/\eta_0)$ term is due to the interlayer Coulomb interaction (Eq. (D.5)), while the distribution functions give rise to $Y(\eta,\zeta_0)$.

The function $Y(\eta,\zeta_0)$ is plotted in Fig. 5.2, where it is shown that Y is a peaked function in η varying as a power of η on either side of the peak. We define η^* to be the location of the peak, and note that $\eta^* \approx \zeta_0$. Physically, $Y(\eta,\zeta_0)$ tracks the availability of energy fluctuations corresponding to a particular momentum transfer $k = \eta k_F$ and temperature $k_BT = \zeta_0 E_F$. If $\eta < \eta^*$, Y is limited by the Fermi-Dirac distributions that govern the occupation of states in each 2DEG. For $\eta > \eta^*$, Y is instead constrained by the temperature difference between 2DEGs.

From Eq. (5.2), we see that the Coulomb potential causes η to be cut off at approximately η_0. Hence, there are two asymptotic regions of interest: when $\eta_0 \ll \eta^*$ and when $\eta_0 \gg \eta^*$. In the first region, the Coulomb potential cuts off the integration over η well before η^*, which corresponds to large separations between 2DEGs. Here, the separation distance limits the magnitude of the momentum transfer, which in turn limits power transfer. For $\eta_0 \gg \eta^*$, the Coulomb interaction truncates the η integration after η^*, corresponding to small separation. In this regime, Y is already rapidly decreasing, so the power transfer is instead mainly constrained by the temperature difference between 2DEGs. The crossover between these two regions occurs when $\eta_0 \approx \eta^* \approx \zeta_0$, corresponding to a separation of

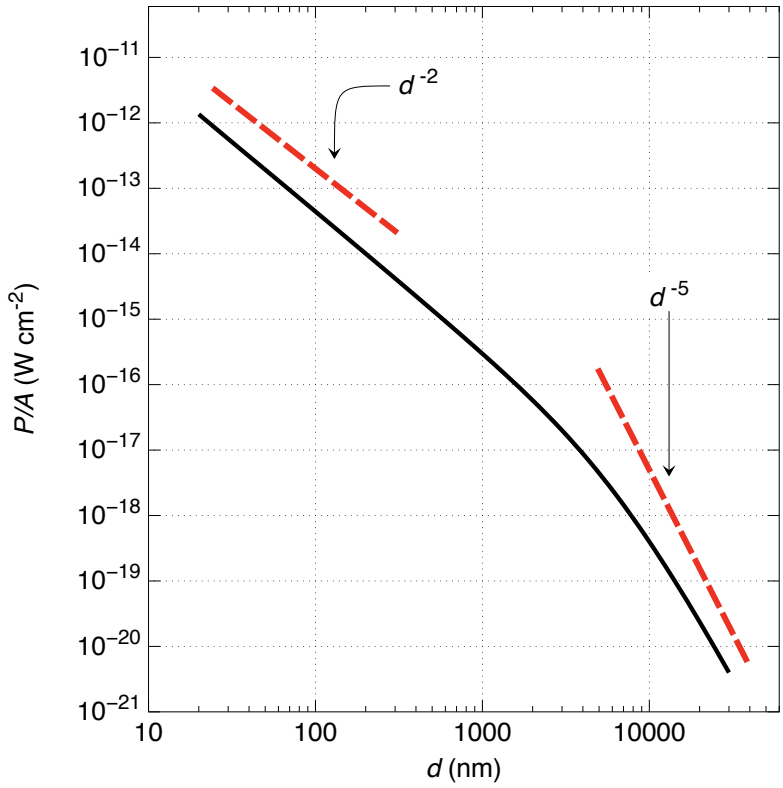

Figure 5.3: Calculated values for the power per unit area P/A transferred via the Coulomb interaction versus separation (Eq. (5.2)). Here, the sheet density is 4×10^{11} cm^{-2} in both layers, the temperature of the active layer is $T = 100$ mK, and the temperature of the auxiliary layer is 0 K. As can be seen by the dashed lines, the power transfer varies as approximately $1/d^2$ at small distances and $1/d^5$ at large distances. The crossover length scale occurs when $d \approx E_F/(k_F k_B T)$.

$d \approx E_F/(k_F k_B T)$.

In appendix D.4, we work out the asymptotic forms for power transfer. We consider the specific case of equal density 2DEGs, when $x = 1$. In the large separation regime when $d \gg E_F/(k_F k_B T)$, we find

$$\frac{P}{A} \sim \frac{k_F \hbar^5}{512 m^{*3}} \left(\frac{\epsilon_0 \epsilon_b}{q^2}\right)^2 \frac{k_B T}{d^5} \left[8.3 + 13.0 \cdot \log\left(k_F d\right)\right], \tag{5.4}$$

where we use ($\sim$) to denote asymptotic equivalence. For the short distance limit where

$d \ll E_F/(k_F k_B T)$, we have

$$\frac{P}{A} \sim \frac{\hbar}{128 E_F m^*} \left(\frac{\epsilon_0 \epsilon_b}{q^2}\right)^2 \frac{k_B^4 T^4}{d^2} \times \left[0.46 - 1.32 \cdot \log\left(\frac{k_B T}{E_F}\right) - 0.81 \cdot \log\left(k_F d\right)\right]. \tag{5.5}$$

Hence, up to logarithmic corrections, $P/A \propto T/d^5$ for large distances and $P/A \propto T^4/d^2$ for small distances, which can be qualitatively understood as follows. At low temperatures ($T \ll k_B E_F$), it is reasonable to assume that energy fluctuations are small and concentrated about the Fermi level, so that the transfer momentum obeys $k \ll k_F$. Expanding Eq. (5.3) for small η, while working in the large separation regime where $\eta \ll \eta^*$, we find that

$$Y(\eta, \zeta_0) \propto \zeta_0 \eta^2. \tag{5.6}$$

Here, the scaling is determined by the Fermi-Dirac distributions limiting the power transfer. Likewise, if we work in the small separation region where $\eta \gg \eta^*$, we find

$$Y(\eta, \zeta_0) \propto \frac{\zeta_0^4}{\eta}, \tag{5.7}$$

where the scaling is now determined by the layer temperature. In these limits, since the Coulomb interaction sets the scale of $\eta \propto \eta_0$, we can easily see the rough dependences (neglecting the logarithmic corrections) via power counting in Eq. (5.2). Fig. 5.3 shows the numerical evaluation of Eq. (5.2) as a function of separation, clearly demonstrating both distance regimes.

5.4 Comparison with cooling due to phonons.

In this section, we compare Coulomb-mediated cooling to experimentally measured energy dissipation due to phonons at low temperatures. In silicon-based heterostructures at low temperatures, two types of phonon couplings are important: acoustic phonons governed by a deformation potential coupling [101], and the Pekar coupling [102]. Pekar phonons arise from the sharp electrostatic confinement potentials present in heterostructure devices, such as quantum wells, and hence are not present in bulk samples [102]. They also share

a characteristic T^3 dependence with piezoelectric phonons [102], making them especially important in low-temperature experiments with non-polar materials, such as few-electron quantum dots in Si.

Indeed, both deformation potential and Pekar phonons have been experimentally observed in silicon-based heterostructures at low temperature [88]. The characteristic temperature dependence for deformation potential coupling is T^5 [101], so for very low temperatures we expect Pekar phonons to dominate, while for higher temperatures deformation potential phonons become more important.

As established in Eq. (5.5), for small separations the power transfer to the auxiliary layer via the Coulomb interaction varies as T^4. Whether or not this Coulomb cooling is larger than phonon cooling over a given temperature range depends on the numerical magnitude of Eq. (5.2), which we now compute. We compare Coulomb cooling to experimental measurements of phonon mediated cooling in Ref. [88]. There, it is found that the power dissipation due to phonons is $P_{ph}/A = aT^3 + bT^5$, where $a = 2.2 \times 10^{-8}$ W K^{-3} cm^{-2} and $b = 5.1 \times 10^{-8}$ W K^{-5} cm^{-2}. The structure used is a silicon MOS inversion layer, with dielectric thickness 200 nm and carrier density 5.4×10^{11} cm^{-2}.

It is known that the phonon couplings depend on the electron density, with $P \propto n^{-3/2}$ for the deformation potential coupling [101]. Pekar phonons have both an explicit $n^{-1/2}$ dependence and a dependence on the electric field at the 2DEG of F^2 [102]. Since in a 2DEG $F \propto n$ [103], Pekar phonons scale as $P \propto n^{3/2}$ in total. By comparison, Eq. (5.5) tells us that for equal density 2DEGs, Coulomb power transfer goes like $P \propto 1/n$.

Typically, in an experiment the density is fixed by desired electronic properties (for instance, the ability to pinch off current with depletion gates). For low-temperature applications that attempt to reach few-electron regimes, it is desirable to have a low density. It is therefore important to determine the dependence of power transfer on the density n. Fig. 5.4 shows the effect of varying the layer density on the power transfer, for three different layer separations at constant temperature $T = 50$ mK. As expected, the Coulomb power transfer is greatest in the case of small density, making it especially pertinent for

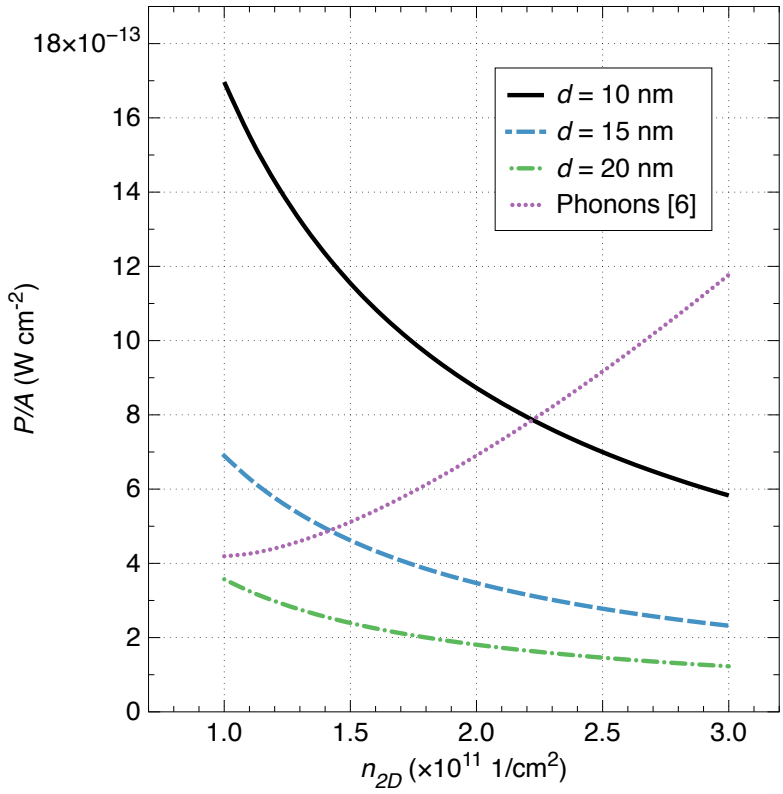

Figure 5.4: Calculated values for the power per unit area P/A transferred between an active ($T = 50$ mK) and heat sink ($T = 0$ K) 2DEG via the Coulomb interaction as a function of the layer density at three different values for the separation between layers. Here, the densities of both layers are identical. For comparison, P/A due to phonons from experimental data in Ref. [88], scaled for changing density, is shown as a dotted line.

few-electron experiments.

It is important to note that our formalism for static screening is only valid when the transfer momentum obeys $k < 2k_F$,[103] which means that our we cannot make the density too small. The Coulomb interaction limits the transfer momentum to $k \lesssim 1/d$. Hence, setting $k = 1/d$ for $d = 10$ nm corresponds to $n > 0.79 \times 10^{11}$ cm^{-2}. Another constraint on low-density 2DEGs is the metal-insulator transition, which occurs for sufficiently low densities. In silicon MOS structures, the critical value of density is known to be around $n_c \approx 1 \times 10^{11}$ cm^{-2} [104]. More recently, calculations for dopantless Si/SiGe devices predict that this value can be much lower, about $n_c \approx 2 \times 10^{10}$ cm^{-2} [105].

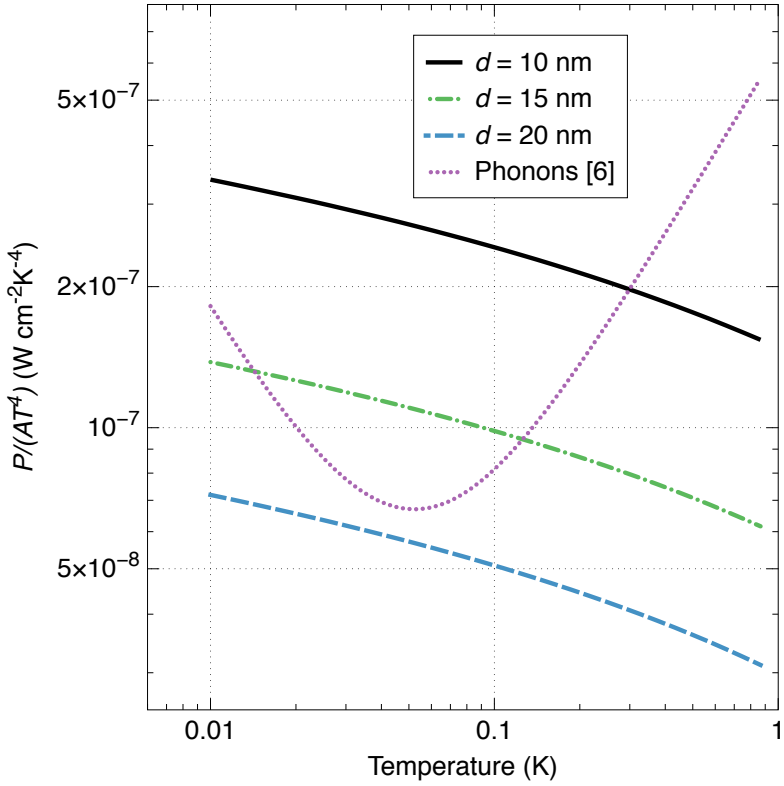

Figure 5.5: Values for the power per unit area scaled by T^4, $P/(AT^4)$, transferred via the Coulomb interaction between two 2DEGs versus temperature at three different values for the separation between the layers. For comparison, the scaled $P/(AT^4)$ due to phonons from experimental data in Ref. [88] is shown. The density of both layers is $1 \times 10^{11}/\mathrm{cm}^2$.

In Fig. 5.5, we plot the temperature dependence of the power transfer per unit area P/A for several separations, and compare with the power dissipation due to phonons. There, we fix the carrier density to be $n = 1 \times 10^{11}$ cm^{-2} for both layers. One sees that for small separations (less than 20 nm), Coulomb-mediated power transfer exceeds phonon power dissipation over a potentially wide temperature range (roughly up to 300 mK for a 10 nm separation). For very low temperatures, phonons again become more important than Coulomb cooling. This is because the low temperature phonon cooling occurs through the Pekar mechanism and scales as T^3, while Coulomb cooling scales as approximately T^4.

5.5 Discussion

Understanding relevant heat dissipation mechanisms at low temperatures in electronic devices is an important problem, especially as spin-based, few-electron devices mature. In this chapter, we considered a geometry consisting of parallel 2DEGs in silicon and calculated the expression for power transfer between two layers at temperatures $T > 0$ and $T = 0$ respectively, in the approximation of Thomas-Fermi screening. We then presented analytic results for the asymptotic regimes of small and large separations. We showed that in this geometry, power transfer due to the remote Coulomb interaction can be the dominant heat loss mechanism. This Coulomb cooling is most effective at low densities, making it especially important for experiments attempting to access few-electron regimes.

There have been a number of studies of heat transfer between close bodies, including a semiclassical kinetic treatment by Boiko and Sirenko [106] and an electromagnetic formulation by Volokitin and Persson [107, 108]. However, these are largely interested in hot devices, where complicating features such as plasma excitations are important. Further, as noted in Ref. [107], there are discrepancies between this electromagnetic formalism and Boltzmann transport approaches. More recent work by Krüger, Emig, and Kardar extends the electromagnetic formalism to arbitrary geometries with a focus on heat transfer [109]. It would be beneficial to compare the present work to the electromagnetic treatments to attempt to address the origin of any discrepancies.

While the results for two parallel 2DEGs are promising, one could almost certainly engineer a better geometry for optimizing heat dissipation. Indeed, the main reason for a preliminary evaluation of the 2DEG-2DEG geometry was due to its computational simplicity. An idea for a more effective heat sink might be a standard MOS geometry, or a top-gated nanostructure. Due to the drastically higher density of states in the metal, one could expect an enhanced power transfer. However, screening would also be enhanced, so careful calculations, similar to those presented in this chapter, should be done for that geometry. Also, studying the effects of high-k dielectrics might be fruitful, since the power transfer scales as ϵ_b^2.

Chapter 6

Two-electron dephasing in single Si and GaAs quantum dots

6.1 Introduction

Both Si and GaAs quantum dot technologies are now well-established as candidates for the implementation of scalable quantum computation [110, 111]. Working qubits have been fabricated with several different architectures involving singly-occupied dots, including the single-spin qubit architecture [2, 112, 113, 114, 115, 116, 117, 118, 119], the singlet-triplet scheme [120, 121, 122, 123, 111], and three-dot logical qubits [124, 125].

Recently, we proposed a new "hybrid" qubit architecture [8] with three electrons in two quantum dots that is potentially advantageous because fast qubit operations can be performed in a relatively simple nanostructure. Because the hybrid design is capable of all-electrical, fast qubit gates, the qubit wavefunctions have some charge character that gives rise to decoherence mechanisms that are not present in pure spin qubits. This means that characterizing decoherence becomes a more pressing issue, because charge decoherence is typically much faster than spin decoherence. In GaAs, the single-spin decoherence time T_2 has been measured to be 1 ns for charge qubit [126, 127], while T_2 for single-spin qubits has been measured to be greater than 100 μs [128].

In the singlet-triplet qubit, when there is a finite exchange-induced energy splitting between the singlet and triplet states, the dominant sources of decoherence have been found to be charge noise [129, 130, 131] and electron-phonon coupling [132]. Much of the physics of the hybrid qubit is similar to that of the singlet-triplet qubit, with the main differences in the decoherence properties arising because one of the dots contains two electrons. In the doubly-occupied dot, both electrons in a singlet can occupy the orbital ground state, while at least one of the triplet electrons must lie in an excited state. A further complicating factor in silicon-based quantum dot devices is the presence of two nearly degenerate, low-lying valley states [133, 134, 135, 136, 137, 138, 139, 140]. These levels are split near a sharp interface by an amount that is typically comparable to the orbital energy spacing. Hence, single-electron first excited states have two characteristic types: orbital, where the electron occupies the same valley state but the P-like first excited state of the lateral confinement potential, and valley, where the electron is in the orbital ground state and a higher valley state.

In this chapter, we calculate singlet-triplet dephasing rates in a doubly-occupied quantum dot, extending the spin relaxation calculations previously done for both GaAs [141] and Si [142] due to finite spin-orbit coupling and hyperfine coupling to nuclear fields. For GaAs, the singlet-triplet relaxation rate has been measured to be on the order of kHz for applied magnetic fields up to 6 T [143]. In Si, this rate has been measured to be on the order of Hz [8]. Unlike relaxation, pure dephasing is due to processes that conserve spin and does not involve energy exchange with the environment. For both electron-phonon coupling and charge noise, we consider the limiting cases of purely orbital (for both GaAs and Si) and purely valley (for Si) excited states.

We find that for GaAs, polar optical phonons are the main source of dephasing, leading to a decoherence rate of ~ 5.9 GHz. For Si, the phonon-mediated dephasing rate depends on the type of excitations supported by the quantum dot. For a first excited state that is orbital-like, intervalley optical phonons lead to a decoherence rate of ~ 140 kHz. For a valley-like first excited state, this same phonon channel results in a faster decoherence

rate of $\sim$ 1.1 MHz. For a perfectly harmonic, disorder-free dot, we find that dephasing due to charge noise is strongly suppressed. This is because the effective dipole moment between the singlet and triplet states vanishes for both orbital- and valley-like excitations. If we allow for anharmonicity and an effective dipole moment, we find that both phonon and charge noise dephasing channels are of similar strengths in Si, but phonons are the limiting mechanism in GaAs. Assuming a gate operation speed of 10 GHz (quite feasible for the hybrid qubit), the decoherence rate in silicon is consistent with the achievement of 10^4 operations per coherence time, while the decoherence rate in GaAs is too fast for viable hybrid qubit operation.

This chapter is organized as follows. In Sec. 6.2, we briefly review the quantum states that are relevant to the system considered in this chapter. Next, in Sec. 6.3 we formulate the problem of intra-dot singlet-triplet dephasing due to the electron-phonon coupling, following the formalism of Ref. [132]. We consider first GaAs, then both pure orbital and valley excitations in Si. In Sec. 6.4, we calculate dephasing due to charge noise, and compare to phonon-induced dephasing. Finally, in Sec. 6.5 we discuss the role that the dephasing mechanisms we have addressed are likely to play for qubits and suggest methods for mitigating decoherence.

6.2 Two-electron states in a quantum dot

The lowest energy eigenstates of two electrons in a single quantum dot (neglecting spin-orbit interaction) are the singlet

$$|S\rangle = |\psi_0\rangle \frac{|\uparrow\downarrow\rangle - |\downarrow\uparrow\rangle}{\sqrt{2}} \tag{6.1}$$

and the three triplet states

$$|T\rangle = |\psi_1\rangle \times \begin{cases} |\uparrow\uparrow\rangle & (T_+) \\ \left(|\uparrow\downarrow\rangle + |\downarrow\uparrow\rangle\right)/\sqrt{2} & (T_0) \\ |\downarrow\downarrow\rangle & (T_-) \end{cases}, \tag{6.2}$$

where $|\psi_0\rangle$ is the two-electron spatial ground state and $|\psi_1\rangle$ is the first excited state. If spin-orbit interaction is included, the charge density fluctuations considered in this chapter would have led to singlet-triplet relaxation as well, in addition to the calculated pure dephasing. However, based on existing spin relaxation calculations [142], we believe such relaxation would be a much weaker decoherence channel, especially considering that spin-orbit interaction is very weak in Si.

We work within the Heitler-London approximation;[132] in this approximation, $|\psi_0\rangle \approx |00\rangle$, indicating that both electrons are in their single-electron ground states, and $|\psi_1\rangle \approx (|01\rangle - |10\rangle)/\sqrt{2}$, where one electron is in its ground state and the other is in its first excited state. This chapter considers dephasing due to the electron-phonon coupling and charge noise, both of which conserve spin, so from here on we will focus on the spatial component, with the appropriate spin wavefunction understood. We refer to the triplets collectively as $|T\rangle$ when the particular spin configuration is not important.

In GaAs, the wavefunctions of the ground and first excited states have identical dependence on z (the direction perpendicular to the quantum well), but have S- and P-like transverse envelopes in the x-y plane (the plane of the quantum well). For a quadratic quantum dot confinement potential, the effective mass approximation for the ground state wavefunction is

$$\psi_0^{GaAs}(\mathbf{r}) = u(\mathbf{r})\frac{F(z)}{\sqrt{\pi}L}e^{-(x^2+y^2)/(2L^2)} \tag{6.3}$$

while the first excited state wavefunction is

$$\psi_1^{GaAs}(\mathbf{r}) = u(\mathbf{r})\frac{F(z)(x+iy)}{\sqrt{\pi}L^2}e^{-(x^2+y^2)/(2L^2)}, \tag{6.4}$$

where $u(\mathbf{r})$ is the periodic (with the lattice periodicity) component of the Bloch function at the conduction band minimum (the Γ-point in GaAs), $F(z)$ is the envelope function along z, and L is the lateral extent of the wavefunction.

For silicon, we write the ground state wavefunction as

$$\psi_0^{Si}(\mathbf{r}) = \phi_-(\mathbf{r})\frac{F(z)}{\sqrt{\pi}L}e^{-\frac{1}{2L^2}(x^2+y^2)}, \tag{6.5}$$

where

$$\phi_{\pm}(\mathbf{r}) = \frac{u_{+}(\mathbf{r})e^{ik_0 z} \pm u_{-}(\mathbf{r})e^{-ik_0 z}}{\sqrt{2}}, \tag{6.6}$$

and $u_{\pm}(\mathbf{r})$ is the periodic part of the Bloch function evaluated at the conduction band minimum located at $\pm k_0 \hat{z}$. In a quantum dot fabricated in a strained silicon quantum well, $k_0 \approx 0.82 \times 2\pi/a$, with $a = 0.543$ nm the length of the Si cubic unit cell.[137] Depending on the magnitude of the valley splitting introduced by the sharp interfaces and the electric field in the z-direction, the lowest energy excited states can either be valley-like or orbital-like. For the case of an orbital-like excitation (large valley splitting), the wavefunction is

$$\psi_1^{Si,O}(\mathbf{r}) = \phi_{-}(\mathbf{r})\frac{F(z)(x+iy)}{\sqrt{\pi}L^2}e^{-\frac{1}{2L^2}(x^2+y^2)}. \tag{6.7}$$

When the valley splitting is smaller than the orbital splitting, both the ground state and first excited state have S-like transverse wavefunctions, but their z-direction wavefunctions are different valley states. The ground state wavefunction is still given by Eq. (6.5), but the first excited state is now

$$\psi_1^{Si,V}(\mathbf{r}) = \phi_{+}(\mathbf{r})\frac{F(z)}{\sqrt{\pi}L}e^{-\frac{1}{2L^2}(x^2+y^2)}. \tag{6.8}$$

The periodic parts of the Bloch functions, $u(\mathbf{r})$, have discrete Fourier spectra, with contributions occurring at reciprocal lattice vectors $\mathbf{G}$. Hence, when performing calculations with the full wavefunctions, as we do in this chapter, it is convenient to decompose $u(\mathbf{r})$ into the sum:[144, 139, 140]

$$u(\mathbf{r}) = \sum_{\mathbf{G}} \alpha(\mathbf{G})e^{i\mathbf{r}\cdot\mathbf{G}}, \tag{6.9}$$

where the expansion coefficients $\alpha(\mathbf{G})$ are independent of $\mathbf{r}$. For low-frequency dephasing channels such as acoustic phonons and charge noise only the $\mathbf{G} = \mathbf{0}$ mode contributes significantly.[145] For high-frequency processes such as optical phonon couplings, contributions with $\mathbf{G} \neq \mathbf{0}$ can also be important. We assume that the electron-optical phonon couplings are independent of $\mathbf{G}$. With this assumption, one can prove that the calculation of dephasing rates is independent of the form of the periodic part of the Bloch functions. Hence, for all instances we consider in this chapter, we may ignore the periodic part of the Bloch functions.

In a real system, disorder would cause the excited states to have mixed valley and orbital characteristics [9], for which pure orbital-like and pure valley-like first excited states represent limiting cases. Hence, it is important to consider both the pure valley and orbital excitations described above.

6.3 Dephasing via the electron-phonon interaction

We now consider the dephasing of two-electron states in a single quantum dot due to the electron-phonon interaction, following the techniques of Ref. [132]. In Sec. 6.3, we consider dephasing in GaAs due to deformation potential, longitudinal and transverse piezoelectric, and polar optical phonons. In Sec. 6.3, we turn to silicon, where we may have either valley or orbital excitations, and the relevant dephasing channels are through intravalley deformation potential and intervalley optical phonons.

The general form of the electron-phonon interaction is [145]

$$V_{ep}(\mathbf{r}) = \sum_{\mathbf{q},\mathbf{G},\lambda} M_\lambda(\mathbf{q}+\mathbf{G})\rho(\mathbf{q}+\mathbf{G})(a_{\mathbf{q},\lambda} + a^\dagger_{-\mathbf{q},\lambda}), \tag{6.10}$$

where each $\mathbf{G}$ is a reciprocal lattice vector, $\mathbf{q}$ is constrained to the first Brillouin zone, ρ is the electron density operator, $a_{\mathbf{q},\lambda}$ and $a^\dagger_{\mathbf{q},\lambda}$ annihilate and create, respectively, phonons with wave vector $\mathbf{q}$, and λ indexes the phonon mode. Since we will treat the the relevant modes separately, we will suppress this sum over phonon modes in the calculations that follow. The electron-phonon coupling, $M_{\mathbf{q}+\mathbf{G}}$, is defined by

$$M(\mathbf{q}+\mathbf{G}) = -V_{ei}(\mathbf{q}+\mathbf{G})\left[(\mathbf{q}+\mathbf{G})\cdot\ \boldsymbol{\xi}\right]\sqrt{\frac{\hbar}{2\rho_m\Omega\omega_{\mathbf{q}}}}, \tag{6.11}$$

where V_{ei} is the electron-ion potential, $\boldsymbol{\xi}$ is the phonon polarization vector, ρ_m is the crystal mass density per unit volume, Ω is the crystal volume, and $\omega_{\mathbf{q}}$ is the phonon frequency. Since the singlet and triplet have different charge distributions, they are dressed differently by the phonons. The phonons can themselves decohere, which in turn causes dephasing between the singlet and triplet states. Following Ref. [132], the singlet-triplet dephasing

rate due to the electron-phonon coupling is

$$\Gamma_{ST} = \frac{\Omega}{2\pi^3\hbar^2}\sum_{\mathbf{G}}\int d^3\mathbf{q}\frac{|M(\mathbf{q}+\mathbf{G})A(\mathbf{q}+\mathbf{G})|^2}{\omega_{\mathbf{q}}^2+(\gamma_{\mathbf{q}}/2)^2}\frac{\gamma_{\mathbf{q}}}{2}, \tag{6.12}$$

where $\gamma_{\mathbf{q}}$ is the phonon relaxation rate, and A is a Fourier component of the charge density difference between triplet and singlet states:

$$A(\mathbf{q}+\mathbf{G}) = \frac{1}{2}\left(\langle T|\,\rho(\mathbf{q}+\mathbf{G})\,|T\rangle - \langle S|\,\rho(\mathbf{q}+\mathbf{G})\,|S\rangle\right). \tag{6.13}$$

Using the approximate forms for the singlet and triplet states detailed in Eqs. (6.1) and (6.2), we have

$$A(\mathbf{q}+\mathbf{G}) = \frac{1}{2}\left(\langle 1|\,e^{i(\mathbf{q}+\mathbf{G})\cdot\mathbf{r}}\,|1\rangle - \langle 0|\,e^{i(\mathbf{q}+\mathbf{G})\cdot\mathbf{r}}\,|0\rangle\right), \tag{6.14}$$

where $|1\rangle$ is the single-particle first excited state and $|0\rangle$ is the single-particle ground state. In the following subsections, we evaluate Eq. (6.12) for the different types of phonons in both GaAs and Si.

Phonon-induced dephasing in GaAs

For the purely orbital excitations supported by GaAs, the ground state transverse wavefunction is an S-orbital, while the first excited state transverse wavefunction is a P-orbital, as given in Eqs. (6.3) and (6.4). The three types of phonon couplings that contribute to decoherence are: deformation potential, piezoelectric, and polar optical. These differ only in the form of the electron-phonon coupling M, so their calculations proceed similarly.

In all cases, we assume a Gaussian form for the wavefunction in the z-direction:

$$F(z) = \frac{1}{\pi^{1/4}\sqrt{d}}e^{-z^2/(2d^2)}, \tag{6.15}$$

where d is the confinement length along the growth axis, which is typically a few nanometers. Choosing this form for the wavefunction represents an approximation, but it captures the relevant physics and allows us to obtain analytic results. Using this approximation and Eqs. (6.3) and (6.4), we use Eq. (6.14) to obtain

$$\left|A^{GaAs}(\mathbf{q})\right|^2 = \frac{L^4\left(q_x^2+q_y^2\right)^2}{4}e^{-\left(\left(q_x^2+q_y^2\right)L^2+q_z^2d^2\right)/2}. \tag{6.16}$$

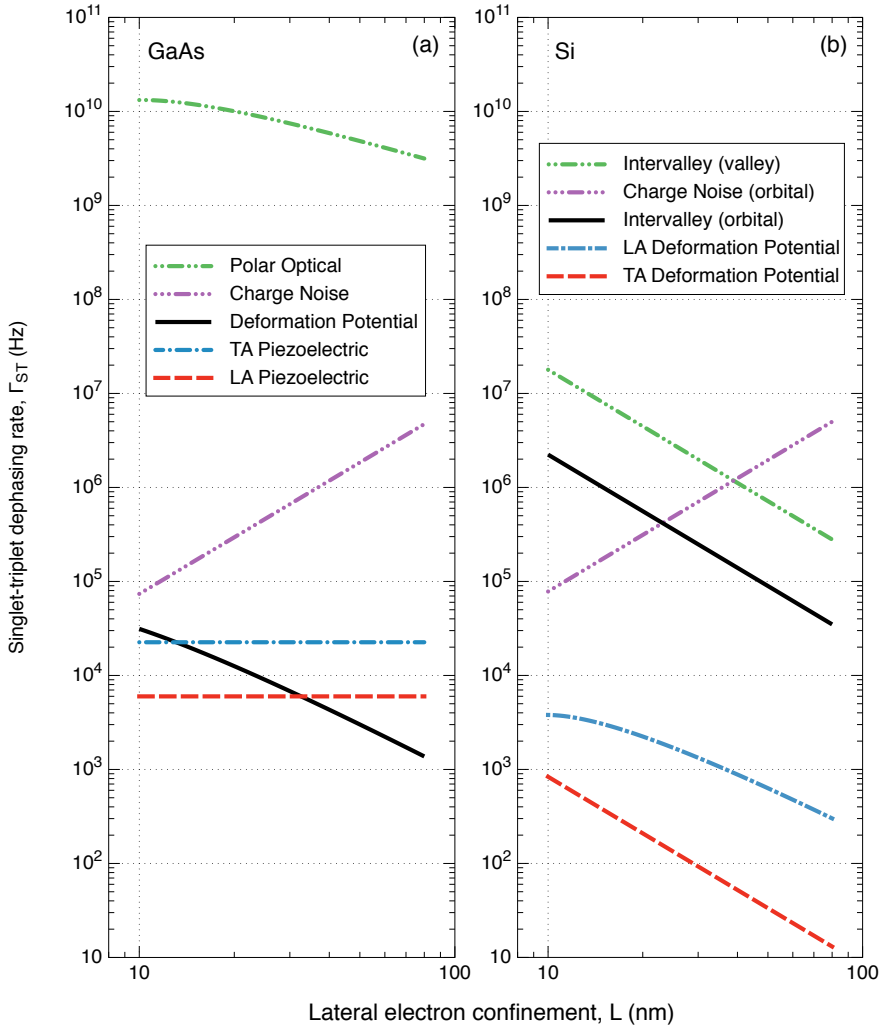

Figure 6.1: Calculated singlet-triplet dephasing rates of two electrons in a single dot via the phonon mechanisms considered in Sec. 6.3 and the charge noise mechanism considered in Sec. 6.4. (a): Plot of dephasing rates versus the lateral extent of the electron wavefunctions for the mechanisms pertinent for GaAs: polar optical phonons (Eq. (6.24)), deformation potential phonons (Eq. (6.18)), transverse piezoelectric phonons (Eq. (6.22)), and longitudinal piezoelectric phonons (Eq. (6.20)). (b): Plot of singlet triplet dephasing rates versus lateral wavefunction extent for different mechanisms in Si: intervalley phonons for valley excitations (Eq. (6.33)), and intervalley phonons (Eq. (6.32)), longitudinal acoustic phonons (Eq. (6.29)), and transverse acoustic phonons (Eq. (6.30)) for orbital excitations. The dephasing rates due to charge noise plotted for both materials systems are determined from Eq. (6.40), using the energy fluctuations for orbital excitations in a single dot (Eq. (6.36)), and assuming zero dipole moment.

Here, we have taken $\mathbf{G} = \mathbf{0}$, since $|A|^2$ goes to zero rapidly for $|\mathbf{q}| = q \gtrsim 1/d, 1/L$, both of which are much smaller than the size of the first Brillouin zone.

We first consider deformation potential phonons, for which the electron-phonon coupling M has the form [100, 132]

$$M^{DP}_{GaAs}(\mathbf{q}) = Dq \left(\frac{\hbar}{2\rho_m \Omega \omega_q} \right)^{1/2}, \tag{6.17}$$

where $D = 8.6$ eV is the deformation potential constant and $\rho_m = 5.33 \times 10^3$ kg/m^3 is the mass density of GaAs. The angular frequency $\omega_{\mathbf{q}}$ is given by the standard relationship for acoustic phonons: $\omega_{\mathbf{q}} = v_s q$, where $v_s = 5.2 \times 10^3$ m/s is the longitudinal speed of sound in GaAs, averaged over direction [146].

The last piece of information we need to compute the dephasing rate is the phonon relaxation rate γ_q. Eq. (6.16) implies that $|A|^2$ is strongly peaked, so it determines the $\mathbf{q}$-values that contribute to the integral in Eq. (6.12). In GaAs, $|A|^2$ goes to zero both as q goes to zero and when $q \gg 1/d, 1/L$. Hence, the low- and high-frequency behaviors of γ_q are not important. For sufficiently high frequencies at low temperature, it is expected that two frequency-dependent phonon attenuation channels will become relevant: anharmonic decay and isotope scattering [147]. However, the frequencies we consider here are low enough that these mechanisms are unimportant, and the dominant source of phonon relaxation is due to interface scattering [148].

To obtain an estimate for the phonon relaxation rate, we use experimental measurements of phonon attenuation due to interface scattering, which were performed at low-temperatures in Si [149]. To convert between the two, one uses $\gamma_q = 2\alpha_q v_s$ [150], where α_q is attenuation and $v_s = 8.49 \times 10^5$ cm/s is the speed of sound in Si along [100]. For LA phonons in Si, low-temperature measurements have shown that at low frequencies (up to 100 GHz), phonon attenuation is roughly frequency-independent, and is about 2.5 cm^{-1} along the [100] direction [149]. This translates to a low-frequency experimental limit of $\gamma_0^{LA} = 4.25$ MHz, which will serve to give us an estimate on the phonon relaxation rate. Since this mechanism is due to the geometry (i.e. the finite extent of the sample and pres-

ence of heterostructure interfaces) rather than the particular material properties of Si, we will also use the above relaxation time for acoustic phonons in GaAs.

By switching to polar-cylindrical coordinates, evaluation of the integral in Eq. (6.12) is straightforward. We set $\omega_{\mathbf{q}}^2 + (\gamma_q/2)^2 \approx \omega_{\mathbf{q}}^2$, which is valid because the frequencies that contribute to the integral satisfy $\omega_{\mathbf{q}} \gg \gamma_0$. Electrostatically defined quantum dots typically obey $L \gg d$, so we expand the integration result to first order in d/L, obtaining an expression for $\Gamma_{ST}^{GaAs,DP}$, the singlet-triplet decoherence rate in GaAs due to deformation potential electron-phonon coupling:

$$\Gamma_{ST}^{GaAs,DP} \approx \frac{D^2(4\ln(2L/d) - 3)\gamma_0^{LA}}{16\pi^2 L^2 v_s^3 \rho_m \hbar} \approx \frac{6.9}{L^2}\,\mathrm{MHz\,nm^2}. \tag{6.18}$$

Here, the dependence on L and d can be understood by power counting in Eq. (6.12). For the polar couplings we consider next, the L and d dependencies can be understood by examining the q_z integral in Eq. (6.12) over the range where $|q_z| \ll |q_x|, |q_y|$, followed by power counting.

We next consider piezoelectric coupling, which contribute in both longitudinal and transverse phonon modes. In this case, the electron-phonon coupling is [100, 132]

$$\begin{aligned} M_{GaAs}^{PE}(\mathbf{q}) = \frac{2iee_{14}}{q^2}\left(\frac{\hbar}{2\rho_m \Omega \omega_q}\right)^{1/2} \\ \times \left(q_x q_y \xi_z + q_y q_z \xi_z + q_z q_x \xi_y\right), \end{aligned} \tag{6.19}$$

where e is elementary charge and $e_{14} = 1.38 \times 10^9$ V/m is an elasticity tensor component. For longitudinal phonons, $\boldsymbol{\xi} = \mathbf{q}/q$. Integration of Eq. (6.12), expanded to lowest order in d/L, yields $\Gamma_{ST}^{GaAs,PE,LA}$, the singlet-triplet dephasing rate in GaAs due to piezoelectric coupling between electrons and longitudinal acoustic phonons:

$$\Gamma_{ST}^{GaAs,PE,LA} \approx \frac{3e^2 e_{14}^2 \gamma_0^{LA}}{140\pi^2 v_s^3 \rho_m \hbar} \approx 6.0\,\mathrm{kHz}. \tag{6.20}$$

In the limit when the media is considered isotropic and homogeneous, the two transverse phonon branches are degenerate, and we can choose any two orthogonal polarizations. One possible polarization is

$$\boldsymbol{\xi} = \left[\frac{q_y}{\sqrt{q_x^2 + q_y^2}}, -\frac{q_x}{\sqrt{q_x^2 + q_y^2}}, 0\right], \tag{6.21}$$

and any rotation of this vector about $\mathbf{q}$ is also a valid transverse polarization. We average over this plane before integrating over $\mathbf{q}$. This complicates the resulting integral, but it can still be carried out analytically, yielding $\Gamma_{ST}^{GaAs,PE,TA}$, the singlet-triplet dephasing rate in GaAs due to piezoelectric coupling between electrons and transverse acoustic phonons:

$$\Gamma_{ST}^{GaAs,PE,TA} \approx \frac{e^2 e_{14}^2 \gamma_0^{LA}}{70\pi^2 v_s^3 \rho_m \hbar} \approx 22\,\mathrm{kHz} \tag{6.22}$$

per transverse mode.

For polar optical phonons, the electron-phonon coupling is [100, 132]

$$M_{GaAs}^{PO}(\mathbf{q}) = \sqrt{\frac{2\pi e^2 \hbar\omega_0}{q^2\Omega}\left(\frac{1}{\epsilon_\infty} - \frac{1}{\epsilon_0}\right)}, \tag{6.23}$$

where $\epsilon_\infty = 10.89\epsilon_{vac}$ and $\epsilon_0 = 12.9\epsilon_{vac}$ are the high and low frequency limits of the GaAs dielectric function, and ϵ_{vac} is the vacuum permittivity. The frequencies of optical phonons are essentially $q-$independent, with $\hbar\omega_0 = 36.35$ meV. Since optical phonons are much higher in frequency than acoustic phonons, they also have much shorter lifetimes, with measurements indicating $\gamma_0^{LO} \approx 160$ GHz [151]. The integration proceeds similarly to the acoustic cases, and the resulting singlet-triplet dephasing rate $\Gamma_{ST}^{GaAs,PO}$ in GaAs due to polar optical electron-phonon coupling is, to first order in d/L:

$$\begin{aligned}\Gamma_{ST}^{GaAs,PO} &\approx \frac{e^2\left(\epsilon_0 - \epsilon_\infty\right)}{\epsilon_0\epsilon_\infty}\frac{(3\pi L - 16d)\gamma_0^{LO}}{16\sqrt{2\pi}L^2\hbar\omega_0} \\ &\approx \frac{240}{L}\,\mathrm{GHz\,nm}.\end{aligned} \tag{6.24}$$

In Fig. 6.1, we plot the four dephasing rates considered in this section. Typical values and scalings are listed in Table 6.1. Polar optical phonons are the largest contribution to dephasing, exceeding the others by at least five orders of magnitude. This is mainly due to the extremely fast decay of the high-frequency, optical phonons.

Phonon-induced dephasing in silicon

Unlike GaAs, Si quantum dots can support both valley and orbital excited electron states. The ground and first excited states in the case of an orbital excitation are given in Eqs. (6.5)

Table 6.1: Typical values for the dephasing rates of the phonon-induced channels discussed in Sec. 6.3, assuming a lateral electron confinement of $L = 40$ nm and a vertical confinement along the growth direction of $d = 3$ nm. The channels depend on material properties and symmetry: polar phonon couplings are absent in Si, transverse phonons do not couple electrons via the deformation potential in GaAs [132], at low temperatures and biases GaAs has only one band minimum that participates in conduction, and valley excitations in Si are not connected by low-frequency phonons. The scaling column describes the primary dependence of the dephasing rate on L, the lateral wavefunction extent and d, the vertical wavefunction extent. In the scalings, $(*)$ indicates a neglected logarithmic correction, while $(**)$ indicates that the result applies in the limit of $d/L \to 0$.

Coupling mechanism	Typical dephasing rate (Hz)			Scaling
	GaAs	Si: orb. excit.	Si: val. excit.	
LA phonons				
Deformation potential	4.3×10^3	8.8×10^2	-	L^{-2*}
Piezoelectric	6.0×10^3	-	-	-
TA phonons				
Deformation potential	-	5.2×10^1	-	L^{-2}
Piezoelectric	2.2×10^4	-	-	-
LO phonons				
Polar optical	5.9×10^9	-	-	L^{-1**}
Intervalley	-	1.4×10^5	1.1×10^6	$L^{-2}d^{-1}$

and (6.7). As we did for GaAs, we take the envelope in z to be Gaussian with width d. Then, defining $\mathbf{Q} = \mathbf{q} + \mathbf{G}$, we evaluate Eq. (6.14) for orbital excitations in Si (A_O^{Si}), obtaining

$$\left|A_O^{Si}(\mathbf{Q})\right|^2 = \frac{L^4(Q_x^2+Q_y^2)^2}{256} e^{-L^2(Q_x^2+Q_y^2)/2}\Big(4e^{-d^2Q_z^2/2} + e^{-d^2(2k_0+Q_z^2)/2} + e^{-d^2(2k_0-Q_z^2)/2}\Big), \tag{6.25}$$

where we used the fact that the three Gaussians are well-separated in Q_z to drop cross-terms. If we instead have excitations as given by Eqs. (6.5) and (6.8), we evaluate Eq. (6.14) for valley excited states in Si (A_V^{Si}), obtaining

$$\left|A_V^{Si}(\mathbf{Q})\right|^2 = \frac{1}{4} e^{-L^2(Q_x^2+Q_y^2)/2} \times \left(e^{-d^2(Q_z+2k_0)^2/2} + e^{-d^2(Q_z-2k_0)^2/2}\right). \tag{6.26}$$

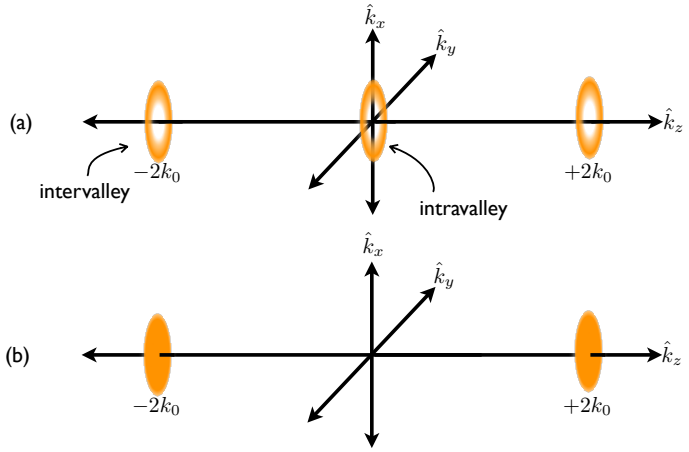

Figure 6.2: Cartoon of the absolute value of the Fourier transform of the difference between the triplet and singlet charge distributions, $|A|^2$ (Eq. (6.13)) in Si. Here, the shaded regions indicate the $\mathbf{k}-$values that contribute significantly to dephasing. Phonons that couple electrons in the same valley (intravalley processes) lie near the origin, while phonons that couple electrons in different valleys (intervalley processes) lie near $\mathbf{k} = \pm 2k_0\hat{k}_z$. (a): The contribution resulting from an orbital-like first excited state (Eq. (6.25)). (b): The contribution resulting from a valley-like first excited state (Eq. (6.26)).

The expressions for $|A_O^{Si}|^2$ and $|A_V^{Si}|^2$ in Eqs. (6.25) and (6.26) above select the types of phonons that contribute significantly to dephasing through the integral in Eq. (6.12). For orbital excitations, both phonons that couple electrons within the same valley and across valleys contribute, and $|A_O^{Si}|^2$ contains contributions from three toroids, each with peak radius $\sqrt{2}/L$, situated in the $k_x - k_y$ planes centered at $Q_z = 0$ and $Q_z = \pm 2k_0$. The phonons at the $Q_z = 0$ toroid correspond to intravalley processes, where $\mathbf{G} = \mathbf{0}$. The remaining two toroids at $Q_z = \pm 2k_0$ are intervalley processes, where $\mathbf{G} = \mp(4\pi/a)\hat{z}$. The regions of $\mathbf{k}-$space relevant to orbital excitations are shown in Fig. 6.2 (a). For valley excitations, $|A_V^{Si}|^2$ contains contributions from two ellipsoids centered at $\mathbf{Q} = (0, 0, \pm 2k_0)$. Since the valley-like first excited state has the same envelope function as the ground state, long wavelength phonons cannot contribute to the singlet-triplet dephasing. This is clearly illustrated by the vanishing of $|A_V^{Si}|^2$ at small k (or long wavelength). The regions of $\mathbf{k}-$space relevant to valley excitations are shown in Fig. 6.2 (b).

Now that we have identified the most important phonon wave vectors for the different

dephasing mechanisms, we discuss which electron-phonon coupling mechanisms are most relevant. Since Si is not polar, the deformation potential electron-acoustic phonon coupling is the main contribution near the zone center ($\mathbf{G} = 0$, $q \ll 2\pi/a$). This coupling connects electrons to both longitudinal acoustic phonons, with matrix element [100, 132]

$$|M_{LA}(\mathbf{q})|^2 = \Xi_d^2 \frac{\hbar q^2}{2\rho_m \Omega \omega_{\mathbf{q}}} \left(1 + \frac{\Xi_u}{\Xi_d} \frac{q_z^2}{q^2}\right)^2, \tag{6.27}$$

and to transverse acoustic phonons, with coupling [100, 132]

$$|M_{TA}(\mathbf{q})|^2 = \Xi_u^2 \frac{\hbar \xi_z^2 q_z^2}{2\rho_m \Omega \omega_{\mathbf{q}}}, \tag{6.28}$$

where $\Xi_d = 5.0$ eV and $\Xi_u = 8.77$ eV are silicon deformation potentials. As in Sec. 6.3 above, for these acoustic modes we take the phonon relaxation rate, believed to be due to interface scattering, to be $\gamma_0 = 4.25$ MHz [149]. The intravalley piece of the orbital excitation is found by integration of Eq. (6.12), which proceeds very similarly to the GaAs deformation potential case we considered in Sec. 6.3. For deformation potential coupling between electrons and longitudinal phonons in Si, the singlet-triplet dephasing rate $\Gamma_{ST}^{Si,LA}$, to first order in d/L, is:

$$\begin{aligned}\Gamma_{ST}^{Si,LA} &\approx \frac{\gamma_0}{192\pi^2 L^2 v_s^3 \rho_m \hbar} \Big[3(\Xi_d + \Xi_u)^2 \ln\left(16L^4/d^4\right) \\ &\quad - 9\Xi_d^2 - 42\Xi_d\Xi_u - 25\Xi_u^2\Big] \\ &\approx \frac{1.4}{L^2}\,\text{MHz}\,\text{nm}^2.\end{aligned} \tag{6.29}$$

As was the case for GaAs, the dependence on L and d can be understood by power counting in Eq. (6.12).

We perform the same averaging procedure as was done for the transverse phonons in the previous section and obtain $\Gamma_{ST}^{Si,TA}$, the singlet-triplet dephasing rate in Si due to deformation potential coupling between electrons and transverse acoustic phonons:

$$\Gamma_{ST}^{Si,TA} \approx \frac{\Xi_u^2 \gamma_0}{96\pi^2 L^2 v_s^3 \rho_m \hbar} \approx \frac{83}{L^2}\,\text{kHz}\,\text{nm}^2. \tag{6.30}$$

We next consider the intervalley contributions, which occur at $k_z = \pm 2k_0$, outside the first Brillouin zone. The reciprocal lattice vectors that contribute significantly to the relevant integrals are $\mathbf{G} = \pm(4\pi/a)\hat{k}_z$, which give $q_z \approx \mp 0.36(2\pi/a) = \mp 4.17 \times 10^9$ m^{-1}. The

phonons that are responsible for this transition in silicon are due to g-type Umklapp processes [100]. Although symmetry restricts these to be longitudinal optical phonons, experiments indicate that both transverse and longitudinal acoustic phonons participate through processes in which $M(\mathbf{q})$ is first-order in $\mathbf{q}$ [152, 100]. However, the acoustic phonons do not play a significant role here, both because their deformation potential coupling to the electrons is weaker [146] and they are much longer lived [147] than optical phonons.

The LO phonons in Si have a nearly constant energy $\hbar\omega_0 = 62$ meV [100]. The electron-phonon coupling arises from an optical deformation potential [100, 146]:

$$|M(\mathbf{Q})_{LO}|^2 = D_{if}^2 \frac{\hbar}{2\rho_m \Omega \omega_0}, \tag{6.31}$$

where the intervalley deformation potential $D_{if} = 11.0 \times 10^8$ eV/cm [146].

Finally, we estimate the relaxation rate γ_q for optical phonons in Si. As for optical phonons in GaAs, the short-wavelength longitudinal optical phonons that cause intervalley coupling have a much shorter lifetime than the long wavelength acoustic phonons that are responsible for intravalley coupling. The literature value we use for the relaxation rate is $\gamma_0^{LO} = 118$ GHz [153]. For the intervalley component of the orbital excitation, we get

$$\begin{aligned} \Gamma_{ST}^{Si,Orbital,LO} &= \frac{D_{if}^2 \gamma_0}{32\sqrt{2\pi^3} d L^2 \rho_m \hbar \omega_0^3} \\ &\approx \frac{670}{L^2 d}\,\mathrm{MHz\,nm^3}. \end{aligned} \tag{6.32}$$

Similarly, for the case of valley excitations we have

$$\begin{aligned} \Gamma_{ST}^{Si,Valley,LO} &= \frac{D_{if}^2 \gamma_0}{4\sqrt{2\pi^3} d L^2 \rho_m \hbar \omega_0^3} \\ &\approx \frac{5.3}{L^2 d}\,\mathrm{GHz\,nm^3}. \end{aligned} \tag{6.33}$$

Fig. 6.1 shows the dephasing rates for both GaAs and Si. Typical values and scalings with L and d are listed in Table 6.1. In Si, as in GaAs, most of the dephasing is due to the fast decay of optical phonons: in silicon these high-frequency phonons couple electrons across valleys.

So far, we have only considered pure valley and pure orbital excitations. However, for non-ideal interfaces such as those with atomic steps, valley-orbit mixing occurs [136, 9,

138]. Since both of the limiting cases exhibit strong dephasing due to intervalley phonons (with orbital excitations suppressed by a factor of 8 from valley excitations; see Eqs. (6.32) and (6.33)), we expect that valley-orbit mixing cannot be used to suppress substantially this dephasing.

6.4 Dephasing due to charge noise

We now consider the other expected major dephasing mechanism for our system: charge noise [129, 130, 131, 154]. This dephasing arises because remote charge fluctuations induce random variations of the energy splitting between singlet and triplet levels by coupling to their non-equivalent charge distributions via the Coulomb interaction. These variations in the energy splitting lead to the accumulation of a random phase between the singlet and triplet states. In turn, this introduces a phase difference between the logical qubit states. The dephasing mechanism and the estimated decay rates are essentially equivalent for GaAs and Si quantum dots, so we do not treat these two systems separately in this section.

Because the hybrid qubit has a potentially strong charge characteristic, it can couple to remote charge traps. We assume the simplest non-trivial charge fluctuation: a single, remote charge trap with two states (occupied and empty). To determine the dephasing rate, the first step is to compute the effect of the change in the state of the charge trap on the singlet-triplet energy splitting. We work to first order in perturbation theory, where we may calculate the small change in energy by using the unperturbed (spatial) wavefunctions. Using the formalism of Sec. 6.2, it is straightforward to show that the first-order estimate of the variation in energy splitting $\Delta V(\tau)$ is

$$\begin{aligned} \Delta V(\tau) &= \langle T| V(\tau) |T\rangle - \langle S| V(\tau) |S\rangle \\ &\approx \langle 1| V(\tau) |1\rangle - \langle 0| V(\tau) |0\rangle , \end{aligned} \tag{6.34}$$

where $|0\rangle$ is the ground state, $|1\rangle$ is the first excited state, and τ is time. Here, we assume that the energy fluctuations are much smaller than the singlet-triplet splitting, and hence also the confinement energy. At any instant in time, our perturbing charge trap might be

occupied or empty. If the charge trap at the position $\mathbf{r}$ is occupied, and hence perturbing the singlet-triplet energy splitting, we have

$$\Delta V = \int d^3r' \frac{e^2}{4\pi\epsilon_0} \frac{|\psi_1(\mathbf{r}')|^2 - |\psi_0(\mathbf{r}')|^2}{|\mathbf{r} - \mathbf{r}'|}, \tag{6.35}$$

where e is the elementary charge and ϵ_0 is the (low-frequency) dielectric constant of our material. We assume that the trap is distant and calculate ΔV in a multipole expansion.[155] For S- and P-like orbitals in a perfectly harmonic dot, the lowest-order, non-vanishing term is of quadrupole order:

$$\Delta V_{SP} \approx \frac{e^2 L^2 \left(1 + 3\cos(2\theta)\right)}{32\pi r^3 \epsilon_0 \epsilon_b}, \tag{6.36}$$

where L is the lateral electron confinement length and (r, θ, ϕ) is the location of the noise source in polar-spherical coordinates. Alternatively, for two valley states with identical envelope functions, we find that ΔV is exponentially suppressed by a factor of $e^{-d^2 k_0^2}$ to quadrupole order, where d is the z-envelope width and k_0 is the location of the valley minimum. To evaluate Eq. (6.36), we must estimate the typical distance r between the charge trap and the qubit. To do this, we consider a slightly different system comprised of a double dot charge qubit in GaAs, for which the energy splitting has been measured experimentally and found to be $\Delta V^{exp} \approx 1.6$ μeV [126]. Although this system differs from a two-electron dot, the statistics of the charge fluctuators should be similar. Evaluating Eq. (6.35) for the double-dot geometry, we find that the leading order term is a dipole contribution:

$$\Delta V_{DD} \approx \frac{e p_0 \cos\phi \sin\theta}{4\pi r^2 \epsilon_0 \epsilon_b}, \tag{6.37}$$

where p_0 is the dipole moment $e x_0$ associated with the dot separation x_0. Averaging over θ and ϕ with $x_0 \approx 300$ nm (the distance between the double dots considered in the experiment), we solve Eq. (6.37) to find $r \approx 2.9$ μm. Inserting this into Eq. (6.36), we obtain $\Delta V_{SP} \approx 2 \times 10^{-3}$ μeV for $L = 40$ nm in Si. Note that this value for ΔV_{SP} is likely an overestimate: if the dephasing is due to multiple charge traps (instead of the single trap we have assumed), ΔV_{SP} will be decreased. This is because matching to ΔV^{exp} while increasing the number of traps increases the average r. Since $\Delta V_{SP} \sim 1/r^3$ and

$\Delta V_{exp} \sim 1/r^2$, ΔV_{SP} decreases. Therefore, our estimate of the $S-T$ dephasing rate for an ideal orbital first excited state is an overestimate, and may decrease due to multiple charge traps.

Now that we know the magnitude of the energy fluctuations, we can calculate the dephasing time T_2. The off-diagonal elements of the density matrix decay as $e^{-\Delta\phi(\tau)}$, so the time T_2 is defined by $\Delta\phi(T_2) = 1$ [156]. Following Ref. [130], the time-dependent dephasing is given by

$$\Delta\phi(\tau) = \frac{1}{2\hbar^2}\int_{\omega_0}^{\infty} d\omega S(\omega)\left(\frac{\sin\omega\tau/2}{\omega/2}\right)^2, \tag{6.38}$$

where ω_0 is a low-frequency cutoff that is the inverse measurement time. Up to this point, we have only considered the coherent evolution of the phase due to charge fluctuations. However, true decoherence occurs due to the statistical nature of the fluctuators. This effect is captured in the spectral density $S(\omega)$ of the charge noise, through the definition

$$S(\omega) = \frac{1}{2\pi}\int_{-\infty}^{\infty} d\tau e^{i\omega\tau}\left\langle \Delta V(\tau)\Delta V(0)\right\rangle. \tag{6.39}$$

As noted in Ref. [130], by examining the form of Eqs. (6.38) and (6.39) we can deduce that T_2 for $1/f$ noise should scale as $1/\Delta V$. Thus, we can calibrate our T_2 to the experimental measurement via

$$T_2 \approx \left|\frac{\Delta V^{exp}}{\Delta V}\right| T_2^{exp}, \tag{6.40}$$

where ΔV^{exp} and T_2^{exp} are the experimental charge qubit measurements for the energy splitting fluctuation and the dephasing time. For the double-dot charge qubit experiment referenced above, $T_2^{exp} \approx 1$ ns, which leads to $T_2^{SP} \approx 0.8$ μs for our two electron dot with an orbital-like first excited state. Thus, the dephasing rate for orbital excitations due to charge noise in Si is $\Gamma_{ST}^{Charge} \approx 1.3$ MHz, which is on the same order as the phonon-induced dephasing in Si, and far slower than the dominant dephasing mechanism in GaAs. We plot this dephasing rate as a function of L alongside the phonon dephasing mechanisms in Fig. 6.1.

This long dephasing time is due to the fact that for a perfectly harmonic confinement potential, the dipole term of ΔV_{SP} vanishes. However, in realistic systems, potential an-

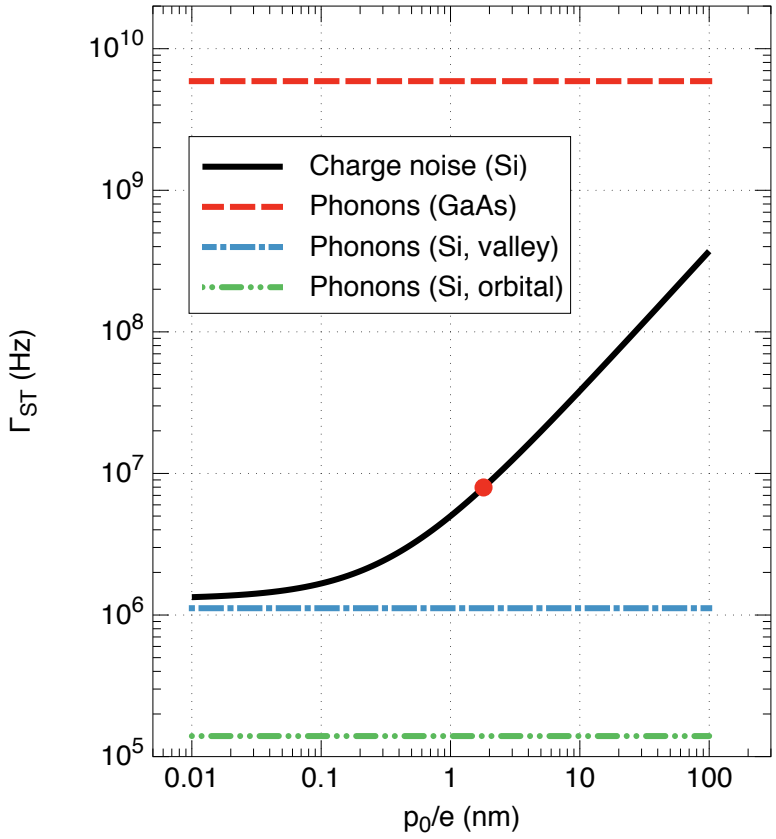

Figure 6.3: Singlet-triplet dephasing rate Γ_{ST} due to charge noise and electron-phonon coupling as a function of effective dipole moment p_0. In this plot, a constant quadrupole contribution of 1.3 MHz (Eq. (6.36)) is added to the dipole contribution, which is the estimated dephasing rate from charge noise for a dot with a purely harmonic confinement potential, for which $p_0/2$ is zero. Here, we have set the lateral electron confinement to be $L = 40$ nm, the vertical confinement to be $d = 3$ nm, and have assumed an orbital excited state. The charge noise curve for Si is estimated using a dielectric constant $\epsilon_0^{Si} = 11.7\epsilon_{vac}$. In a perfectly harmonic dot, $p_0 \approx 0$, but anharmonicity and disorder can introduce a dipole moment of $p_0 \lesssim eL$. In GaAs we expect phonon-mediated dephasing to be most important, but in Si quantum dots charge noise can easily dominate. The circle marker indicates the estimated dephasing due to charge noise at $p_0/e = 1.8$ nm, an estimated dipole moment for realistic devices.[157, 158]

harmonicity and interface roughness result in a non-vanishing dipole moment that can be more important than the quadrupole term in Eq. (6.36). If our confinement potential is severely anharmonic, we expect that we would have a dipole contribution similar to Eq. (6.37), but with a moment of $p_0 \lesssim eL$. Further, a disordered interface might also introduce

a dipole moment. As an example, simulations of the typical devices used in Refs. [157] and [158] find $p_0/e = 1.8$ nm.

Fig. 6.3 shows the dephasing rate due to charge noise as a function of dipole moment p_0, obtained by using Eqs. (6.37) and (6.40). The figure also shows the dominant dephasing rates from phonons calculated in Sec. 6.3 and listed in Table 6.1, which are essentially independent of dipole moment because there is substantial electron-phonon coupling even for perfectly harmonic confinement potentials. Within our approximations, we see that phonon-mediated dephasing is the most important mechanism in GaAs, but in Si charge noise can easily dominate.

6.5 Discussion

In this chapter, we addressed dephasing due to electron-phonon coupling and charge noise for two-electron states in a single quantum dot in both GaAs and Si. For the electron-phonon coupling, we found that in GaAs the main contribution to dephasing is due to polar coupling to optical phonons, and that the dephasing rate was of order gigahertz. In Si, phonon-mediated dephasing rates are much lower than in GaAs because there is no polar coupling to phonons, Intervalley processes are more important than intravalley processes, since phonons that couple valleys in silicon are extremely short-lived. The intervalley coupling to phonons leads a dephasing rate for silicon of order megahertz.

We found that charge noise for an orbital first excited state in a perfectly harmonic quantum dot with no disorder is strongly suppressed because the singlet-triplet energy splitting fluctuations produced by a remote perturbing potential in this case are of quadrupole order, while for a double-dot charge qubit they are of dipole order. As has been noted previously [159], pure valley states in Si are even more favorable, as they are largely immune to charge noise, in that both the dipole and quadrupole terms are suppressed by a factor of $e^{-d^2k_0^2}$. However, the introduction of either anharmonicity (for orbital excitations) or disorder (for valley excitations) leads to non-vanishing dipole moments up to the order of the lateral wavefunction extent. For either type of excited state in Si, this can become the dominant

dephasing mechanism. Our estimated dephasing rate due to charge noise, based on calculations in typical dots, is of order 10 MHz. This rate is fast enough to dominate the dephasing in silicon, but likely not in GaAs.

Our calculations suggest that two-electron, singlet-dot systems in Si have substantially better dephasing properties than those in GaAs. This is because the polar coupling for optical phonons, which mediates fast dephasing in GaAs, is absent in Si. Within Si, to reduce the dephasing in this system, the critical figure to optimize is the effective dipole moment of the charge density difference between the first excited state and the ground state. As indicated in Fig. 6.3, we estimate that unless this dipole moment is reduced below $p_0/e \sim 1$ nm, charge noise is expected to be the dominant dephasing mechanism. Below that threshold, the electron-phonon coupling (for valley excitations) and quadrupole-order charge noise (for orbital excitations) are expected to be the dominant dephasing mechanisms.

Finally, we note that throughout this chapter we focussed on conduction electron charge carriers, rather than holes. Since there have been recent advances in quantum dot structures that use holes [160, 118], a detailed study of two-hole dephasing would be useful, but is beyond the scope of the current work. Recent studies of hole relaxation in the context of low-temperature quantum dots [161] do not rely on the exact character of the spatial wavefunction, and so are not directly applicable to decoherence. We expect that the techniques we developed here can be readily extended to studies of holes. The major challenges in such a study would be determining the accurate hole spatial wavefunctions and deformation potentials, which would be affected around the valence band maximum by heavy hole-light hole mixing [162].

Chapter 7

Tunable singlet-triplet splitting in a few-electron Si/SiGe quantum dot

7.1 Introduction

Silicon quantum dots are candidate hosts for semiconductor spin qubits, both because of long spin relaxation and coherence times for electrons in Si, and because of potential synergy with classical microelectronics. Long spin relaxation times have been demonstrated in Si quantum dots and donors [163, 86, 164, 117], and measurements of ensembles of donor-bound spins by electron spin resonance have demonstrated T_2 coherence times up to 2s [165]. One of the key properties of Si quantum dot spin qubits is the ability to tune in real-time tunnel rates and couplings between neighboring dots by controlling electrostatic gate voltages [166, 167, 168]. Tunable, gate-defined Si quantum dots often are designed to sit at the interface between pure Si and a barrier of either SiGe [169, 170] or SiO_2 [171, 172, 173].

For initialization and readout of singlet-triplet spin qubits, an essential parameter is the energy difference E_{ST} between the singlet (with both electrons occupying the lowest energy single-particle state) and triplet states (built out of the lowest energy single-particle state

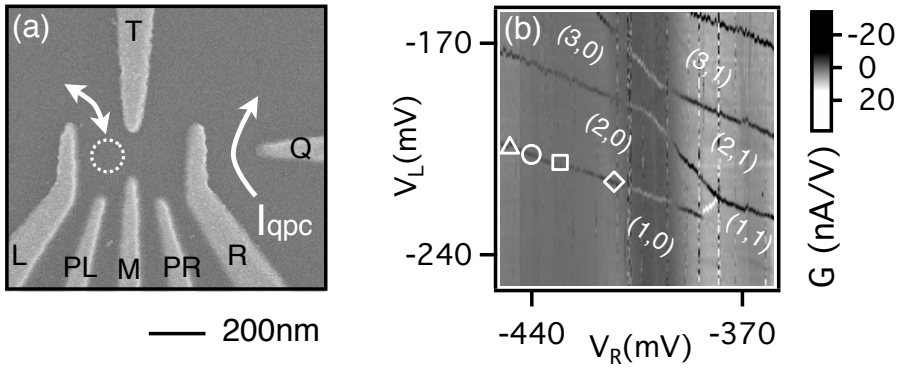

Figure 7.1: (a) Scanning electron micrograph of a double dot identical to the one used in the experiment. The transition measured here is between the left dot (white circle) and the left reservoir. (b) Stability diagram of the double dot with effective electron occupation numbers labeled. The white symbols between regions (1,0) and (2,0) correspond to the gate voltages for the data reported below in Fig. 3. The transition line at the bottom right is invisible, because tunneling between the reservoir and the right dot is slow in that regime.

and the first excited state) of two electrons in one dot [120, 121]. The energy $E_{\rm ST}$ is equal to the lowest single-particle excited state energy, less a correction arising from electron-electron interactions. In Si nanostructures, which have states arising from the two low-lying valleys in the Si conduction band, the sharpness and quality of the interface between Si and the SiGe or SiO_2 barrier material play an important role in determining this energy [136]. Experiments have shown that quantum-confined structures can have reasonably large valley splitting, ranging from 100 μeV to 1-2 meV [174, 175, 176]. The existence of large valley splitting in Si quantum dots has led to large $E_{\rm ST}$ and the observation of Pauli spin blockade [177, 178]. However, systematic control of the valley splitting or, more directly, $E_{\rm ST}$ has not been demonstrated in a Si quantum dot.

7.2 Experimental observation of the singlet-triplet splitting

In this chapter, we report a magnetospectroscopy study of a Si/SiGe double quantum dot with 2 and 0 valence electrons on the left and right dots, respectively. We use a pulsed-gate voltage technique to measure the evolution of the ground and low-lying excited states of the left dot as a function of an in-plane magnetic field B. We extract the magnetic

field B_{ST} at which the ground state changes from singlet to triplet, corresponding to the Zeeman energy equaling the singlet-triplet splitting E_{ST} for the $(2,0)$ charge configuration. We find that B_{ST} is tunable by lateral displacement of the quantum dot location, achieved by simultaneously tuning voltages applied to two gates on opposite sides of the dot. B_{ST} evolves systematically as a function of the gate voltages, and we measure a fractional change in B_{ST} of up to 19 %. Changes in gate voltages can alter both the position and shape of the electron wavefunctions in quantum dots [179, 180, 157]. Applying asymmetric changes to the voltages on either side of the quantum dot, as we do here, will change primarily the position of the quantum dot. We perform calculations showing that the fractional change in B_{ST} observed is consistent with valley-orbit mixing arising from a rough Si/SiGe interface, and that a change in position alone can account for observed changes in B_{ST}.

A double quantum dot, shown in Fig. 7.1(a), is fabricated as described in [86]. A quantum point contact (QPC), defined by gates R and Q, is used to perform charge sensing measurements. Gate L is connected to a pulse generator (Tektronix AFG3252), allowing the application of fast voltage pulses. The dc gate voltages are tuned so that the double dot is in the few-electron regime, as shown in Fig. 7.1(b). The change in background grayscale arises from changes in the QPC sensitivity caused by capacitive cross-talk in the device [181]. Measurements are performed in a dilution refrigerator at an electron temperature $T_{\mathrm{e}} = 143 \pm 10\,\mathrm{mK}$, determined as described in [86]. The electron occupation numbers are effective; we believe there are spin-zero closed shells of electrons in both the left and the right dots that do not participate in the physics discussed here.

To determine the 2-electron singlet-triplet splitting, we measure the gate voltage dependence of the transition from a single-electron spin-down state to the 2-electron ground state as a function of B. Figs. 7.2(a) and (b) show the transconductance $G = \partial I_{\mathrm{qpc}}/\partial V_{\mathrm{L}}$ as a function of B, measured with a lock-in amplifier using a 120 μV ac excitation voltage applied to gate L. The bright peak in the color plot corresponds to adding one electron to the left dot. The gate voltage of this transition first increases and then decreases as a function of B.

The electrochemical potential $\mu_{\rm N}$, and equivalently the gate voltage of transitions like those in Figs. 7.2(a) and (b), has a dependence on the in-plane magnetic field of the form $\partial\mu_{\rm N}/\partial B = g\mu_{\rm B}\Delta S_{\rm tot}(N)$ [182]. Here g is the Landé g-factor, $\mu_{\rm B}$ is the Bohr magneton, and $\Delta S_{\rm tot}(N)$ is the change in the z component of the total spin when the Nth electron is added to the dot. The electrochemical potential has a slope of $+g\mu_{\rm B}/2$ when a spin-up electron is added (magnetic moment anti-parallel to B), whereas the addition of a spin-down electron results in a slope of $-g\mu_{\rm B}/2$ (magnetic moment parallel to B). The positive slope in Fig. 7.2(a,b) at small B corresponds to the addition of a spin-up electron, forming a 2-electron singlet ground state. The arrows mark $B_{\rm ST}$, the magnetic field at which the slope changes; for $B > B_{\rm ST}$, the added electron is spin-down, and the ground state is the triplet $\rm T_-$. As indicated schematically in Fig. 7.2(c), the turning point of the slope corresponds to a magnetic field $B_{\rm ST}$ at which the Zeeman energy of the state $\rm T_-$ is equal to $E_{\rm ST}(B = 0)$. The value of $B_{\rm ST}$ is different in Figs. 7.2(a) and (b), indicating that $E_{\rm ST}$ is tunable with gate voltage.

Pulsed-gate spectroscopy methods [183, 158] allow us to confirm the state identification described above, while simultaneously mapping out the excited-state energy spectrum as a function of B. Square wave voltage pulses of peak-to-peak amplitude 3.6 mV and frequency 50 kHz are applied to gate L, and the time-averaged value of G is recorded, as shown in Fig. 7.2(d). Here, the bottom (top) line corresponds to the positive (negative) edge of the pulse bringing the 2-electron ground state into resonance with the Fermi level of the lead. Both of these lines therefore reproduce the shape of the line in Fig. 7.2(b).

The two middle lines in Fig. 7.2(d) meet at $B = 0$ and correspond to the triplet states $\rm T_-$ and $\rm T_0$, which are degenerate at this point, and as B increases, the lines split. The $\rm T_-$ line has a negative slope, corresponding to the addition of a spin-down electron, and this state becomes the ground state when $B = B_{\rm ST}$. The $\rm T_0$ line has a positive slope, corresponding to the addition of a spin-up electron. There is small chance of loading the $\rm T_+$ after unloading the singlet into a spin-up state; however, the process is weak and produces a line at the same location as the $\rm T_0$.

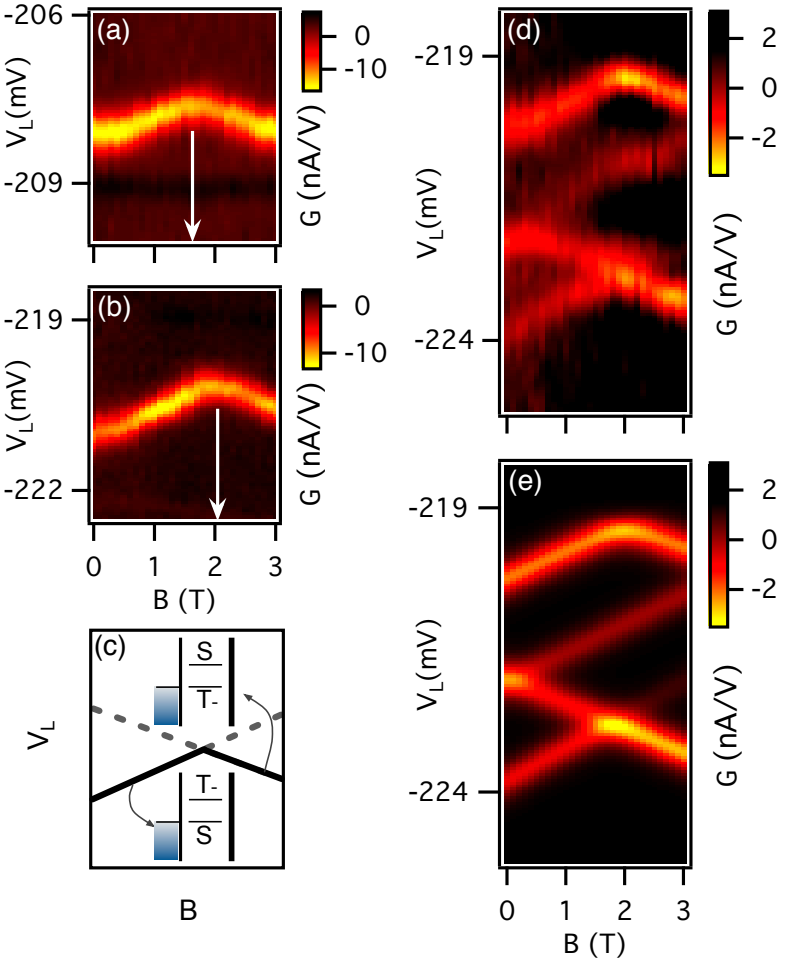

Figure 7.2: (a), (b) Ground state magnetospectroscopy for two different sets of gate voltages chosen so that the gate voltages for (b) favor a dot position farther to the right than those for (a) (see Fig. 7.3). The plots show the QPC conductance G. The arrows indicate the magnetic field B_{ST} at which the Zeeman shift for the T_- is equal to the zero-field E_{ST}. (c) Schematic diagram showing the transition as a function of B. (d) Excited state magnetospectroscopy using pulsed-gate voltages for the dot position corresponding to (b). (e) Simulated excited-state magnetospectroscopy for the data in panel (d).

7.3 Demonstration of tunable singlet-triplet splitting via dot translation

Fig. 7.2(e) shows a theoretical simulation of the experiment of Fig. 7.2(d), performed using a coupled rate equation model similar to that described in the supplemental material for

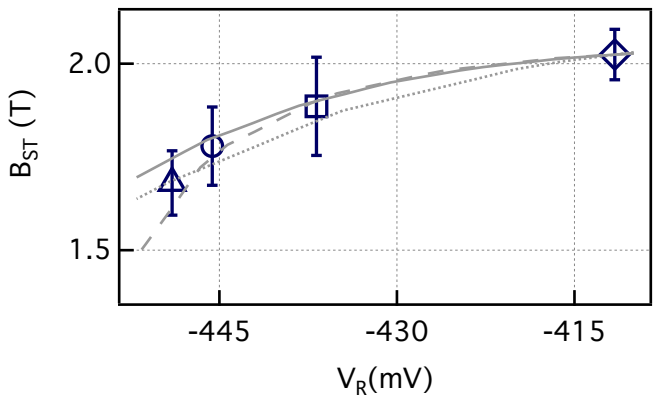

Figure 7.3: B_{ST}, the magnetic field at which the ground state shifts from S to T$_-$, for different sets of gate voltages V_{L} and V_{R}, corresponding to the symbols on the stability diagram in Fig. 1(b). Error bars are determined by the uncertainty in linear fits to lines like those in Figs. 2(a) and (b). The three gray lines show fits to three different sets of microscopic parameters that can be used to fit the experimental results.

Ref. [86]. The model includes thermal broadening but neglects energy-dependent tunneling. The S, T$_0$, and T$_-$ loading and unloading rates are determined by fitting the simulation to the data in Fig. 7.2(d). We find the loading rates $\Gamma_S^L = 45.1$ kHz, $\Gamma_{T_-}^L = 216$ kHz, and $\Gamma_{T_0}^L = 377$ kHz, and the unloading rates $\Gamma_S^U = 164$ kHz, $\Gamma_{T_-}^U = 354$ kHz, and $\Gamma_{T_0}^U = 183$ kHz.

Using the method illustrated in Figs. 7.2(a) and (b), we measure the transition field B_{ST} at four different gate voltage configurations, corresponding to the symbols shown in Fig. 7.1(b). Along this line in the stability diagram, changes in V_{L} and V_{R} tend to shift the dot physically from left to right as V_{R} (V_{L}) is made more positive (negative). As shown in Fig. 7.3, we observe a systematic increase in B_{ST} as we move from left to right in the stability diagram. Over this range, B_{ST} increases from 1.68 ± 0.09 T to 2.02 ± 0.07 T, a total increase of ~ 19 %.

The singlet-triplet splitting can be expressed as $E_{\mathrm{ST}} = E_1 - E_0 + C_{01} - C_{00} + K_{\mathrm{ST}}$, where E_0 and E_1 denote the ground and first excited-state energies, C_{01} and C_{00} are the Coulomb interaction energies of the two electrons in the singlet and triplet states, and K_{ST} is the exchange energy [184]. A simple shift of the dot position is expected to have little effect

on the last three terms, which correspond to interactions between the electrons. Similarly, the shape of the wavefunction envelope should change very little as a function of the dot displacement. The variation in B_{ST} is not caused by a change in g-factor as a function of gate voltage, because we calculate that only 0.6% of the electron density resides in the SiGe barrier, and the g-factor changes $\sim 2\%$ between Si and $Si_{0.7}Ge_{0.3}$, the concentration used in our heterostrucutre [185]. Thus, it is important to check whether microscopic features of the quantum device can account for the changes in E_{ST} that we observe.

The single-particle spacing $\Delta E = E_1 - E_0$ has a contribution arising from the difference in valley components in the two lowest lying orbital states. The quantum well interface will have atomic steps and other sharp changes in potential that vary as a function of lateral position, and these variations can modify the coupling of the two z-valleys, contributing to a position dependence of the energy difference ΔE [138, 186].

To test whether a small atomic-scale variation can account for the magnitude of the observed variations in B_{ST}, we perform tight-binding calculations of the single particle energy levels of an electron confined near a single atomic step. The calculations use a two-dimensional tight-binding Hamiltonian similar to Refs. [133, 187], including a parabolic lateral confinement potential. The fitting procedure varies the position of the atomic step, the confinement length scale, and the vertical electric field, enabling a calculation of the variation in ΔE as a function of gate voltage. To compare with the measured B_{ST}, we also fit the sum of the Coulomb and exchange energies ($C_{01} - C_{00} + K_{\mathrm{ST}}$), and the results are plotted in Fig. 7.3. The fitting is underconstrained, as there are many physical ways to produce similar valley splitting. To indicate the types of variations possible, three results are plotted in Fig. 7.3 as the solid, dashed, and dotted lines, and all three calculations can reproduce the magnitude of the observed change in B_{ST}. The lowest excited-state can be classified as "orbital-like" when the calculated wavefunction contains a lateral node or "valley-like" when it does not, and both cases occur. For valley-like excitations, lateral translation of the dot with respect to a step results in a tunable valley splitting. For orbital-like excitations, strong valley-orbit coupling enables a tunable orbital energy splitting (see

chapter 8). Thus, atomic-scale structure of the quantum well interface is sufficient to produce valley-orbit mixing large enough to account for the experimental observations, even under the assumption that the dot shape is unchanged as a function of gate voltage.

Chapter 8

Disorder-induced valley-orbit hybrid states in Si quantum dots

8.1 Introduction

Isolated electrons in semiconductor systems are a promising candidate for scalable quantum computation because they exhibit excellent control and decoherence properties, while being able to leverage the mature semiconductor industry to scale up [184]. Much recent progress has led to demonstrations of both spin- and charge-based qubits in GaAs [126, 121, 115, 188] and Si [117, 111, 189]. While Si has better spin decoherence properties than GaAs [190], silicon's nontrivial conduction band valley structure is a complication [191].

The presence of the valley degree of freedom in Si quantum dot devices can lead to difficulty in isolating a two-state system to use as a qubit, because valley splitting energies can be the same order as both Zeeman splittings and orbital energy spacings [191, 174, 135]. On the other hand, it has been proposed to harness this valley degree of freedom to define noise-resistant qubits [191, 192, 159]. Previous studies of valley states in Si have mainly focused on an idealized picture of the valley and orbital physics in which the system is taken to be disorder-free, and hence the valley and orbital degrees of freedom are good quantum numbers for the system [137, 193].

It has been recognized that structural disorder, such as atomic steps at the heterostructure interface, alloy disorder, or other types of correlated randomness, can introduce new effects such as intervalley tunneling [194, 186]. Furthermore, recent experimental evidence for disorder-influenced valley-orbit physics has been found in both MOS [195, 196] and Si/SiGe systems [9, 189]. Studying disorder in silicon is especially challenging, since the conduction band valley states couple atomic-scale disorder to the micron-scale electron confinement that is typical of quantum dots. To analyze this problem, researchers have used computationally intensive numerical techniques such atomistic tight binding [134, 197], or analytical approaches that assume the effective mass theory holds with only minor corrections necessary [136, 137, 186].

In this chapter, we develop a systematic disorder-expansion technique that successfully reproduces the results of atomistic simulations, while retaining the appealing physical intuition and computational efficiency of effective mass theories. Using this technique, in addition to the valley mixing matrix elements noticed previously, we identify matrix elements that correspond to valley-orbit hybridization, which were previously studied in an approximation using the two lowest energy $z-$states [138]. We also show that the presence of these matrix elements leads to the emergence of effects not observed in previous analytical treatments. In particular, we show that disorder leads to finite dipole matrix elements between valley states, and quantitative corrections to intervalley tunneling. Both effects are detrimental to quantum information stored in valley states.

8.2 Disorder-expansion effective mass theory

In Si quantum dots confined to a quantum well in the absence of disorder, one can show through tight-binding or effective mass theories that the energy eigenstates $\Psi_{i,\pm}(\mathbf{r})$ form symmetric and antisymmetric valley doublets [137]:

$$\Psi_{i,\pm}(\mathbf{r}) = \frac{1}{\sqrt{2}}\left[u_{-k_0}(\mathbf{r})e^{-ik_0 z} \pm u_{k_0}(\mathbf{r})e^{ik_0 z}\right] h_i(\mathbf{r}), \tag{8.1}$$

where $\mathbf{r}$ is the spatial position, h_i is the electronic envelope function for the i^{th} orbital, and $u_{\pm k_0}$ is the periodic part of the Bloch function located at the conduction band minima $\mathbf{k} = \pm k_0 \hat{z}$,. Here, $k_0 = 0.82 \cdot 2\pi/a$ is the position of the valley minimum, and $a = 0.543$ nm is the cubic lattice spacing in Si.

To calculate the effects of disorder on valley states in Si accurately, researchers have previously relied on atomistic tight-binding techniques [134, 198, 199, 197] which are numerical and extremely expensive computationally. Here, we introduce a new semi-analytical technique based on a systematic expansion in the matrix elements of disorder. This technique allows us to understand analytically and compute accurately the effects of interface disorder much faster than was previously possible.

We consider an unperturbed problem consisting of a lateral, two-dimensional confinement potential $V(x, y)$ that describes a quantum dot or other device, and a one-dimensional, vertical confinement potential $U(z)$ that includes the sharp interfaces, the quantum well barriers, and other slowly-varying components such as an applied electric field. Since this problem is separable, the resulting wavefunction is written as $\Psi_{i,j}(\mathbf{r}) = F_i(x, y)\psi_j(z)$, where i is the x-y orbital index and j is the subband index [137].

We solve the x-y problem using the effective mass equation,

$$\begin{aligned} &\left[-\frac{\hbar^2}{2m_t}\left(\partial_x^2 + \partial_y^2\right) + V(x, y)\right] F_i(x, y) \\ &\qquad \equiv H^0_{xy} F_i(x, y) = \epsilon_i F_i(x, y) \ , \end{aligned} \tag{8.2}$$

where $m_t = 0.19\, m_0$ is the transverse effective mass in Si, with m_0 the bare electron mass. The z problem is described similarly, with an unperturbed Hamiltonian H^0_z. However, the solution method is different because H^0_z includes sharp interface potentials that couple different valley states. There are a number of well-established techniques to solve this 1D problem, including augmented effective mass treatments [137] and tight-binding techniques [134], which yield solutions of the form noted in Eq. (8.1). The results shown below are obtained using the 1D tight-binding treatment.

We now introduce disorder through the perturbation potential $D(\mathbf{r})$. For the "bump" geometry shown in Fig. 8.1, $D(\mathbf{r})$ is zero everywhere except for the small black region, where

it has the same height as the barrier potential. We write the full Schrödinger equation, including the disorder potential, as

$$\left[H_{xy}^0 + H_z^0 + D(\mathbf{r})\right] \phi_l(\mathbf{r}) = E_l \phi_l(\mathbf{r}). \tag{8.3}$$

We solve this equation by expanding in terms of the unpertubed basis set:

$$\phi_l(\mathbf{r}) = \sum_{j,k=1}^{\infty} \alpha_{jk}^l F_j(x,y)\psi_k(z), \tag{8.4}$$

where α_{jk}^l are the expansion coefficients. The problem then reduces to a matrix eigenvalue problem for the coefficients α_{jk}^l and the energies E_l.

The expansion described in Eqs. (8.3) and (8.4) must be truncated to find a numerical solution. However, the method is guaranteed to succeed if a sufficiently large basis set is used. Since matrix elements of the disorder potential $D(\mathbf{r})$ can be large, we may need many basis functions to obtain quantitative accuracy. In the problems studied below, accurate, converged solutions can be obtained reasonably quickly by using tens of the $\psi_k(z)$ basis functions and tens of the $F_j(x,y)$ basis functions, leading to a dense effective Hamiltonian matrix with dimensions $N \times N$, where $N \sim$100-500.

8.3 Application to quantum dot systems

We now apply this disorder-expansion technique to calculate the eigenstates of a single quantum dot, and the tunneling coefficients for a double quantum dot, in the presence of a disordered interface. Many previous analytic treatments of disordered interfaces considered only the effects of valley mixing (VM) between the two low-lying valley states. Here, the disorder-expansion method allows us to treat both VM and valley-orbit hybridization (VOH), which describes the mixing of orbital and valley degrees of freedom, and is observed only when the basis includes more than one orbital degree of freedom [138]. When VOH is significant, the electric dipole moment between the lowest two states,

$$\mathbf{p} = e \int d^3\mathbf{r} \left(|\phi_1(\mathbf{r})|^2 - |\phi_0(\mathbf{r})|^2 \right) \mathbf{r}, \tag{8.5}$$

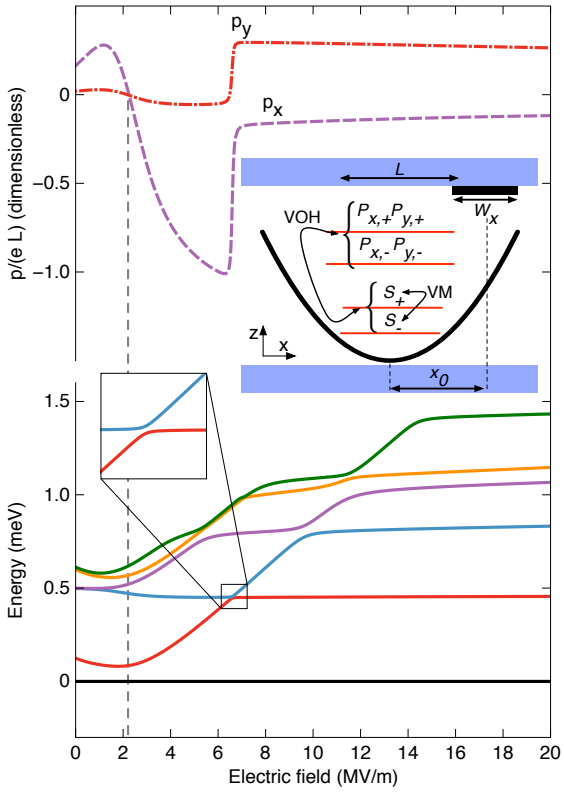

Figure 8.1: Calculation of low-lying energy eigenstates and electric dipole moments for a 3D quantum dot in a quantum well with interface disorder, demonstrating that valley-orbit mixing induces a substantial dipole moment. The simulation geometry (inset) has a quantum well thickness of 10 nm and a barrier height of 150 meV. The parabolic quantum dot is circular, with a diameter of $L = 28.3$ nm. Disorder is introduced as a rectangularly shaped "bump" (black region) in the quantum well barrier, with an x-width of $W_x = 2L$, a y-width of $W_y = 4L$, a height of a single atom, and a center position at $(x_0, y_0) = (-0.7L, -0.7L)$. The top two curves show the components of the dipole moment $\mathbf{p}$, defined in Eq. (8.5), along the $\hat{x}$ (dashed) and $\hat{y}$ (dash-dotted) directions, as a function of electric field applied along $\hat{z}$. The lower set of solid curves show the lowest six energy levels in the quantum dot, measured relative to the ground state. At low fields, these form two manifolds: a lower, S-like doublet and an upper P-like quadruplet. Disorder introduces two distinct effects: valley mixing (VM) between states in the same valley doublet, and valley-orbit hybridization (VOH) between states in different valley doublets. The dipole moment is typically substantial, but it is suppressed near the VM-induced anticrossing indicated by the vertical dashed line. A second anticrossing occurs at a higher field, where the first excited state changes from valley-like to orbital-like, and is accompanied by a large change in the dipole moment.

where $-e$ is the electron charge, can also be significant. In constrast, Eq. (8.5) yields $\mathbf{p} = 0$ when ϕ_0 and ϕ_1 represent pure pure orbital states, and is on the scale of the atomic lattice

spacing when ϕ_0 and ϕ_1 are pure pure valley states. For qubit applications, a finite dipole moment makes the system susceptible to charge noise [126, 130, 7].

We consider the specific quantum dot geometry shown in Fig. 8.1. For simplicity, we choose a 2D parabolic confinement potential for the quantum dot with an energy level spacing of $\hbar\omega = 0.5$ meV, corresponding to a characteristic dot size of $L = \sqrt{\hbar/(m_t\omega)} =$ 28.3 nm. We choose the lateral dimensions of the bump perturbation to be of order of L, as consistent with recent stuctural characterization of Si/SiGe heterostructures [200]; specifically, we use $W_x = 2L$ and $W_y = 4L$. The height of the bump is taken to be a single atom. The quantum well width is 10 nm, with a barrier height of 150 meV. We compute the z-basis functions within the 1D tight-binding method described in Ref. [134]. The full 3D calculations are carried out using the disorder-expansion framework described above, with a basis of size $5(x) \times 5(y) \times 30(z)$. The results are of good accuracy, as described in Appendix E.1.

The results of our single-dot calculations are shown in Fig. 8.1 as a function of the perpendicular electric field. The curves at the top of the plot p_x and p_y, the $\hat{x}$ and $\hat{y}$ components of the electric dipole moment. For the device specifications used here, the dipole moment is typically comparable to eL. Its non-monotonic dependence on perpendicular electric field can be understood by examining the energies of the lowest six energy eigenstates of the quantum dot, shown in the lower portion of Fig. 8.1. At low fields, the lowest set of six energy eigenstates splits into two orbital manifolds. Each of these manifolds is further split by a small valley splitting of order 0.1 meV. As the field is increased, the lowest two states undergo successive transitions, corresponding to level anticrossings: a VM transition at about 2×10^6 V/m, and a VOH transition at about 7×10^6 V/m. The VM anticrossing is caused by a competition beween two different confinement potentials: the quantum dot and the effective confinement caused by disorder. The dipole moments are strongly suppressed at the VM anticrossing, as shown in Fig. 8.1, although the magnitude of $\mathbf{p}$ is never zero. We note that in the limit of large orbital energy spacing $\hbar\omega$, the dipole moment scales approximately as $1/(\hbar\omega)$, as consistent with lowest order perturbation theory. Therefore,

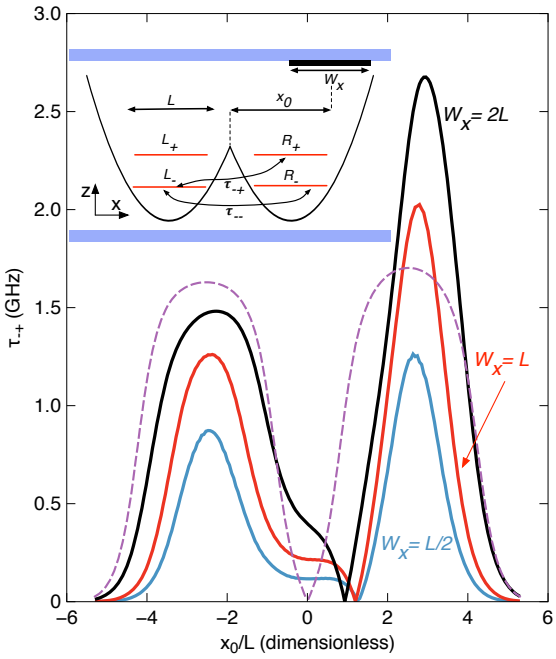

Figure 8.2: The intervalley tunnel rate $\tau_{-+} = \langle L_- | H | R_+ \rangle$ between two sides of a double quantum dot in the presence of a "bump" at the quantum well interface, as a function of the bump position x_0. Here, the height of the bump is one atom, L_- refers to the lowest left-localized state, and R_+ refers to the first excited right-localized state. A schematic of the calculation geometry is shown in the inset. In the absence of disorder, the $\pm$ indices refer to unperturbed valley states. Results are shown for bumps with widths $W_x = L/2$, L, and $2L$ in the x-direction, and infinite widths in the y-direction. The solid curves are computed using the disorder-expansion framework described in the main text, with a basis of size $50(x) \times 1(y) \times 10(z)$, while the dashed line is an alternative result for $W = 2L$, with a basis of size $1(x) \times 1(y) \times 2(z)$, which does not admit VOH effects. For the calculations shown here, the dimensions of the individual dots are the same as Fig. 8.1, and we assume an electric field of 2×10^5 V/m applied perpendicular to the quantum well. The intervalley tunneling rate is substantial over a wide range of bump positions and widths.

two methods are available to help suppress the unwanted dipole moment: using smaller dots and working at fields corresponding to the VM anticrossing.

We now study the impact of VOH on interdot tunneling. As noted in Refs. [186, 138], structural disorder induces VM, so the z-component of the wavefunction is no longer well described by its unperturbed eigenstate. Since disorder varies spatially, the z-composition of the wavefunction will be different from dot to dot. This leads to intervalley tunneling, meaning that an electron can change valley indices when tunneling between two dots [194]. When quantum information is stored in the valley indices, intervalley tunneling constitutes

a loss of information. Here, we go beyond previous work [186] by considering tunneling between the two sides of a double quantum dot, and by including VOH effects using the disorder-expansion technique described above.

We again adopt a simple model for interface disorder: a rectangular bump at the quantum well interface, as shown in the inset of Fig. 8.2. In this calculation, we take the bump width to be infinite in the y direction, but variable in the x direction. As anticipated in Ref. [186], the intra- and inter-valley tunnel rates are comparable when the bump width, analogous to the disorder correlation length, is comparable to the lateral widths of the quantum dot. We consider two quantum dots in a biquadratic potential. The individual dot potentials have circular symmetry, with a diameter of $L = 28.3$ nm, and an interdot separation of $d = 144$ nm. We define the states $L_\pm$ and $R_\pm$ to be the left and right-localized states, obtained from the lowest two eigenstates of the left and right individual confinement potentials. All four states $L_\pm$ and $R_\pm$ are computed within the disorder-expansion framework using a basis set of size $50(x) \times 1(y) \times 10(z)$. (See Appendix E.1 for convergence details.)

To calculate the tunneling, we compute the matrix element of the total, double dot Hamiltonian between left- and right-localized states. Technical details for efficiently computing this matrix element can be found in Appendix E.2. We run our calculation at a low applied electric field, $F = 2 \times 10^5$ V/m, so that in the absence of disorder, the lowest two states in each dot form a valley doublet. This is the regime where the valley index is most likely a good quantum number for quantum computing. With no disorder, the x and z-directions are separable, so the intervalley tunneling term is zero:

$$\tau_{-+} = \langle L_- | \, H \, | R_+ \rangle = 0 \; . \tag{8.6}$$

However, the introduction of an atomic bump leads to significant intervalley tunneling, as shown in Fig. 8.2. In the calculation, the dot geometry is chosen such that the interdot, intravalley tunnel rate in the absence of disorder is 2 GHz, which is a typical value observed in experiments [189]. Over a wide range of bump positions, we confirm that the intervalley tunnel rate is comparable to the intravalley tunnel rate. We find that the intervalley tunnel

rate is largest when the bump in the interface is centered over one of the quantum dots. The dashed line in Fig. 8.2 corresponds to only using one x-basis function, one y-basis function, and two z-basis functions, corresponding to the simple model considered in previous studies [186], where the VOH coupling is effectively turned "off." Although the approximate solution is qualitatively similar to the accurate solution, it is not quantitatively accurate.

Our theoretical results for intervalley tunneling are in reasonable agreement with recent experiments in a double quantum dot, where tunnel rates were measured between a $(2,1)$ electron occupation and two different $(1,2)$ occupations, corresponding to the ground and lowest excited states [189]. The small energy splitting between the $(1,2)$ configurations (~ 45 μeV) is indicative a large valley component in the excited state. (Orbital excitations are typically larger, in the range 0.1-1 meV [158].) The fact that comparable tunnel rates were observed for both $(1,2)$ states (2.7 GHz vs. 3.5 GHz) indicates a strong intervalley matrix element.

Finally, it is interesting to compare the numerical complexity of our scheme to that of a tight binding method. For the double dot considered here, we achieve good accuracy with a basis of size $N = 500$. The computational bottleneck in this procedure is diagonalizing the resulting $N \times N$ dense matrix, which takes a few seconds on a personal computer. In contrast, the number of atoms involved in a 3D tight binding calculation (excluding atoms outside the quantum well) corresponds to including several hundred million atomic sites, which requires run-times of many hours on modern supercomputers [199].

8.4 Discussion

We have introduced a new disorder-expansion effective mass technique for studying disordered silicon systems. This framework provides results consistent with computationally intensive tight-binding calculations [197], while retaining the calculational simplicity and intuitive appeal of the effective mass approach. This approach reveals additional valley-orbit hybridization effects, which are responsible for a non-vanishing dipole moment between valley states, as well as intervalley tunneling.

Both valley mixing and valley-orbit hybridization are problematic for storing quantum information in valley states, since in the presence of disorder they no longer afford protection against charge noise, and do not have consistent quantum numbers between dots. We find that the dipole moment can be mitigated by operating the device at a specific applied electric field, and also by making the dot smaller.

Chapter 9

Conclusion

In this thesis, we have considered several aspects of quantum computation, exploring both software and hardware. The first three chapters discuss recent progress in quantum algorithms. In chapter 2, we develop a framework for calculating the evolution operator of multi-particle non-interacting walks, and use it to prove that two-particle non-interacting walks cannot distinguish strongly regular graphs. We then perform high-throughput computing calculations to present extensive numerical evidence that introducing interactions allows for universal strongly-regular graph distinguishing. Chapter 3 applies the framework we developed in non-interacting walks with more particles, demonstrating that three- and four-particle walks can distinguish some strongly regular graphs. In chapter 4, we investigate a recently proposed quantum adiabatic algorithm for Google PageRank, showing numerically that it appears to scale as a power law for realistic WWW graphs.

In the final four chapters, we discuss issues that occur in the physical implementation of a quantum computer. Chapter 5 discusses the concept of using a cold two dimensional electron gas as a heat sink for a nearby hot electronic system. The heat transfer problem is analogous to the Coulomb drag effect, but for energy rather than momentum. Next, in chapter 6 we calculate the dephasing that occurs in a quantum dot with two electrons, a problem of critical importance for certain qubit architectures. Chapter 7 shows that translation of quantum dots can alter the eigenstate energies, which is indicative of structural interface

disorder. Finally, in chapter 8 we continue to discuss the effects of structural disorder on quantum dots. We develop a new theoretical framework for calculating the effects of disorder, which outperforms previous techniques in both computational efficiency and clarity.

Appendix A

Supplemental information for Chapter 2

A.1 Checking the two-particle matrix elements

In this appendix we demonstrate that eqs. 2.16 and 2.24 are equivalent to Eq. 2.7 for both Bosons and Fermions. To show that the Boson matrix elements as given in Eq. 2.16 are correct, we evaluate the three types of basis elements we have in eq. 2.16. When $i \neq j$ and $k \neq l$, Eq. 2.16 yields

$$\begin{aligned}
{}_B\langle ij|\mathbf{H}_{2B}\,|kl\rangle_B &= \left(\frac{\langle ij|' + \langle ji|'}{\sqrt{2}}\right)\Big[-\frac{1}{2}\left(\mathbf{I}+\mathbf{S}\right)\left(\mathbf{A}\oplus\mathbf{A}\right) \\
&+ U\mathbf{R}\Big]\left(\frac{|kl\rangle' + |lk\rangle'}{\sqrt{2}}\right) \\
&= -\left(\frac{\langle ij|' + \langle ji|'}{\sqrt{2}}\right)\left(\mathbf{A}\oplus\mathbf{A}\right) \\
&\cdot \left(\frac{|kl\rangle' + |lk\rangle'}{\sqrt{2}}\right) \\
&= -A_{ik}\delta_{jl} - A_{jl}\delta_{ik} - A_{il}\delta_{jk} - A_{jk}\delta_{il}.
\end{aligned} \tag{A.1}$$

When $i \neq j$ but $k = l$, we find

$$\begin{aligned}
{}_B\langle ij|\mathbf{H}_{2B}\,|kk\rangle_B &= \left(\frac{\langle ij|' + \langle ji|'}{\sqrt{2}}\right) \\
&\cdot \quad \left[-\frac{1}{2}\left(\mathbf{I}+\mathbf{S}\right)\left(\mathbf{A}\oplus\mathbf{A}\right) + U\mathbf{R}\right]|kk\rangle' \\
&= -\left(\frac{\langle ij|' + \langle ji|'}{\sqrt{2}}\right)\left(\mathbf{A}\oplus\mathbf{A}\right)|kk\rangle' \\
&= -\frac{1}{\sqrt{2}}\big(A_{ik}\delta_{jk} + A_{jk}\delta_{ik} + A_{ik}\delta_{jk} \\
&+ \quad A_{jk}\delta_{ik}\big) \\
&= -\frac{2}{\sqrt{2}}\left(A_{ik}\delta_{jk} + A_{jk}\delta_{ik}\right). \qquad \text{(A.2)}
\end{aligned}$$

When $i = j$ and $k = l$, we have

$$\begin{aligned}
{}_B\langle ii|\mathbf{H}_{2B}\,|kk\rangle_B &= \langle ii|'\left[-\frac{1}{2}\left(\mathbf{I}+\mathbf{S}\right)\left(\mathbf{A}\oplus\mathbf{A}\right) + U\mathbf{R}\right]|kk\rangle' \\
&= U\,\langle ii|'\,\mathbf{R}\,|kk\rangle' \\
&= U\delta_{ik}. \qquad \text{(A.3)}
\end{aligned}$$

These expressions are all exactly the same as we found through the definition of the Hamiltonian in Eq. refbosonelements.

We can work the same exercise for the Fermion Hamiltonian, Eq. fermionoperatorham as we did for the Boson Hamiltonian in eq. A.1. The calculation for the fermions yields

$${}_F\langle ij|\mathbf{H}_{2F}\,|kl\rangle_F = \delta_{ik}A_{lj} + \delta_{jl}A_{ik} - \delta_{il}A_{jk} - \delta_{jk}A_{il}, \qquad \text{(A.4)}$$

which is identical to the result obtained from eq. 2.7.

A.2 Counting the elements in the non-interacting Boson evolution matrix

To prove that the two-particle walk cannot distinguish two non-isomorphic SRGs, we use the method that Shiau et al. introduced for one-particle walks; we show that all the values and degeneracies GFs, matrix elements of the evolution operator, can be expressed of functions

of the SRG family parameters. For one particle, Shiau et al. [40] considered the on-diagonal and off-diagonal matrix elements separately. For the two-particle evolution operator $\mathbf{U}_{2B}$, we perform a similar trick by partitioning the matrix elements according to two parameters (a, b): the total number of distinct indices (a) and the number of indices shared the left and right sides (b). For example, $\langle 34| U_B |24\rangle$ falls into the element class $(3, 1)$, since it has three distinct indices (2,3,4) and the left and right side have one index in common (2). In total, the two-particle Boson evolution operator has seven such classes: $(4, 0)$, $(3, 0)$, $(3, 1)$, $(2, 0)$, $(2, 1)$, $(2, 2)$, and $(1, 2)$, which together partition the set of matrix elements.

Within each of these classes, the various possible element values are listed in table 2.1. Counting the number of occurrences is performed by means of combinatorial sums. First, we consider the symmetry class (4,0). Since $i \neq j$ and $k \neq l$, we use eq. 2.5 to write the matrix elements as

$$\begin{aligned}
\langle ij| \mathbf{U}_B |kl\rangle &= \alpha^2(\delta_{ik}\delta_{jl} + \delta_{il}\delta_{jk}) + 2\beta^2 \\
&+ \gamma^2(A_{ik}A_{jl} + A_{il}A_{jk}) \\
&+ \alpha\beta(\delta_{ik} + \delta_{jk} + \delta_{il} + \delta_{jl}) \\
&+ \alpha\gamma(\delta_{ik}A_{jl} + \delta_{jk}A_{il} + \delta_{il}A_{jk} + \delta_{jl}A_{ik}) \\
&+ \beta\gamma(A_{jl} + A_{il} + A_{jk} + A_{ik}). \qquad \text{(A.5)}
\end{aligned}$$

One possible value for this matrix element, $4\beta\gamma+2\gamma^2+2\beta^2$, occurs when $A_{jl} = A_{il} = A_{jk} = A_{ik} = 1$. Since $\mathbf{A}$ is a $0-1$ matrix, the number of ways this can occur, $n_{(4,0)a}$, is given by

$$\begin{aligned}
n_{(4,0)a} &= \sum_{i<j}\sum_{k<l} A_{jl}A_{il}A_{jk}A_{ik} \qquad \text{(A.6)} \\
&= \frac{1}{4}\sum_{ijkl} A_{jl}A_{il}A_{jk}A_{ik}(1-\delta_{ij})(1-\delta_{kl}) \\
&= \frac{1}{4}\Big(\sum_i (A^4)_{ii} - 2\sum_{ij}(A^2)_{ij} + \sum_{ij} A_{ij}\Big),
\end{aligned}$$

where the initial sum is constrained to $i < j$ and $k < l$ since we are working with indistinguishable Bosons, and hence have a space of dimension $N(N+1)/2$. By repeated use of eq. 2.13, we can use the techniques of the one-particle algorithm [40] to evaluate these sums in

terms of family parameters. The values of those pertinent to our present discussion are:

$$\begin{aligned}
\sum_{ij} A_{ij} &= kN \\
\sum_{ij} (A^2)_{ij} &= N(k-\mu) + kN(\lambda-\mu) + N^2\mu \\
\sum_{ij} (A^3)_{ij} &= N\left(k^2 + k\big(\mu(N+\mu-2) + \lambda^2 - 2\lambda\mu + \lambda\big)\right. \\
&+ \left.(N-1)\mu(\lambda-\mu)\big)\right. \\
\sum_{i} (A^3)_{ii} &= kN\lambda \\
\sum_{i} (A^4)_{ii} &= kN\left(\mu(k-\lambda-1) + k + \lambda^2\right). \qquad \text{(A.7)}
\end{aligned}$$

Plugging in these results and using the SRG relationship $(N-k-1)\mu = k(k-\lambda-1)$, we find

$$\begin{aligned}
n_{(4,0)a} &= 1/4 \cdot N\big(k^2(\mu+1) + k\left(\lambda^2 - \lambda(\mu+2) + \mu - 1\right) \\
&- 2(N-1)\mu\big). \qquad \text{(A.8)}
\end{aligned}$$

A second possible value for this matrix element is $3\beta\gamma + \gamma^2 + 2\beta^2$, obtained by setting any one of A_{jl}, A_{il}, A_{jk}, or A_{ik} to zero. As a sum, this means that the number of occurrences, $n_{(4,0)b}$, is

$$\begin{aligned}
n_{(4,0)b} &= 4\sum_{i<j}\sum_{k<l} A_{jl}A_{il}A_{jk}(1-A_{ik})(1-\delta_{ik}) \\
&= \sum_{ijkl} A_{jl}A_{il}A_{jk}(1-A_{ik})(1-\delta_{ik})(1-\delta_{ij})(1-\delta_{kl}) \\
&= \sum_{ij}(A^3)_{ij} - \sum_{i}(A^3)_{ii} - \sum_{i}(A^4)_{ii} \\
&= N\mu(N-k-1)(k+\lambda-\mu), \qquad \text{(A.9)}
\end{aligned}$$

where the initial factor of four is due to the four possible ways to pick the A, and $(1 - A_{ik})(1-\delta_{ik})$ constrains both $i \neq k$ and $A_{ik} = 0$. The remainder of the calculation proceeds similarly, and the results are listed in table 2.1.

Appendix B

Supplemental information for chapter 3

B.1 Computing multiplicities of values of matrix elements of the evolution operator for strongly regular graphs

Here we discuss how to compute the multiplicities of values of elements of evolution operators, or Green's functions, for SRGs. We show in this appendix that the multiplicity of a non-interacting three-particle Green's function is in general not a function of SRG family parameters. This result is used in Section 3.3 to demonstrate how two-particle and three-particle non-interacting walks have different distinguishing powers for SRGs.

To compute the multiplicity of each value of the Green's function in a non-interacting three-particle walk, we first note that Eqs. (3.10) through (3.12) imply that the value of a given Green's function depends on the relationships between the vertices in the final state (the bra; $\{i, j, k\}$) and the vertices in the initial state (the ket; $\{p, q, r\}$). For each pair of indices (x, y), with x from the bra ($x \in \{i, j, k\}$), and y from the ket ($y \in \{p, q, r\}$), there are three possible relations. The vertices can be connected ($A_{xy} = 1$), the vertices can be the same ($\delta_{xy} = 1$), or the vertices can be different and disconnected ($A_{xy} = \delta_{xy} = 0$). Therefore, we may think of each Green's function as corresponding to a generalized subgraph

of the original graph. We say "generalized subgraph" because the Green's function is unaffected by internal connections within the initial or final state; we adopt the more compact terminology of referring to these generalized subgraphs as "widgets."

To illustrate this point, let us consider the widget shown in Figure B.1. The solid lines in the widget indicate that the sites are connected in the graph, while the dashed lines indicate that the value of the widget does not depend on whether or not those sites are connected. Thus, two widgets are considered the same whether or not sites that are connected by dashed lines are actually adjacent. To evaluate ${}_B\langle ijk|\mathbf{U}_{3B}|pqr\rangle_B$ for the widget shown in Figure B.1, we note that all six vertices ($\{i,j,k,l,p,q,r\}$) are distinct. We can then use Eqs. (3.10) and (3.12) to find that ${}_B\langle ijk|\mathbf{U}_{3B}|pqr\rangle_B = 6(\beta+\gamma)^3$, where β and γ, defined in (3.12), are functions of the SRG family parameters. The multiplicity of this particular value for a particular graph is given by the number of times its corresponding widget occurs in the graph.

To compute the multiplicity, M, of $6(\beta+\gamma)^3$ in $\mathbf{U}_{3B}$, we count the number of occurrences of this widget in the graph. To do this, we perform the following combinatorial sum, generalizing the procedure outlined in Appendix B of Gamble *et al.* [3].

$$\begin{aligned} M &= \sum_{i<j<k} \sum_{p<q<r} A_{ip}A_{iq}A_{ir}A_{jp}A_{jq}A_{jr}A_{kp}A_{kq}A_{kr} \\ &= \frac{1}{36} \sum_{ijkpqr} A_{ip}A_{iq}A_{ir}A_{jp}A_{jq}A_{jr}A_{kp}A_{kq}A_{kr} \times \\ &\quad (1-\delta_{ij})(1-\delta_{ik})(1-\delta_{jk})(1-\delta_{pq})(1-\delta_{pr})(1-\delta_{qr}). \end{aligned} \tag{B.1}$$

The analogous sums considered in Gamble *et al.*, which only examines two-particle walks, can be decomposed into sums and traces over powers of the adjacency matrix. Such operations are given by contracting over two occurrences of the same index in the summand. Conveniently, these quantities are expressible in terms of SRG family parameters, as is illustrated in chapter 2 Things are not so simple, however, for the three-particle walks. By inspection, we see that Eq. B.1 contains contractions over three occurrences of the same index. Such contractions correspond to neither matrix multiplication nor computing the trace, and cannot in general be massaged into forms expressible in terms of SRG family

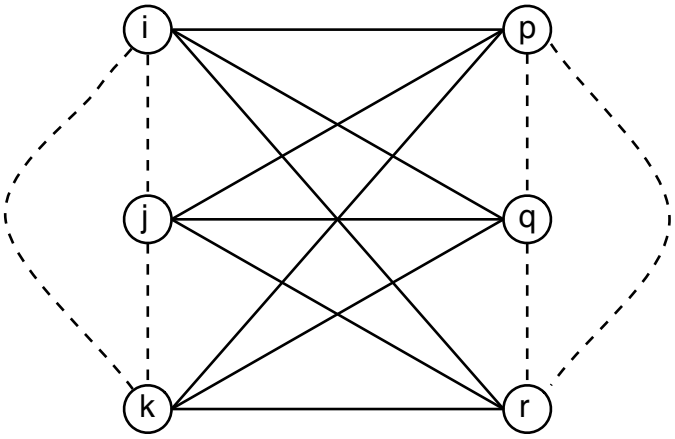

Figure B.1: Sketch of a generalized subgraph, or "widget," used to calculate the values and degeneracy of a Green's function for a three-particle quantum walk on an SRG. The vertices on the right side correspond to the vertices the particles are on to begin with (the ket $|pqr\rangle_B$ or $|pqr\rangle_F$), and the vertices on the left side correspond to the vertices the particles end up on (the bra ${}_B\langle ijk|$ or ${}_F\langle ijk|$), after application of the evolution operator U. A solid line between vertices x and y indicate that $A_{xy} = 1$. A dashed line between x and y means that the value of A_{xy} does not affect the value of the Green's function. Thus, for bosons, the depicted widget corresponds to the Green's function ${}_B\langle ijk|\mathbf{U}_{3B}|pqr\rangle_B$ when all six vertices are distinct, and when $A_{xy} = 1$ for all $x \in \{i, j, k\}$ and $y \in \{p, q, r\}$. Eqs. (3.10) and (3.12) show that the value of this Green's function, or widget, is ${}_B\langle ijk|\mathbf{U}_{3B}|pqr\rangle_B = 6(\beta + \gamma)^3$.

parameters, as evidenced by the fact that the three-particle walks have distinguishing power over many pairs of SRGs.

However, the above statement does not give us analytic proof that there exist Green's functions whose multiplicities are not functions of the family parameters; up to this point, we are still relying on the numerical results as proof. Below, we analytically demonstrate that there exist widgets whose multiplicities *cannot* be determined by family parameters. To demonstrate this, we take a step back to the two-particle walk. Consider the widget shown in Figure B.2(a). We can determine this widget's multiplicity for an arbitrary SRG with family parameters (N, k, λ, μ) by performing the combinatorial sum analogous to Equation (B.1), or equivalently, we can actually count the number of times we can fit this widget on the SRG. To begin, we pick two sites in the graph to serve as sites i and j; these sites may be adjacent or not, as indicated by the dashed line between them in the figure. Now we

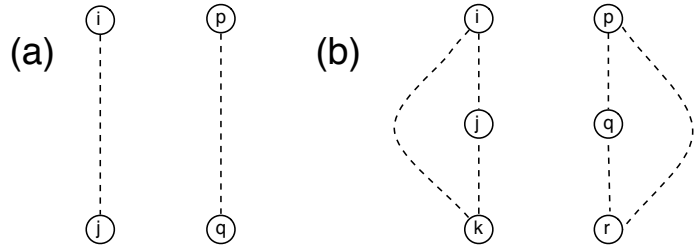

Figure B.2: Empty widgets for two-particle and three-particle non-interacting walks. In both widgets, all vertices are distinct and no vertex in the initial state is adjacent to any vertex in the final state. The values of the widgets depend only on the family parameters for both (a) and (b), while the degeneracies of these values depend only on family parameters for two particles but not for three. The multiplicity of each widget's respective Green's function for a particular SRG is equal to the number of times that widget appears in the SRG. (a) The empty widget for two particles. The number of times this widget appears in an SRG is a function of the SRG family parameters, as is the case for all two-particle widgets [3]. (b) The empty widget for three particles. The number of times this widget appears in an SRG is *not* a function solely of SRG family parameters. This is demonstrated by the graphs in Figure B.3. An analytic explanation for this phenomenon is given in the text following Equation (B.2).

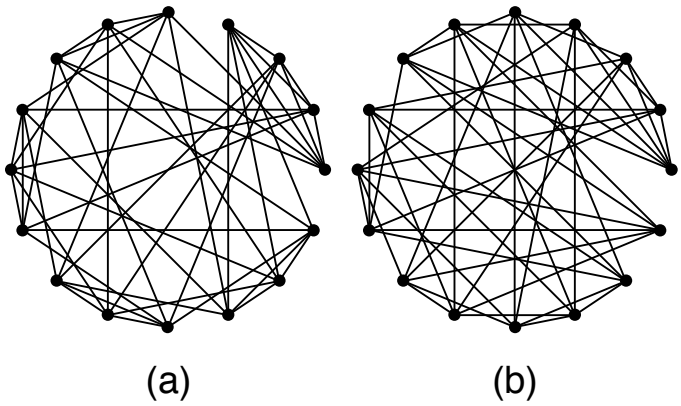

Figure B.3: The two non-isomorphic graphs of the SRG family (16,6,2,2). The widget of Figure B.2(b) appears in the graph shown in (a) 608 times, whereas the same widget appears in the graph shown in (b) 512 times. Thus we see that the same three-particle widget can have different multiplicities in graphs of the same family, so the three-particle non-interacting walk can distinguish at least some non-isomorphic graphs from the same SRG family.

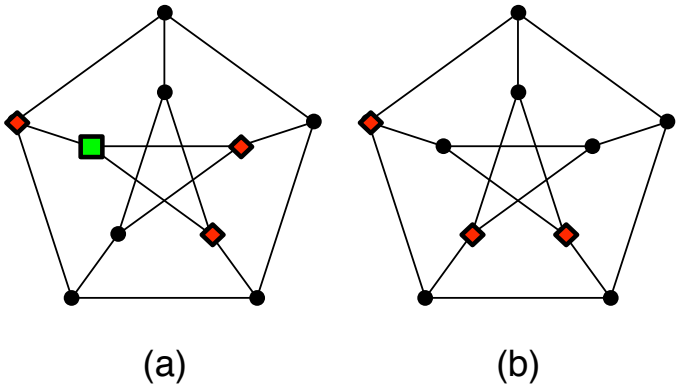

Figure B.4: Two copies of the Petersen graph, an SRG with parameters $(10, 3, 0, 1)$. In each graph, three mutually non-adjacent vertices are highlighted as red diamonds. In (a), the three vertices share one common neighbor, marked as a green square. In (b), the three vertices share no common neighbors. This demonstrates that the number of neighbors common to a triple of vertices in a strongly regular graph is not strictly a function of the SRG family parameters, thus showing why widget multiplicity is not strictly governed by family parameters when $p \geq 3$.

must count, given our choice of i and j, how many sites we may pick as p and q. If i and j are connected, there are $\binom{N-2k+\lambda}{2}$ choices for p and q, whereas if i and j are disconnected, there are $\binom{N-2-2k+\mu}{2}$ choices for p and q. There are $\frac{Nk}{2}$ choices for connected sites that can serve as i and j, and $\binom{N}{2} - \frac{Nk}{2}$ disconnected sites. Thus, the number of four-vertex empty widgets occurring in a two-particle non-interacting walk is:

$$M_{2,empty} = \frac{Nk}{2}\binom{N-2k+\lambda}{2} + \left(\binom{N}{2} - \frac{Nk}{2}\right)\binom{N-2-2k+\mu}{2}, \tag{B.2}$$

in agreement with the result in Gamble *et al.* for this particular widget [3]. Thus we see that this widget's multiplicity is, as expected, a function of the family parameters. Let's see what happens when we try this same approach for the corresponding widget in the three-particle walks, shown in Figure B.2(b). Again, we consider the multiplicity of the widget in an arbitrary SRG by counting the number of times we can fit this widget on the graph.

Now we pick three sites to serve as i, j, and k. We want to count, given our choice of i, j, and k, the number of sites that can serve as p, q, and r. To do this, we need to know how i, j, and k are connected amongst themselves, just as we did in the previous example. There are four possible non-isomorphic connectivities, as there can be between zero and three connections amongst these sites. In order to count the multiplicity of this widget, we must consider for each of these four cases how many sites in the graph are mutually disconnected from sites i, j, and k. In the previous example, we could answer the analogous question via the family parameters, as illustrated above. However, this is because the family parameters μ and λ tell us how many common neighbors *pairs* of vertices have. There are no family parameters which encode this information for *triples* of vertices, as strong regularity does not place absolute constraints on shared connectivities for triples of vertices.

We illustrate this point with an example in Figure B.4. Two copies of the Petersen graph, an SRG with family parameters $(10, 3, 0, 1)$ are depicted. The first copy highlights three mutually non-adjacent vertices; this particular triple of vertices has one common neighbor. The second copy also highlights a triple of mutually non-adjacent vertices, but this triple has *no* shared neighbors. Thus we have demonstrated by example that strong regularity cannot in general uniquely determine the shared connectivity for triples of vertices.

Moreover, we can see that counting the multiplicity of the widget shown in Figure B.2(b) can be used to distinguish two non-isomorphic graphs from the same SRG family. Figure B.3 shows the two non-isomorphic graphs in the SRG family (16,6,2,2). The widget in Figure B.2(b) appears 512 times in the first graph and 608 times in the second graph, thus distinguishing them.

We conclude then that there exist three-particle widgets whose multiplicities *cannot* be functions of family parameters. Thus, the three-particle non-interacting walks are *not* forbidden from distinguishing non-isomorphic SRGs from the same family, unlike the two-particle non-interacting walks.

B.2 Computing the number of SRG fingerprints

In Section 3.3, it is shown that quantum walks of p non-interacting particles cannot distinguish all non-isomorphic pairs of strongly regular graphs. This is done by showing that $Z(p, N)$, the number of graph fingerprints given by the p-boson walk on an SRG family with N vertices, is less than the number of non-isomorphic strongly regular graphs with N vertices, in the limit of large N. This subsection presents the calculation of $Z(p, N)$.

To calculate $Z(p, N)$, we note that if there are X_p possible Green's function values for the p-boson walk, and Y elements of the evolution operator U, then computing the number of unique fingerprints is equivalent to computing the number of ways one can put Y indistinguishable balls in X_p labeled bins, so that [201]

$$Z(p, N) = \binom{X_p + Y - 1}{X_p - 1}. \tag{B.3}$$

We recall that X_p is a function of p, but not of N. (We may think of X_p as the number of uniquely-valued widgets that appear in the p-boson walk.) However, Y, the number of elements in the evolution operator, will depend on both p and N, and we henceforth write it as $Y_{p,N}$. The dimension of the evolution operator is computed by determining how many different ways p bosons can be put on N vertices, which this is the same problem as computing the number of ways to put p indistinguishable balls into N labeled bins. The number of elements in the evolution operator is just the square of its dimension, so we find that:

$$Y_{p,N} = \binom{N + p - 1}{p}^2. \tag{B.4}$$

Using Equations (B.3) and (B.4), we now compute an upper bound for $Y_{p,N}$ and Z. It can be shown that $\binom{n+k-1}{k-1} \leq n^k$ when $n \geq 2$ and $k \geq 1$. Thus

$$Y_{p,N} < \binom{N + p}{p}^2 \leq N^{2(p+1)} \tag{B.5}$$

and

$$Z(p, N) \leq (Y_{p,N})^{X_p} < N^{2X_p(p+1)}. \tag{B.6}$$

Therefore, the maximum number of unique graphs the p-boson walk can distinguish is bounded above by $N^{2X_p(p+1)}$. We use this result in Section 3.3 to show that there exist SRGs that a particular p-particle walk cannot distinguish.

B.3 Bounding the number of widgets in the non-interacting p-particle walk

Here, we show that $\log_2 X_p \sim p^2$, where X_p is the number of distinct widgets for the non-interacting p-boson walk. First, Auluck proved there are $e^{O(p^{2/3})}$ widgets with no edges [202]. (He counted bipartitions of (p, q), which may be considered to be edgeless widgets when $p = q$.) Since there are at most 2^{p^2} ways to add edges to one of these, we have the upper bound $X_p \leq 2^{p^2+O(p^{2/3})}$. To get a lower bound, it will suffice to consider the widgets with $2p$ distinct indices. The edges in one of these can be specified by a $p \times p$ array of bits, and the widgets isomorphic to it are obtained by permuting rows, permuting columns, or transposing the matrix. Therefore, by Burnside's counting lemma [203], the number of isomorphism classes of widgets of this type is

$$\frac{1}{|F|} \sum_{f \in F} [\ \#\ \text{of arrays fixed by}\ f\ ],$$

where the finite group F is the semidirect product of $S_p \times S_p$ by S_2. (S_p and S_2 are the symmetric groups on p and 2 objects, respectively.) This is lower bounded by the term coming from $f = 1$, which is $2^{p^2}/(2(p!)^2))$, and this is $2^{p^2+O(p \log p)}$ by Stirling's formula. From these two estimates the result of Equation (3.19) follows.

Error analysis for numerical computations

When comparing two graphs, we compute Δ, a measure of the distance between the lists of matrix elements of the evolution operators for the two graphs, as defined in Eq. (3.9). Computing Δ requires comparing two lists of numbers that are each exponentially large in particle number p. An evolution operator for a walk of p non-interacting fermions on a graph with N vertices has $\binom{N}{p}^2$ elements, and the boson equivalent has $\binom{N+p-1}{p}^2$ elements.

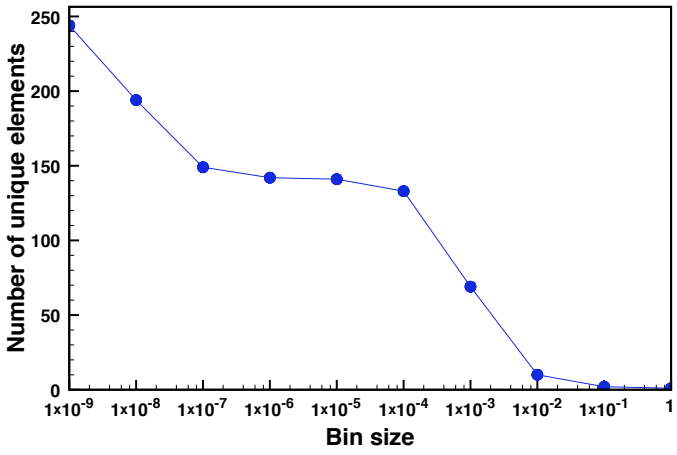

Figure B.5: The number of numerically distinguished elements in the evolution operator $\mathbf{U}(t)$, defined in Equation (3.8) as a function of the bin size used in grouping the elements. This plot is for the non-interacting three-fermion walk on a graph in the SRG family (16,6,2,2). We see that the actual number of unique elements is about 150, which can be obtained by using a bin size in the range of 10^{-7} to 10^{-4}.

For example, the evolution operator for the non-interacting four-fermion walk on a graph of 35 vertices has over 2.7 billion elements.

The comparison of the lists can be made much more efficient by exploiting the fact that the values in the list are highly degenerate. Instead of comparing the entries in a list, we make histograms of element values and their multiplicities. We then compute Δ by comparing these histograms. When constructing the histograms, it is important to determine the correct bin size. Choosing too large a bin size results in falsely grouping distinct elements together, while choosing too small a bin size results in falsely distinguishing elements. By constructing a series of histograms with different bin sizes for the same evolution operator, we are able to determine a range of bin sizes which are neither too large nor too small. This is illustrated in Figure B.5, which shows that for the non-interacting three-fermion walk on a graph in $(16, 6, 2, 2)$, an appropriate bin size is between 10^{-7} and 10^{-4}.

Because we compute Δ via numerical simulation, we expect there to be some numerical noise floor. That is, for any two permutations of the same graph, we expect

$\Delta > 0$. It is important to determine how big this quantity, which we denote Δ_{iso}, will be. We only consider two non-isomorphic graphs to be distinguished if they yield a Δ which satisfies $\Delta \gg \Delta_{iso}$.

We numerically compute Δ_{iso} using double precision arithmetic for a variety of random permutations on our graphs, and we find a maximum Δ_{iso} to be approximately 10^{-6}. Thus, only graph pairs which yield a $\Delta > 10^{-6}$ are considered distinguished. We find Δ_{iso} to be relatively insensitive to graph size and particle number.

In practice, we see a gap for Δ between distinguished graph pairs and non-distinguished graph pairs. For distinguished graphs, we find Δ at least two orders of magnitude larger than Δ_{iso} (usually much larger); non-distinguished graph pairs have values of Δ are approximately equal to Δ_{iso} or are even smaller than it.

Appendix C

Supplemental information for chapter 4

C.1 Parameters of Web Graph Models

In implementing the models used in chapter 4, the relationship between the parameters of the network generation algorithms and the generated networks themselves is not always obvious, so in the following section we explain it in detail.

GZL Preferential Attachment

The method of graph construction in the GZL Preferential Attachment Model [71] consists of two phases, each with its own parameter. First, a graph X (with adjacency matrix A_X) is created by adding a new vertex at each time step, where each vertex is created with m_X out-going edges. Next, a second graph Y (with adjacency matrix A_Y) is created in the same fashion, only with each new vertex having m_Y in-coming edges. A_X and A_Y are then added together, with loops and weights discarded, forming the adjacency matrix of the desired network. m_X and m_Y are the two parameters to consider in this algorithm.

In order for a graph to be scale-free, $\Pr(d_{in} = k)$ and $\Pr(d_{out} = k)$, the probabilities that the in-degree d_{in} and the out-degree d_{out} of a random node have the value k, must

satisfy

$$\Pr(d_{in} = k) \sim k^{-\gamma_{in}}, \tag{C.1}$$
$$\Pr(d_{out} = k) \sim k^{-\gamma_{out}},$$

where γ_{in} and γ_{out} are positive real numbers, and it is understood that $\Pr(d_{in} = k) = 0$ when $k < m_X$ and $\Pr(d_{out} = k) = 0$ when $k < m_Y$. To compute γ_{in} and γ_{out}, one starts from the undirected version from Ref. [204]. This result is then combined with a constant offset, since each vertex of X has m_x outgoing edges and each vertex of Y has m_Y incoming edges. The resulting composite probability distributions follow

$$\Pr(d_{in} = k) \sim (k + m_X - m_Y)^{-3}, \tag{C.2}$$
$$\Pr(d_{out} = k) \sim (k - m_X + m_Y)^{-3}.$$

Thus, for sufficiently large k, these distributions are scale-free. However, for a large range of intermediate k, we expect substantial deviation from the power law dependence of Eq. (C.1). According to GZL [81], the parameters used to generate Fig. 2 in their paper [71], which provides the main evidence for logarithmic scaling of the gap, follow $m_Y \gg m_X$. In Fig. C.1, we show the degree distributions for such a network, where we set $m_X = 1$ and $m_Y = 15$. There, we see that the degree distributions are well-described by Eq. (C.2), and that the addition process does indeed distort the degree distributions. By requiring $m_X = m_Y$, as we have done in this paper (and GZL did for a portion of their supplemental material [71]), $\gamma_{in} = \gamma_{out} = 3$ for all k, meaning that the in-degrees and out-degrees both follow the desired power law behavior.

The asymptotic (large number of nodes) value of average edges per node for the composite graph is also determined by the parameters m_X and m_Y. Because m_X is the number of out-going edges per vertex in graph X, it is also the average number of edges per vertex in X. The same logic holds for m_Y and graph Y. Thus, when constructing the composite graph, the asymptotic average edges per node would be simply $m_X + m_Y$. Although loops are then eliminated from the composite graph, the expected number of loops is much less than n in the large-n case, so this has little effect on the average edges per node. To produce

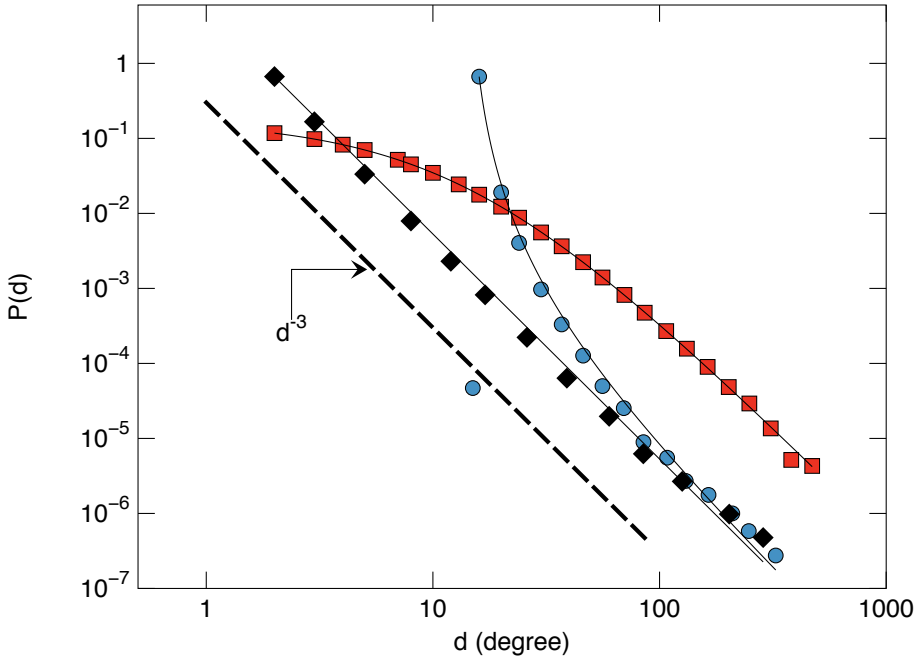

Figure C.1: Degree distributions for the GZL preferential attachment model with $m_X = 1$ and $m_Y = 15$, taken at graph size $n = 8196$ and averaged over approximately 1000 random graph realizations. Both the in-degree (blue circles) and out-degree (red squares) distributions are shown. For reference, the in-degree distribution for $m_X = 1$ and $m_Y = 1$ (duplicated from Fig. 4.2 of the main text is shown (black diamonds). The dashed line is the expected power law scaling of d^{-3}, which is applicable for large d. As predicted by Eq. (C.2), shown as fitting curves, the $m_X = 1$ and $m_Y = 15$ distributions exhibit non-scale-free behavior over a wide region of d.

a graph with $\gamma_{in} = \gamma_{out} = 3$ and average in- and out-edges per node of 2 (as in Fig. 2 of the main text), we use this model with $m_X = m_Y = 1$.

GZL Copying Model

The parameters of the GZL Copying Model [71] are similar to the GZL Preferential Attachment, as they both involve the adding of two graphs to form a composite graph. We again have the parameters m_X and m_Y, which again indicate the number of out-going edges per node in one component graph and the number of in-coming edges per node in the other.

This model has two new parameters, p_X and p_Y, which are the probabilities of a new node connecting to nodes chosen uniformly at random at a given time step during the

construction of X and Y, respectively. We follow Ref. [80] and add a constant offset (just as in the preferential attachment case). Doing so, we again obtain the result that the graphs are scale-free only for $m_X = m_Y$. Assuming this constraint, the composite graph follows

$$\gamma_{in} = \frac{2 - p_X}{1 - p_X}, \tag{C.3}$$

$$\gamma_{out} = \frac{2 - p_Y}{1 - p_Y}. \tag{C.4}$$

For the data in Fig. 2 of the main text, we used the parameters $p_X = p_Y = 0.5$ and $m_X = m_Y = 1$. In Fig. 3 of the main text, we used $p_X = 1/11$ and $p_Y = 35/86$ and $m_X = m_Y = 1$.

α-Preferential Attachment

Just as in the GZL Copying Model, there are multiple possible actions at each time step in the α-Preferential Attachment Model [77], and each of these steps has an associated probability. p_1 is the probability of adding a new vertex with a single out-going edge, p_2 is the probability of adding a new vertex with a single in-coming edge, and $1 - p_1 - p_2$ is the probability of an edge being added to the existing network without the addition of a new vertex. α, the third parameter, measures how far the generated network deviates from the GZL preferential attachment model.

As laid out in Ref. [77], the relationship between these 3 parameters and the exponents is

$$\gamma_{in} = \frac{2 + (p_1 + p_2)\alpha - p_2}{1 - p_2}, \tag{C.5}$$

$$\gamma_{out} = \frac{2 + (p_1 + p_2)\alpha - p_1}{1 - p_1}. \tag{C.6}$$

The connection between these parameters and the average number of directed edges per node in the graph is clear when one considers that the probability that a new node will be added at a given time step is $p_1 + p_2$, and a new edge is added at each step.

Using these constraints, we can find appropriate values for the parameters for both Fig. 2 and Fig. 3 of the main text. In Fig. 2, we used $p_1 = p_2 = 0.25$, and $\alpha = 1$, and in Fig.

3, we used $p_1 = 0.415$, $p_2 = 0.0851$, and $\alpha = 0.0128$. These choices in parameters keep γ_{in} and γ_{out} fixed at our desired values, while simultaneously keeping the graph at an average of 2 in- and 2 out-edges per node.

C.2 Initial Conditions

For each of these models, it is necessary to specify an initial graph to seed the network growth. In our simulations we used a complete graph (including loops) with $m+1$ vertices, where m is the number of edges added per vertex (in the α-Preferential Attachment Model, we used $m = 1$).

C.3 Adaptive Binning

In the plots of the degree distributions (Figs. 2(e)-(f), Figs. 3(c)-(d), and Fig. C.1), numerical noise caused by few high-degree vertices leads to data which are difficult to interpret. In order to combat this, we use adaptive binning, which functions as follows. First, some sampling threshold s_t is set, which we take to be 200 in our analysis. If a given data point, corresponding to a degree, contains at least s_t samples, then it is included. If the data point instead has fewer than s_t samples, it is combined with nearby points until the aggregated samples total at least s_t. The weighted average degree and probability are then recorded.

Appendix D

Supplemental information for Chapter 5

D.1 Derivation of the power transfer rate

In this appendix, we briefly sketch the derivation of Eq. (5.1), the formal expression for the power transfer between two 2DEGs, using the methods of Ref. [100]. First, recall that we are interested in the scattering of two particles with initial (2D) momenta $(\mathbf{k}_1, \mathbf{k}_2)$ and final momenta $(\mathbf{k}'_1, \mathbf{k}'_2) = (\mathbf{k}_1 + \mathbf{k}, \mathbf{k}_2 - \mathbf{k})$. The transition rate Γ for the above process is given by the balance equation

$$\begin{aligned}\Gamma\left(\mathbf{k}_1, \mathbf{k}_2; \mathbf{k}'_1, \mathbf{k}'_2\right) &= S\left(\mathbf{k}_1, \mathbf{k}_2; \mathbf{k}'_1, \mathbf{k}'_2\right) \\ &\times \Big[f^{(1)}_{\mathbf{k}_1}\left(1 - f^{(1)}_{\mathbf{k}'_1}\right) f^{(2)}_{\mathbf{k}_2}\left(1 - f^{(2)}_{\mathbf{k}'_2}\right) \\ &- f^{(1)}_{\mathbf{k}'_1}\left(1 - f^{(1)}_{\mathbf{k}_1}\right) f^{(2)}_{\mathbf{k}'_2}\left(1 - f^{(2)}_{\mathbf{k}_2}\right) \Big],\end{aligned} \tag{D.1}$$

where S is the transition rate given that the appropriate states are available, $f^{(1)}$ is the Fermi-Dirac distribution function in layer one,

$$f^{(1)}_{\mathbf{k}} = \left[1 + \exp\left(\frac{E_{\mathbf{k}} - E_F}{k_B T}\right)\right]^{-1}, \tag{D.2}$$

where $E_{\mathbf{k}} = \hbar^2 k^2/(2m^*)$, E_F is the Fermi level, m^* is the effective mass, and T is the temperature in layer one, and $f^{(2)}_{\mathbf{k}}$ is likewise the Fermi-Dirac distribution function in layer

two. Note that here we restrict our attention to Fermi-Dirac distribution functions, but Eq. (D.1) remains valid even for non-equilibrium distribution functions.

The first term in the square brackets of Eq. (D.1) can be understood as the particles starting with momenta $(\mathbf{k}_1, \mathbf{k}_2)$ and ending with momenta $(\mathbf{k}'_1, \mathbf{k}'_2)$. The second term corresponds to scattering from momenta $(\mathbf{k}'_1, \mathbf{k}'_2)$ to momenta $(\mathbf{k}_1, \mathbf{k}_2)$. To calculate the scattering rate S, we use Fermi's golden rule:

$$S\left(\mathbf{k}_1, \mathbf{k}_2; \mathbf{k}'_1, \mathbf{k}'_2\right) = \frac{2\pi}{\hbar} |H|^2 \times \delta\left(E_{\mathbf{k}_1} + E_{\mathbf{k}_2} - E_{\mathbf{k}'_1} - E_{\mathbf{k}'_2}\right), \tag{D.3}$$

where H is the interaction matrix element,

$$H = \frac{q}{A} \tilde{\phi}_{scr}(k, d), \tag{D.4}$$

and $\tilde{\phi}_{scr}$ is the Fourier transformed screened Coulomb interaction between layers. Defining the Thomas-Fermi screening wavevector $k_{TF} = 2m^*/(\pi\hbar^2) \cdot q^2/(2\epsilon_0\epsilon_b)$, the Fourier-transformed screened Coulomb interaction between the layers, calculated within the Thomas-Fermi approximation is [99]:

$$\tilde{\phi}_{scr}(k, d) = \frac{kq}{4k_{TF}^2 \epsilon_0 \epsilon_b} \frac{1}{\sinh(kd)}, \tag{D.5}$$

where we have assumed $k \ll k_{TF}$. For clarity of presentation, we present a self-contained derivation of this expression in appendix D.2.

Now that we have an expression for the scattering rate between particular states, we obtain the power transfer between the layers:

$$P = 16 \sum_{\mathbf{k}_1, \mathbf{k}_2, \mathbf{k}} E \cdot \Gamma\left(\mathbf{k}_1, \mathbf{k}_2; \mathbf{k}_1 + \mathbf{k}, \mathbf{k}_2 - \mathbf{k}\right), \tag{D.6}$$

where the factor of 16 is due to spin degeneracies of two and valley degeneracies of two in each electron layer, [205] and $E = E_{\mathbf{k}_1+\mathbf{k}} - E_{\mathbf{k}_1}$, the transferred energy. Converting the sum to an integral gives us Eq. (5.1).

D.2 The screened Coulomb potential

In this appendix, we present a self-contained derivation of the screened interlayer Coulomb potential within the Thomas-Fermi approximation. Although this result can be obtained as a special case of the random phase approximation result as described in Ref. [99], assuming a static screening formalism from the beginning results in a considerably more transparent calculation. The technique we present here can also easily be implemented numerically to treat more complex geometries.

To start, we consider placing an electron into one of the 2DEGs. This results in an external, unscreened potential $\phi_{ext}(\mathbf{r}, z)$ due to the external electron, where $\mathbf{r}$ is the 2D position within the plane of the 2DEG. The electron gas in both layers can rearrange to screen this external charge, resulting in an induced potential $\phi_{ind}(\mathbf{r}, z)$. The screened potential that an electron in the other layer feels is then $\phi_{scr}(\mathbf{r}, d) = \phi_{ext}(\mathbf{r}, d) + \phi_{ind}(\mathbf{r}, d)$, where we have assumed that the two 2DEGs are separated by a distance d. Our objective is to calculate ϕ_{ind}, from which we can compute ϕ_{scr}.

We assume that our system is translationally invariant in the plane parallel to the 2DEGs, which we define to be the $x-y$ plane. It is convenient to exploit this translational invariance by taking a Fourier transform of the Poisson equation in the $x-y$ plane, yielding

$$\left(\partial_z \epsilon(z) \partial_z - \epsilon(z) k^2\right) \tilde{\phi}_{ind}(\mathbf{k}, z) = -\tilde{\rho}_{ind}(\mathbf{k}, z), \tag{D.7}$$

where we denote the Fourier transform of a function $f(\mathbf{r}, z)$ as

$$\tilde{f}(\mathbf{k}, z) = \int d^2 r f\left(\mathbf{r}, z\right) e^{-i\mathbf{r}\cdot\mathbf{k}}. \tag{D.8}$$

In Eq. (D.7), ρ_{ind} is the induced charge density, responsible for the production of ϕ_{ind}, and $\epsilon(z)$ is the dielectric function. In a homogeneous medium, Eq. (D.7) has the general solution [155]

$$\tilde{\phi}_{ind}(k, z) = \frac{1}{2k\epsilon_0\epsilon_b} \int dz' e^{-k|z-z'|} \tilde{\rho}_{ind}(k, z'), \tag{D.9}$$

so to find ϕ_{ind}, we must calculate ρ_{ind}.

To determine ρ_{ind}, we first note that the total charge density ρ_{tot} obeys

$$\rho_{tot}(\mathbf{r}, z) = \rho_0 + \rho_{ind}, \tag{D.10}$$

where ρ_0 is the charge density without an external charge present, and we have neglected the small density contribution from the external charge itself. The dispersion relation for the electrons is given approximately by

$$E(\mathbf{k}, \mathbf{r}, z) \approx \frac{\hbar^2 k^2}{2m^*} - q\phi_{scr}(\mathbf{r}, z), \tag{D.11}$$

where $-q$ is the charge on an electron. By using the functional form of the Fermi-Dirac distribution, we can view charge density as a functional of Fermi energy:[87]

$$\rho_{ind}(\mathbf{r}, z) \approx \rho_0 \left(E_F + q\phi_{scr}\right) - \rho_0 \left(E_F\right). \tag{D.12}$$

Now, assuming that $q\phi_{scr} \ll E_F$, to first order in ϕ_{scr} Eq. (D.12) is

$$\rho_{ind}(\mathbf{r}, z) \approx -q^2 \frac{dn_0}{dE}\Big|_{E_F} \phi_{scr}, \tag{D.13}$$

where $\rho_0 = -qn_0$. For low temperatures, $dn_0/dE\big|_{E_F} \approx g(\mathbf{r}, E_F)$, the local density of states evaluated at the Fermi level, which might vary spatially. For our geometry with two 2DEGs separated by a distance d, g only varies in the z direction:

$$g(z) = g_{2D} \left(\delta(z) + \delta(z - d)\right), \tag{D.14}$$

where g_{2D} is the energy-independent two-dimensional density of states.

Substituting Eq. (D.13) into Eq. (D.9), we find

$$\begin{aligned}\tilde{\phi}_{ind}(z) = -\frac{q^2 g_{2D}}{2k\epsilon_0\epsilon_b}\Big[&e^{-k|z|}\left(\tilde{\phi}_{ind}(0) + \tilde{\phi}_{ext}(0)\right) \\ &+ e^{-k|z-d|}\left(\tilde{\phi}_{ind}(d) + \tilde{\phi}_{ext}(d)\right)\Big].\end{aligned} \tag{D.15}$$

The external potential due to the external electron in the first 2DEG satisfies [103]

$$\tilde{\phi}_{ext}(k, z) = \frac{q}{2k\epsilon_0\epsilon_b} e^{-k|z|}. \tag{D.16}$$

Hence, evaluating Eq. (D.15) for $z = 0$ and $z = d$ leaves us with a system of two linear equations. Solving gives Eq. (D.5), where we note that the Thomas-Fermi screening wavevector k_{TF} is defined to be twice what is typical for GaAs, due to the extra valley degeneracy in Si, and we have assumed that $k \ll k_{TF}$.

D.3 Calculation of the power transfer

This appendix presents the derivation of Eq. (5.2). The calculation begins similarly to those done in the case of Coulomb drag.[99] However, it proceeds quite differently because the symmetry of the momentum transfer relevant to CD differs from that of power transfer, which we consider here. Following the CD literature,[99] we seek to decouple the k_1 and k_2 integrals. First, it is conventional to split the energy-conserving delta function in Fermi's golden rule by introducing an integration over the transfer energy. The relevant identity is [99]

$$\begin{aligned}&\delta\left(E_{\mathbf{k}_1}+E_{\mathbf{k}_2}-E_{\mathbf{k}_1+\mathbf{k}}-E_{\mathbf{k}_2-\mathbf{k}}\right) \\ &=\int dE\delta(E+E_{\mathbf{k}_1}-E_{\mathbf{k}_1+\mathbf{k}})\delta(E-E_{\mathbf{k}_2}+E_{\mathbf{k}_2-\mathbf{k}}).\end{aligned} \tag{D.17}$$

Next, note that Fermi-Dirac distributions at a common temperature T satisfy the algebraic relationship for two energies E_x and E_y [99]

$$f(E_x)\left(1-f(E_x+E_y)\right)=\frac{f(E_x)-f(E_x+E_y)}{1-e^{-E_y/(k_BT)}}. \tag{D.18}$$

A third, useful algebraic identity is

$$\frac{1}{1-e^{-a}}\frac{1}{1-e^{+b}}-\frac{1}{1-e^{+a}}\frac{1}{1-e^{-b}}=\coth b-\coth a, \tag{D.19}$$

which is verified by using the definition of the hyperbolic tangent. With these identities, it is tedious but straightforward to show that Eq. (5.1) can be written as

$$\begin{aligned}\frac{P}{A}=&\frac{16q^2}{\hbar(2\pi)^5}\int d^2kdE\cdot E\left|\tilde{\phi}_{tot}(k,d)\right|^2 I(\mathbf{k},E)J(\mathbf{k},E) \\ &\times\left[\coth\left(\frac{E}{k_BT_2}\right)-\coth\left(\frac{E}{k_BT_1}\right)\right],\end{aligned} \tag{D.20}$$

where

$$\begin{aligned}I(\mathbf{k},E)=&\int d^2k_1\delta(E+E_{\mathbf{k}_1}-E_{\mathbf{k}_1+\mathbf{k}}) \\ &\times\left[f^{(1)}(E_{\mathbf{k}_1})-f^{(1)}(E_{\mathbf{k}_1}+E)\right]\end{aligned} \tag{D.21}$$

and

$$J(\mathbf{k},E) = \int d^2k_2 \delta(E - E_{\mathbf{k}_2} + E_{\mathbf{k}_2-\mathbf{k}}) \times \left[f^{(2)}(E_{\mathbf{k}_2}) - f^{(2)}(E_{\mathbf{k}_2} - E) \right]. \tag{D.22}$$

Again, $f^{(1)}$ is the Fermi-Dirac distribution function of the active layer and $f^{(2)}$ is the Fermi-Dirac distribution function of auxiliary layer. We next make the simplifying assumption that the carriers in the two layers have have the same effective masses, but possibly different Fermi levels. Assuming that the temperature is sufficiently low, we also approximate the distribution functions as step functions at the Fermi level, from which it follows that $I(\mathbf{k},E) \approx -J(\mathbf{k},E)$ when the Fermi levels are the identical.

We calculate $I(\mathbf{k},E)$ within the effective mass approximation with a simple parabolic dispersion, $E = \hbar^2k^2/(2m^*)$, by using Cartesian coordinates and integrating over k_1, yielding:

$$I(\mathbf{k},E) = \frac{m^*}{\hbar^2 k}\sqrt{\frac{m^*}{2\hbar^2}}\mathrm{Re}\left(\sqrt{E_\beta} - \sqrt{E_\alpha}\right), \tag{D.23}$$

where m^* is the (transverse) effective mass, $E_\alpha = E_F - E_0 - E$, $E_\beta = E_F - E_0$, E_F is the Fermi level of active layer and

$$E_0 = \frac{\hbar^2}{2m^*}\left(\frac{k}{2} - \frac{Em^*}{\hbar^2 k}\right)^2. \tag{D.24}$$

It is now useful to switch to dimensionless coordinates, where we define $\zeta \equiv E/E_F$ and $\eta \equiv k/k_F$, where $k_F = \sqrt{2m^*E_F}/\hbar$ is the Fermi momentum. Doing this gives

$$I = \frac{m^*}{4\hbar^2}\cdot\frac{1}{\eta^2}\mathrm{Re}\Big(\sqrt{2(2+\zeta)\eta^2 - \eta^4 - \zeta^2} - \sqrt{2(2-\zeta)\eta^2 - \eta^4 - \zeta^2}\Big). \tag{D.25}$$

The calculation of J is very similar, except that the Fermi level of the auxiliary layer is taken to be E_F/x, where $x = n_1/n_2$ is the ratio of carrier densities. Recall that we wish to consider systems where $T_1 \gg T_2$. Hence, for simplicity we let $T_2 \approx 0$. Introducing the parameters $\zeta_0 \equiv k_B T_1/E_F$ and $\eta_0 \equiv 1/(k_F d)$ and substituting Eqs. (D.5) and (D.25) into Eq. (D.20) gives us

$$\frac{P}{A} = \frac{E_F^4}{64\hbar}\left(\frac{\epsilon_0\epsilon_b}{q^2}\right)^2 \int d\eta \left(\frac{\eta}{\sinh(\eta/\eta_0)}\right)^2 Y(\eta,\zeta_0), \tag{D.26}$$

which is Eq. (5.2), where Y is defined by Eq. (5.3).

D.4 Asymptotic analysis of heat transfer

In this appendix, we seek to obtain an accurate analytic expression for Eq. (5.2) for both large ($d \gg E_F/(k_F k_B T)$) and small ($d \ll E_F/(k_F k_B T)$) separations between the 2DEG layers. In the following, we set the densities of the two 2DEGs to be equal for simplicity. To, proceed, we first expand for small momentum excitations about the Fermi level. Using this, we work out the asymptotic form of Y (Eq. (5.3)) on either side of its peak. Then, we calculate the resulting integral in Eq. (5.2), and derive formulas for asymptotic power transfer for both large (Eq. (5.4)) and small (Eq. (5.5)) separations.

Asymptotic forms of Y

To begin, we calculate the asymptotic forms of Y. Since we are at low temperatures, we may assume that the transfer momentum $k \ll k_F$, the Fermi momentum. In this approximation, we find that

$$\begin{aligned} Y(\zeta, \eta_0) \approx & \int_0^{2\eta-\eta^2} \frac{\zeta(\coth(\zeta/\zeta_0)-1)}{\eta^3} \frac{4\zeta^2\eta^2}{4-\zeta^2/\eta^2} \\ & + \int_{2\eta-\eta^2}^{2\eta+\eta^2} \frac{\zeta(\coth(\zeta/\zeta_0)-1)}{\eta^3} \left[2(2+\zeta)\eta^2 - \eta^4 - \zeta^2\right]. \end{aligned} \tag{D.27}$$

The two limiting cases we consider are when $\eta \ll \zeta_0$, corresponding to the region well to the left of the peak in Y, and $\eta \gg \zeta_0$, corresponding to the right of the peak. When $\eta \ll \zeta_0$, we make the approximation that

$$\coth(\zeta/\zeta_0) \approx \zeta_0 - \zeta. \tag{D.28}$$

Using this, Eq. (D.27) reduces to

$$Y(\eta, \zeta_0) \underset{\eta \ll \zeta_0}{\sim} 4\zeta_0 \log(4/\eta)\eta^2. \tag{D.29}$$

When $\eta \gg \zeta_0$, we may take $\eta \gg \zeta$, so

$$\frac{3\zeta^2\eta^2}{4-\zeta^2/\eta^2} \approx \zeta^2\eta^2. \tag{D.30}$$

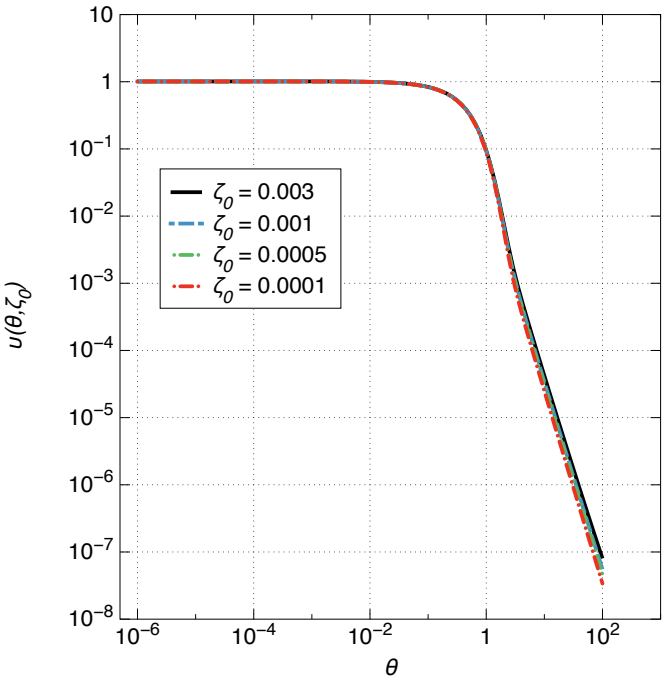

Figure D.1: The rescaled function $\upsilon(\theta)$ (Eq. (D.33)), plotted versus the scaled coordinate $\theta = \eta/\zeta_0$. Here, $\eta = k/k_F$, the momentum transfer scaled by the Fermi momentum, and $\zeta_0 = k_B T/E_F$. For small θ, υ takes on the expected asymptotic value of one. The curves essentially coincide until around $\theta \gtrsim 1$. This enables us to treat υ as approximately independent of ζ_0 before that point.

In this limit, the second integral in Eq. (D.27) does not contribute. Evaluating the first integral, we find

$$Y(\eta,\zeta_0) \underset{\eta\gg\zeta_0}{\sim} \frac{\zeta_0^4}{\eta}\int_0^\infty dx(\coth x - 1)x^3, \tag{D.31}$$

which reduces to

$$Y(\eta,\zeta_0) \underset{\eta\gg\zeta_0}{\sim} \frac{\zeta_0^4}{\eta}\frac{\pi^4}{120}. \tag{D.32}$$

Now that we have the asymptotic forms of Y on either side of the peak, we may proceed to evaluate Eq. (5.2) in the limits of $\eta_0 \ll \zeta_0$ and $\eta_0 \gg \zeta_0$.

Power transfer in the limit of large separation

Next, we evaluate Eq. (5.2) in the large-distance limit, when $\eta_0 \ll \zeta_0$, which corresponds to $d \gg E_F/(k_F k_B T)$. To do this, we first define a scaled function υ:

$$\upsilon(\theta, \zeta_0) \equiv \frac{Y(\theta\zeta_0, \zeta_0)}{4\zeta_0^3 \log(4/(\theta\zeta_0))\theta^2}, \tag{D.33}$$

which is just Y scaled by its asymptotic value in the region where $\eta \ll \zeta_0$ as a function of the scaled coordinate $\theta \equiv \eta/\zeta_0$. We plot υ for various values of ζ_0 in Fig. D.1.

The integral we need to evaluate can be written as

$$\Lambda(\eta_0, \zeta_0) \equiv 4\zeta_0^6 \int_0^\infty d\theta \frac{\theta^4 \log(4/(\theta\zeta_0))\upsilon(\theta, \zeta_0)}{\sinh^2(\theta\zeta_0/\eta_0)}, \tag{D.34}$$

which is related to Eq. 5.2 by

$$\frac{P}{A} = \frac{E_F^4}{64\hbar} \left(\frac{\epsilon_0 \epsilon_b}{q^2}\right)^2 \Lambda(\eta_0, \zeta_0). \tag{D.35}$$

Since we are in the region where $\eta_0 \ll \zeta_0$, we can approximate $\upsilon(\theta, \zeta_0) \sim 1$. The integration can then be carried out numerically, resulting in

$$\Lambda(\eta_0, \zeta_0) \underset{\eta_0 \ll \zeta_0}{\sim} \zeta_0 \eta_0^5 \left(8.3 - 13.0 \log \eta_0\right), \tag{D.36}$$

which reduces to Eq. (5.4) when inserted into Eq. (D.35).

Power transfer in the limit of small separation

Now, we evaluate Eq. (5.2) in the small-distance limit, when $\eta_0 \gg \zeta_0$, corresponding to $d \ll E_F/(k_F k_B T)$. We begin with Eq. (D.34), but unlike before we cannot assume that $\upsilon(\theta, \zeta_0) = 1$. Instead, we note that from Fig. D.1, υ is approximately independent of ζ_0 until some cutoff θ, $\theta_c \gtrsim 1$. Hence, we split the integration region of Λ into two pieces at θ_c. For $\theta < \theta_c$, we take υ to be independent of ζ_0, and also

$$\sinh(\theta\zeta_0/\eta_0) \approx \frac{\theta\zeta_0}{\eta_0}, \tag{D.37}$$

where this second approximation is valid since $\theta \leq \theta_c \ll \eta_0/\zeta_0$. For $\theta > \theta_c$, we calculate $\upsilon(\theta, \zeta_0)$ according to the asymptotic formula for Y in the limit of $\eta \gg \zeta_0$, given in Eq. (D.32).

These approximations result in

$$\Lambda(\eta_0,\zeta_0) \underset{\eta_0\gg\zeta_0}{\sim} 4\zeta_0^4\eta_0^2\int_0^{\theta_c} d\theta\,\log(4/(\theta\zeta_0))\theta^2\upsilon(\theta) + \frac{\pi^4}{120}\zeta_0^6\int_{\theta_c}^{\infty} d\theta\frac{\theta}{\sinh^2(\theta\zeta_0/\eta_0)}. \tag{D.38}$$

In the limit where $\zeta_0 \ll \eta_0$ and with $\theta_c = 2.0$, the result is

$$\Lambda(\eta_0,\zeta_0) \underset{\eta_0\gg\zeta_0}{\sim} \zeta_0^4\eta_0^2\left(0.458 - 1.32\log\zeta_0 + 0.182\log\eta_0\right). \tag{D.39}$$

In this evaluation, we picked $\zeta_0 = 0.001$ for the calculation of υ in the region where it is approximately ζ_0-independent. Inserting this result into Eq. (D.35) gives Eq. (5.5), as desired.

Appendix E

Supplemental information for Chapter 8

E.1 Convergence of the disorder expansion

In this appendix, we examine the convergence properties of the disorder-expansion method introduced in chapter 8. To do this, in Fig. E.1 we compare the performance of our disorder-expansion method in a 2D system to results obtained using the tight-binding method of Refs. [187, 9]. Specifically, Fig. E.1 (a) shows the x-component of the electric dipole moment $\mathbf{p}$, defined in Eq. (8.5). To be able to compare the disorder-expansion results to tight-binding in a reasonable time, we used a 2D system, so we altered the disorder from the single-atom square described in the main text. Analogous to the simple disorder in 3D used in the main text, here we consider a single-atom bump in $\hat{z}$ with x-width $W_x = 70.2$ nm, corresponding to 300 atoms. This 2D tight-binding problem can be computed in about 10 minutes on a personal computer and compared to the results of the disorder expansion. As in the main text, an electric field is applied along the $\hat{z}$ direction with strength 2×10^5 V/m, the dot has width $L = 28.3$ nm, and the quantum well is 10 nm thick with barrier height 150 meV.

In Fig. E.1 (a), the black curve is the tight-binding result, while the color lines indicate different numbers of z-basis functions: red is 2, blue is 10, green is 20, and purple is 40. In

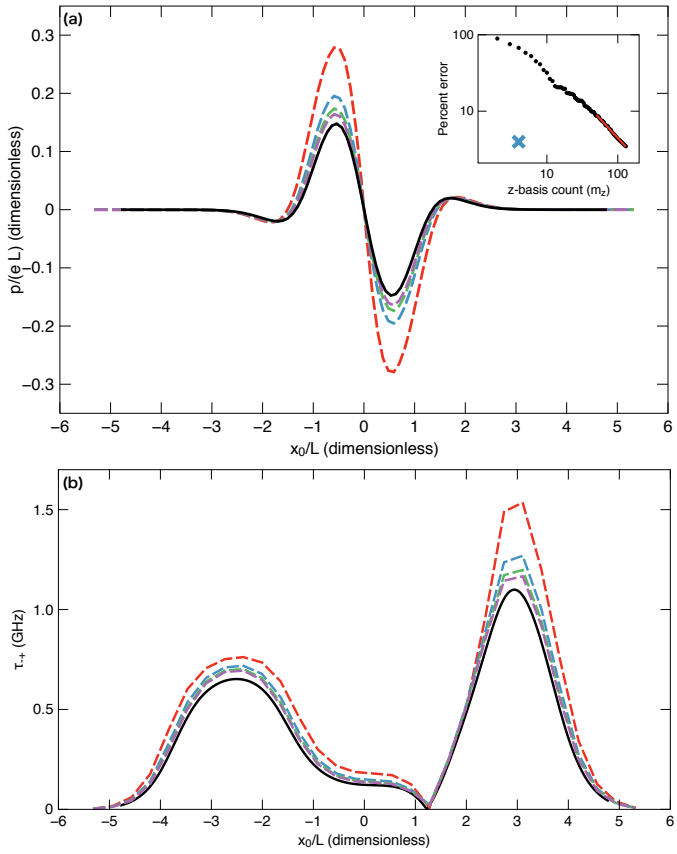

Figure E.1: (a): Comparison of disorder-expansion calculations for dipole moment with 2D tight-binding calculations. A bump one atom high in $\hat{z}$ with a width in $\hat{x}$ of 300 atoms is centered at the lateral position x_0. As in the main text, an electric field is applied along the $\hat{z}$ direction with strength 2×10^5 V/m, the dot has width $L = 28.3$ nm, and the quantum well is 10 nm thick with barrier height 150 meV. The black, solid curve is the tight-binding result, while the colored, dashed lines correspond to different numbers of z-basis functions: red is 2, blue is 10, green is 20, and purple is 40. In all cases, 5 x-basis functions were used. Assuming the tight binding results reflect exact solutions, the inset shows the percent error in the left peak of the main plot as a function of m_z, the number of z-basis functions used. The curve fit for large m_z indicates that the percent error scales like $m_z^{-1.005\pm0.007}$ for large m_z. The blue cross ($\times$) indicates the percent error obtained using eight z-functions from an augmented basis set described in Appendix A. (b): Comparison of disorder-expansion calculations for intervalley tunneling with 2D tight-binding calculations. The disorder and system parameters are identical to panel (a), except that two dots are used, and are separated by a distance $d = 150.3$ nm. As in panel (a), the black, solid line indicates tight-binding results, while the colored, dashed lines correspond to successively more z-basis functions. Even though tunneling is very sensitive to small tails of the wavefunctions along $\hat{x}$, the 35 x-basis functions used here are sufficient to ensure stability such that the number of z-basis functions used limits the accuracy.

all cases, 5 x-basis functions were used. As more z-basis functions are used, the disorder-expansion results become more accurate (*i.e.*, they approach the tight binding results). In order to quantify this further, we plot in the inset the percent error in the left peak as a function of m_z, the number of z-basis functions used. For large m_z, we observe that the error falls off like $m_z^{-1.005\pm0.007}$.

Fig. E.1 (b) shows the intervalley tunneling computed using both disorder-expansion and tight-binding techniques. As in panel (a), the black line corresponds to the 2D tight-binding calculation, while the colored lines corresponding to disorder-expansion calculations with different numbers of z-basis functions used. The system parameters used are identical to the dipole calculation, except that the disorder-expansion calculations use 35 x-basis functions in all cases, and there are two dots, separated by a distance $d = 150.3$ nm.

As is clear from Fig. E.1, the disorder-expansion technique does converge to the tight-binding results as expected, with the essential physics captured at a modest number of basis functions. However, this convergence can be slow, particulaly with respect to the $\hat{z}$ basis functions. This is because the perturbations we consider involve large energy scales, which effectively shift the positions of the $\hat{z}$ energy eigenstates. We are effectively trying to reconstruct this shift in position by including many unperturbed basis states.

We can achieve higher accuracy with fewer basis functions by tailoring our initial choice of basis to the particular type of disorder we include in our system. For example, the types of disorder that we considered in this paper all were of the form of single-atom bumps. This suggests that a better $z-$basis would be to include eigenstates not only of the unperturbed quantum well, but also a quantum well that is narrower by the bump height. Effectively, this means that we are supposing that the true $z-$solution will be a sum of eigenstates of the bare well and eigenstates of the well where the bump covers the entire system. By using this tailored basis, we can achieve very high accuracy with many fewer $z-$basis functions. In the inset of E.1 (a), the blue cross ($\times$) indicates the percent error obtained by using this augmented basis with only eight $z-$functions, demonstrating significantly better accuracy than the "brute-force" approach with significantly more basis functions.

Therefore, a promising direction for future study would be to develop physics-informed, tailored basis sets that can help speed convergence for more general forms of disorder.

E.2 Efficient computation of matrix elements

The initial, unperturbed basis used for the disorder-expansion calculation is separable in at least $\hat{z}$ and $\hat{x}-\hat{y}$ (and sometimes in $\hat{x}$ and $\hat{y}$ individually as well). The disorder perturbation mixes the eigenstates of the unperturbed problem, making them no longer separable. One can then use these 3D states to compute matrix elements of desired operators directly. However, we find that in practice the direct computation of these 3D matrix elements is computationally intensive, and often takes longer than the disorder-expansion calculation itself.

To bypass this bottleneck, we exploit the separability of our initial basis states in order to speed up calculation of matrix elements. While this procedure is not strictly necessary, it enables us to speed up our calculations greatly. We begin with the calculation of the dipole matrix element, Eq. (8.5) in the main text. For simplicity of presentation, we show here the computation of only p_x; the calculation of p_y follows similarly. Recalling the definition of the expansion in Eq. (8.4), we write

$$\begin{aligned} p_x &= \sum_{j,k,l,m} \int d^3rx \Big(\alpha^1_{jk}\alpha^1_{lm} F_j F_l \psi_k \psi_m - \alpha^0_{jk}\alpha^0_{lm} F_j F_l \psi_k \psi_m \Big) \\ &= \sum_{i,j,k} \left(\alpha^1_{jk}\alpha^1_{lk} - \alpha^0_{jk}\alpha^0_{lk} \right) \int dxdy \cdot xF_jF_l. \end{aligned} \tag{E.1}$$

Here, we suppress the arguments of the F and ψ functions for notational simplicity. From this, we see that to compute p_x, we can precompute the matrix

$$M^{p_x}_{j,l} = \int dxdy \cdot xF_jF_l, \tag{E.2}$$

which has dimension equal to the number of $x-y$ basis elements used. Then, computing p_x reduces to a simple sum:

$$p_x = \sum_{j,k,l,m} \left(\alpha^1_{jk}\alpha^1_{lk} - \alpha^0_{jk}\alpha^0_{lk} \right) M^{p_x}_{j,l}. \tag{E.3}$$

Finally, we note that in the case of an initial basis that is separable in both $\hat{x}$ and $\hat{y}$, the formula simplifies even further, since p_x is then diagonal in both $\hat{y}$ and $\hat{z}$.

Next, we consider the calculation of the intervalley tunneling matrix elements. We rewrite Eq. (8.6) from the main text as

$$\begin{aligned}\tau_{-+} = &\langle L_-| \left(V_{\mathrm{DD}}(x,y) - V_R(x,y)\right) |R_+\rangle \\ &+ \langle L_-| \left(\hat{T} + V_R(x,y) + V_z(z) + D(\mathbf{r})\right) |R_+\rangle ,\end{aligned} \tag{E.4}$$

where V_{DD} is the double-dot potential in the $x-y$ plane, V_R is the right-dot potential, $\hat{T}$ is the kinetic energy operator, and V_z is the unperturbed potential along $\hat{z}$. We have grouped the second term such that it forms the Hamiltonian corresponding to the $|R_+\rangle$ eigenstate, which lets us write

$$\tau_{-+} = \langle L_-| \left(V_{\mathrm{DD}}(x,y) - V_R(x,y)\right) |R_+\rangle + \epsilon_{R_+} \langle L_-|R_+\rangle , \tag{E.5}$$

where ϵ_{R_+} is the energy eigenvalue for $|R_+\rangle$. By using the same decomposition technique as we did for the dipole moment calculation, we can write

$$\tau_{-+} = \sum_{j,k,l} \alpha_{jk}^{L_-} \alpha_{lk}^{R_+} \left(M_{j,l}^A + \epsilon_{R_+} M_{j,l}^B\right) , \tag{E.6}$$

where the matrices are defined by

$$M_{j,l}^A = \int dxdy \left(V_{\mathrm{DD}}(x,y) - V_R(x,y)\right) F_j^L F_l^R, \tag{E.7}$$

and

$$M_{j,l}^B = \int dxdy F_j^L F_l^R. \tag{E.8}$$

Here, the superscript L and R denote basis functions in the left and right dots, respectively. As before, these matrices can be precomputed to increase computational speed, reducing the computation of τ_{-+} to a sum.

Bibliography

[1] T. Monz, P. Schindler, J. T. Barreiro, M. Chwalla, D. Nigg, W. A. Coish, M. Harlander, W. Hänsel, M. Hennrich, and R. Blatt, "14-qubit entanglement: Creation and coherence," *Phys. Rev. Lett.*, vol. 106, p. 130506, Mar 2011.

[2] D. Loss and D. P. DiVincenzo, "Quantum computation with quantum dots," *Phys. Rev. A*, vol. 57, pp. 120–126, Jan 1998.

[3] J. K. Gamble, M. Friesen, D. Zhou, R. Joynt, and S. N. Coppersmith, "Two-particle quantum walks applied to the graph isomorphism problem," *Phys. Rev. A*, vol. 81, p. 052313, May 2010.

[4] K. Rudinger, J. K. Gamble, M. Wellons, E. Bach, M. Friesen, R. Joynt, and S. N. Coppersmith, "Noninteracting multiparticle quantum random walks applied to the graph isomorphism problem for strongly regular graphs," *Phys. Rev. A*, vol. 86, p. 022334, Aug 2012.

[5] A. Frees, J. K. Gamble, K. Rudinger, E. Bach, M. Friesen, R. Joynt, and S. N. Coppersmith, "Power law scaling for the adiabatic algorithm for search engine ranking," 2012.

[6] J. K. Gamble, M. Friesen, R. Joynt, and S. N. Coppersmith, "Cooling of cryogenic electron bilayers via the coulomb interaction," *Phys. Rev. B*, vol. 84, p. 125321, Sep 2011.

[7] J. K. Gamble, M. Friesen, S. N. Coppersmith, and X. Hu, "Two-electron dephasing in single si and gaas quantum dots," *Phys. Rev. B*, vol. 86, p. 035302, Jul 2012.

[8] Z. Shi, C. B. Simmons, J. R. Prance, J. K. Gamble, T. S. Koh, Y.-P. Shim, X. Hu, D. E. Savage, M. G. Lagally, M. A. Eriksson, M. Friesen, and S. N. Coppersmith, "Fast hybrid silicon double quantum-dot qubit," *Phys. Rev. Lett.*, vol. 108, p. 140503, 2012.

[9] Z. Shi, C. B. Simmons, J. R. Prance, J. K. Gamble, M. Friesen, D. E. Savage, M. G. Lagally, S. N. Coppersmith, and M. A. Eriksson, "Tunable singlet-triplet splitting in a

few-electron si/sige quantum dot," *Applied Physics Letters*, vol. 99, no. 23, p. 233108, 2011.

[10] R. Motwani and P. Raghavan, "Randomized algorithms," *ACM Comput. Surv.*, vol. 28, no. 1, pp. 33–37, 1996.

[11] R. Aleliunas, R. M. Karp, R. J. Lipton, L. Lovasz, and C. Rackoff, "Random walks, universal traversal sequences, and the complexity of maze problems," in *SFCS '79: Proceedings of the 20th Annual Symposium on Foundations of Computer Science*, (Washington, DC, USA), pp. 218–223, IEEE Computer Society, 1979.

[12] Z. Trautt, M. Upmanyu, and A. Karma, "Interface mobility from interface random walk," *Science*, vol. 314, p. 632, Oct 2006.

[13] R. Sessions, M. Oram, and M. Szczelkun, "Random walk models for dna synapsis by resolvase," *J. Mol. Biol.*, vol. 270, pp. 413–425, Jan 1997.

[14] L. Kilian and M. P. Taylor, "Why is it so difficult to beat the random walk forecast of exchange rates?," *J. Int. Econ.*, vol. 60, no. 1, pp. 85 – 107, 2003.

[15] Y. Aharonov, L. Davidovich, and N. Zagury, "Quantum random walks," *Phys. Rev. A*, vol. 48, pp. 1687–1690, Aug 1993.

[16] E. Bach, S. Coppersmith, M. P. Goldschen, R. Joynt, and J. Watrous, "One-dimensional quantum walks with absorbing boundaries," *Journal of Computer and System Sciences*, vol. 69, no. 4, pp. 562 – 592, 2004.

[17] D. Solenov and L. Fedichkin, "Continuous-time quantum walks on a cycle graph," *Phys. Rev. A*, vol. 73, p. 012313, Jan 2006.

[18] A. Childs, E. Farhi, and S. Gutmann, "An example of the difference between quantum and classical random walks," *Quantum Inf. Process.*, Jan 2002.

[19] N. Shenvi, J. Kempe, and K. B. Whaley, "Quantum random-walk search algorithm," *Phys. Rev. A*, vol. 67, p. 052307, May 2003.

[20] A. Ambainis, "Quantum walks and their algorithmic applications," *International Journal of Quantum Information*, vol. 1, pp. 507–518, 2003.

[21] A. Ambainis, "Quantum walk algorithm for element distinctness," *Foundations of Computer Science, Annual IEEE Symposium on*, vol. 0, pp. 22–31, 2004.

[22] F. Magniez, A. Nayak, J. Roland, and M. Santha, "Search via quantum walk," in *STOC '07: Proceedings of the thirty-ninth annual ACM symposium on Theory of computing*, (New York, NY, USA), pp. 575–584, ACM, 2007.

[23] V. Potoček, A. Gábris, T. Kiss, and I. Jex, "Optimized quantum random-walk search algorithms on the hypercube," *Phys. Rev. A*, vol. 79, p. 012325, Jan 2009.

[24] D. Reitzner, M. Hillery, E. Feldman, and V. Bužek, "Quantum searches on highly symmetric graphs," *Phys. Rev. A*, vol. 79, p. 012323, Jan 2009.

[25] G. S. Agarwal and P. K. Pathak, "Quantum random walk of the field in an externally driven cavity," *Phys. Rev. A*, vol. 72, p. 033815, Sep 2005.

[26] K. Eckert, J. Mompart, G. Birkl, and M. Lewenstein, "One- and two-dimensional quantum walks in arrays of optical traps," *Phys. Rev. A*, vol. 72, p. 012327, Jul 2005.

[27] C. M. Chandrashekar and R. Laflamme, "Quantum phase transition using quantum walks in an optical lattice," *Phys. Rev. A*, vol. 78, p. 022314, Aug 2008.

[28] C. A. Ryan, M. Laforest, J. C. Boileau, and R. Laflamme, "Experimental implementation of a discrete-time quantum random walk on an nmr quantum-information processor," *Phys. Rev. A*, vol. 72, p. 062317, Dec 2005.

[29] B. C. Travaglione and G. J. Milburn, "Implementing the quantum random walk," *Phys. Rev. A*, vol. 65, p. 032310, Feb 2002.

[30] H. Schmitz, R. Matjeschk, C. Schneider, J. Glueckert, M. Enderlein, T. Huber, and T. Schaetz, "Quantum walk of a trapped ion in phase space," *Phys. Rev. Lett.*, vol. 103, p. 090504, Aug 2009.

[31] K. Manouchehri and J. B. Wang, "Quantum random walks without walking," *Phys. Rev. A*, vol. 80, p. 060304, Dec 2009.

[32] A. M. Childs, "Universal computation by quantum walk," *Phys. Rev. Lett.*, vol. 102, p. 180501, May 2009.

[33] D. A. Spielman, "Faster isomorphism testing of strongly regular graphs," in *Proceedings of the twenty-eighth annual ACM symposium on Theory of computing*, STOC '96, (New York, NY, USA), pp. 576–584, ACM, 1996.

[34] U. Schöning, "Graph isomorphism is in the low hierarchy.," *J. Comp. Syst. Sci.*, vol. 37, pp. 312–323, Jan 1988.

[35] P. W. Shor, "Algorithms for quantum computation: discrete logarithms and factoring," in *SFCS '94: Proceedings of the 35th Annual Symposium on Foundations of Computer Science*, (Washington, DC, USA), pp. 124–134, IEEE Computer Society, 1994.

[36] S. Hallgren, C. Moore, M. Rötteler, A. Russell, and P. Sen, "Limitations of quantum coset states for graph isomorphism," in *STOC '06: Proceedings of the thirty-eighth annual ACM symposium on Theory of computing*, (New York, NY, USA), pp. 604–617, ACM, 2006.

[37] C. Moore, A. Russell, and P. Sniady, "On the impossibility of a quantum sieve algorithm for graph isomorphism," in *STOC '07: Proceedings of the thirty-ninth annual ACM symposium on Theory of computing*, (New York, NY, USA), pp. 536–545, ACM, 2007.

[38] T. Rudolph, "Constructing physically intuitive graph invariants," *arXiv:quant-ph/0206068v1*, Jan 2002.

[39] V. Gudkov and S. Nussinov, "Graph equivalence and characterization via a continuous evolution of a physical analog," *arXiv:cond-mat/0209112v2*, Jan 2002.

[40] S. Shiau, R. Joynt, and S. Coppersmith, "Physically-motivated dynamical algorithms for the graph isomorphism problem," *Quantum Inf. Comput.*, vol. 5, pp. 492–506, Jan 2005.

[41] B. Douglas and J. Wang, "A classical approach to the graph isomorphism problem using quantum walks," *Journal of Physics A: Mathematical and Theoretical*, vol. 41, p. 075303, Feb 2008.

[42] D. Emms, E. Hancock, and S. Severini, "A matrix representation of graphs and its spectrum as a graph invariant," *Electron. J. Comb.*, Jan 2006.

[43] D. Emms, S. Severini, R. Wilson, and E. Hancock, "Coined quantum walks lift the cospectrality of graphs and trees," *Pattern Recogon.*, Jan 2009.

[44] R. Burioni, D. Cassi, I. Meccoli, M. Rasetti, S. Regina, P. Sodano, and A. Vezzani, "Bose-einstein condensation in inhomogeneous josephson arrays," *Europhys. Lett.*, vol. 52, p. 251, Nov 2000.

[45] P. Buonsante, R. Burioni, D. Cassi, and A. Vezzani, "Bose-einstein condensation on inhomogeneous networks: Mesoscopic aspects versus thermodynamic limit," *Phys. Rev. B*, vol. 66, p. 094207, Sep 2002.

[46] F. P. Mancini, P. Sodano, and A. Trombettoni, "Bec in a star-comb graph," *AIP Conference Proceedings*, vol. 918, p. 302, 2007.

[47] C. Godsil and G. Royle, *Algebraic Graph Theory*. Springer, 2001.

[48] E. M. Luks, "Isomorphism of graphs of bounded valence can be tested in polynomial time," *Journal of Computer and System Sciences*, vol. 25, pp. 42–65, 1982.

[49] E. W. Weisstein, "Strongly regular graph." `http://mathworld.wolfram.com/StronglyRegularGraph.html`, 2010.

[50] E. Spence, "Strongly regular graphs on at most 64 vertices." `http://www.maths.gla.ac.uk/~es/srgraphs.html`.

[51] B. McKay, "Combinatorial data." `http://cs.anu.edu.au/~bdm/data/graphs.html`.

[52] M. Karski, L. Förster, J.-M. Choi, A. Steffen, W. Alt, D. Meschede, and A. Widera, "Quantum walk in position space with single optically trapped atoms," *Science*, vol. 325, no. 5937, pp. 174–177, 2009.

[53] A. Schreiber, K. N. Cassemiro, V. Potoček, A. Gábris, P. J. Mosley, E. Andersson, I. Jex, and C. Silberhorn, "Photons walking the line: A quantum walk with adjustable coin operations," *Phys. Rev. Lett.*, vol. 104, p. 050502, Feb 2010.

[54] M. A. Broome, A. Fedrizzi, B. P. Lanyon, I. Kassal, A. Aspuru-Guzik, and A. G. White, "Discrete single-photon quantum walks with tunable decoherence," *Phys. Rev. Lett.*, vol. 104, p. 153602, Apr 2010.

[55] F. Zähringer, G. Kirchmair, R. Gerritsma, E. Solano, R. Blatt, and C. F. Roos, "Realization of a quantum walk with one and two trapped ions," *Phys. Rev. Lett.*, vol. 104, p. 100503, Mar 2010.

[56] J. O. Owens, M. A. Broome, D. N. Biggerstaff, M. E. Goggin, A. Fedrizzi, T. Linjordet, M. Ams, G. D. Marshall, J. Twamley, M. J. Withford, and A. G. White, "Two-photon quantum walks in an elliptical direct-write waveguide array," *New Journal of Physics*, vol. 13, no. 7, p. 075003, 2011.

[57] A. Peruzzo, M. Lobino, J. C. F. Matthews, N. Matsuda, A. Politi, K. Poulios, X.-Q. Zhou, Y. Lahini, N. Ismail, K. Wörhoff, Y. Bromberg, Y. Silberberg, M. G. Thompson, and J. L. OBrien, "Quantum walks of correlated photons," *Science*, vol. 329, no. 5998, pp. 1500–1503, 2010.

[58] L. Sansoni, F. Sciarrino, G. Vallone, P. Mataloni, A. Crespi, R. Ramponi, and R. Osellame, "Two-particle bosonic-fermionic quantum walk via integrated photonics," *Phys. Rev. Lett.*, vol. 108, p. 010502, Jan 2012.

[59] J. Smith, "arxiv:1004.0206v1," April 2010.

[60] C. Godsil and K. Guo, "Quantum walks on regular graphs and eigenvalues," *The Electronic Journal of Combinatorics*, vol. 18, no. 1, 2011.

[61] S. D. Berry and J. B. Wang, "Two-particle quantum walks: Entanglement and graph isomorphism testing," *Phys. Rev. A*, vol. 83, p. 042317, Apr 2011.

[62] F. W. Strauch, "Connecting the discrete- and continuous-time quantum walks," *Phys. Rev. A*, vol. 74, p. 030301, Sep 2006.

[63] K. Rudinger, J. K. Gamble, M. Wellons, E. Bach, M. Friesen, R. Joynt, and S. N. Coppersmith, "arxiv:1207.4535v1," July 2012.

[64] R. B. Sidje, "EXPOKIT. A software package for computing matrix exponentials," *ACM Trans. Math. Softw.*, vol. 24, no. 1, pp. 130–156, 1998.

[65] D. S. Stones, "The many formulae for the number of latin rectangles," *Electr. J. Comb.*, vol. 17, 2010.

[66] B. McKay and I. Wanless, "On the number of latin squares," *Annals of Combinatorics*, vol. 9, pp. 335–344, 2005. 10.1007/s00026-005-0261-7.

[67] L. K. Grover, "A fast quantum mechanical algorithm for database search," in *Proceedings of the twenty-eighth annual ACM symposium on Theory of computing*, STOC '96, (New York, NY, USA), pp. 212–219, ACM, 1996.

[68] D. Bacon and W. van Dam, "Recent progress in quantum algorithms," *Commun. ACM*, vol. 53, pp. 84–93, Feb. 2010.

[69] S. Brin and L. Page, "The anatomy of a large-scale hypertextual web search engine," *Computer Networks and ISDN Systems*, vol. 30, no. 1-7, pp. 107 – 117, 1998.

[70] P. Berkhin, "A survey on pagerank computing," *Internet Math*, vol. 2, no. 1, pp. 73–120, 2005.

[71] S. Garnerone, P. Zanardi, and D. A. Lidar, "Adiabatic quantum algorithm for search engine ranking," *Phys. Rev. Lett.*, vol. 108, p. 230506, Jun 2012.

[72] E. Farhi, J. Goldstone, S. Gutmann, and M. Sipser, "Quantum computation by adiabatic evolution," *arXiv:quant-ph/0001106v1*, 2000.

[73] A. L. Barabasi and R. Albert, "Emergence of scaling in random networks," *Science*, vol. 286, pp. 509–512, 1999.

[74] B. Bollobás, O. Riordan, J. Spencer, and G. Tusnády, "The degree sequence of a scale-free random graph process," *Random Structures and Algorithms*, vol. 18, no. 3, pp. 279–290, 2001.

[75] R. Cohen and S. Havlin, "Scale-free networks are ultrasmall," *Phys. Rev. Lett.*, vol. 90, p. 058701, Feb 2003.

[76] H. Tangmunarunkit, R. Govindan, S. Jamin, S. Shenker, and W. Willinger, "Network topology generators: degree-based vs. structural," in *SIGCOMM '02: Proceedings of the 2002 conference on Applications, technologies, architectures, and protocols for computer communications*, (New York, NY, USA), pp. 147–159, ACM, 2002.

[77] B. Bollobás, C. Borgs, J. Chayes, and O. Riordan, "Directed scale-free graphs," in *Proceedings of the fourteenth annual ACM-SIAM symposium on Discrete algorithms*, SODA '03, (Philadelphia, PA, USA), pp. 132–139, Society for Industrial and Applied Mathematics, 2003.

[78] A. Broder, R. Kumar, F. Maghoul, P. Raghavan, S. Rajagopalan, R. Stata, A. Tomkins, and J. Wiener, "Graph structure in the web," *Comput. Netw.*, vol. 33, pp. 309–320, June 2000.

[79] F. Chung and L. Lu, *Complex Graphs and Networks (Cbms Regional Conference Series in Mathematics)*. No. 107, Boston, MA, USA: American Mathematical Society, 2006.

[80] J. M. Kleinberg, R. Kumar, P. Raghavan, S. Rajagopalan, and A. S. Tomkins, "The web as a graph: measurements, models, and methods," in *Proceedings of the 5th annual international conference on Computing and combinatorics*, COCOON'99, (Berlin, Heidelberg), pp. 1–17, Springer-Verlag, 1999.

[81] S. Garnerone private communication, 2012.

[82] J. Nelder and R. Mead, "A simplex method for function minimization," *Computer Journal*, vol. 7, pp. 308–313, 1965.

[83] M. Xiao, I. Martin, E. Yablonovitch, and H. W. Jiang, "Electrical detection of the spin resonance of a single electron in a silicon field-effect transistor," *Nature*, vol. 430, pp. 435–439, 2004.

[84] C. Barthel, M. Kjærgaard, J. Medford, M. Stopa, C. M. Marcus, M. P. Hanson, and A. C. Gossard, "Fast sensing of double-dot charge arrangement and spin state with a radio-frequency sensor quantum dot," *Phys. Rev. B*, vol. 81, p. 161308, Apr 2010.

[85] M. Dolev, M. Heiblum, V. Umansky, A. Stern, and D. Mahalu, "Towards identification of a non-abelian state: observation of a quarter of electron charge at $\nu=5/2$ quantum Hall state," *ArXiv e-prints*, Feb. 2008.

[86] C. B. Simmons, J. R. Prance, B. J. van Bael, T. S. Koh, Z. Shi, D. E. Savage, M. G. Lagally, R. Joynt, M. Friesen, S. N. Coppersmith, and M. A. Eriksson, "Tunable spin loading and T_1 of a silicon spin qubit measured by single-shot readout," *Phys. Rev. Lett.*, vol. 106, p. 156804, 2011.

[87] N. W. Ashcroft and N. D. Mermin, *Solid State Physics*. Thomson Learning, Inc., 1976.

[88] O. Prus, M. Reznikov, U. Sivan, and V. Pudalov, "Cooling of electrons in a silicon inversion layer," *Phys. Rev. Lett.*, vol. 88, p. 016801, Jan 2001.

[89] A. Bid, N. Ofek, M. Heiblum, V. Umansky, and D. Mahalu, "Shot noise and charge at the 2/3 composite fractional quantum hall state," *Phys. Rev. Lett.*, vol. 103, p. 236802, Dec 2009.

[90] D. Harbusch, D. Taubert, H. P. Tranitz, W. Wegscheider, and S. Ludwig, "Phonon-mediated versus coulombic backaction in quantum dot circuits," *Phys. Rev. Lett.*, vol. 104, p. 196801, May 2010.

[91] M. Kellogg, I. B. Spielman, J. P. Eisenstein, L. N. Pfeiffer, and K. W. West, "Observation of quantized hall drag in a strongly correlated bilayer electron system," *Phys. Rev. Lett.*, vol. 88, p. 126804, Mar 2002.

[92] A. Jauho and H. Smith, "Coulomb drag between parallel two-dimensional electron systems," *Phys. Rev. B*, vol. 47, no. 8, pp. 4420–4428, 1993.

[93] L. Zheng and A. H. MacDonald, "Coulomb drag between disordered two-dimensional electron-gas layers," *Phys. Rev. B*, vol. 48, pp. 8203–8209, Sep 1993.

[94] M. Fischetti and S. Laux, "Long-range coulomb interactions in small si devices. part i: Performance and reliability," *J. Appl. Phys.*, vol. 89, pp. 1205–1231, Jan 2001.

[95] M. Fischetti, "Long-range coulomb interactions in small si devices. part ii. effective electron mobility in thin-oxide structures," *J. Appl. Phys.*, vol. 89, pp. 1232–1250, Jan 2001.

[96] B. Laikhtman and P. Solomon, "Electron-drag effect in si metal-oxide-semiconductor devices with thin oxide layers," *Phys Rev B*, vol. 72, p. 125338, Jan 2005.

[97] M. Prunnila, S. J. Laakso, J. M. Kivioja, and J. Ahopelto, "Electrons and holes in si quantum well: A room-temperature transport and drag resistance study," *Appl. Phys. Lett.*, vol. 93, p. 112113, Jan 2008.

[98] K. Takashina, K. Nishiguchi, Y. Ono, A. Fujiwara, T. Fujisawa, Y. Hirayama, and K. Muraki, "Electrons and holes in a 40 nm thick silicon slab at cryogenic temperatures," *Appl. Phys. Lett.*, vol. 94, p. 142104, Jan 2009.

[99] A. Rojo, "Electron-drag effects in coupled electron systems," *J. Phys.: Condens. Mat.*, vol. 11, pp. R31–R52, 1999.

[100] B. K. Ridley, *Quantum Processes in Semiconductors.* Oxford Science Publications, fourth ed., 1999.

[101] V. Karpus, "Theoretical limit of mobility of two-dimensional electrons in gaas," *Semicond. Sci. Tech.*, vol. 5, pp. 691–694, Jan 1990.

[102] B. A. Glavin, V. A. Kochelap, T. L. Linnik, and K. W. Kim, "Electron-phonon interaction via the pekar mechanism in nanostructures," *Phys. Rev. B*, vol. 71, p. 081305, Feb 2005.

[103] J. H. Davies, *The Physics of Low-dimensional Semiconductors: An Introduction.* Cambridge University Press, 1997.

[104] S. D. Sarma and E. H. Hwang, "The so-called two dimensional metal-insulator transition," *Solid State Commun.*, vol. 135, no. 9-10, pp. 579–590, 2005.

[105] A. Gold, "Mobility of the non-polarized and spin-polarized electron gas in si/sige heterostructures: Remote impurities," *Europhys. Lett.*, vol. 92, p. 67002, 2010.

[106] I. I. Boiko and Y. M. Sirenko, "Scattering of two-dimensional electron gas on the semibounded three-dimensional electron gas," *Phys. Stat. Sol. (b)*, vol. 159, no. 2, pp. 805–816, 1990.

[107] A. I. Volokitin and B. N. J. Persson, "Near-field radiative heat transfer and noncontact friction," *Rev. Mod. Phys.*, vol. 79, pp. 1291–1329, Jan 2007.

[108] A. Volokitin and B. Persson, "Radiative heat transfer between nanostructures," *Phys. Rev. B*, vol. 63, p. 205404, Jan 2001.

[109] M. Krüger, T. Emig, and M. Kardar, "Non-equilibrium electromagnetic fluctuations: Heat transfer and interactions," *ArXiv e-prints*, Feb. 2011.

[110] K. C. Nowack, M. Shafiei, M. Laforest, G. E. D. K. Prawiroatmodjo, L. R. Schreiber, C. Reichl, W. Wegscheider, and L. M. K. Vandersypen, "Single-Shot Correlations and Two-Qubit Gate of Solid-State Spins," *Science*, vol. 333, pp. 1269–, Sept. 2011.

[111] B. M. Maune, M. G. Borselli, B. Huang, T. D. Ladd, P. W. Deelman, K. S. Holabird, A. A. Kiselev, I. Alvarado-Rodriguez, R. S. Ross, A. E. Schmitz, M. Sokolich, C. A. Watson, M. F. Gyure, and A. T. Hunter, "Coherent singlet-triplet oscillations in a silicon-based double quantum dot," *Nature*, vol. 481, pp. 344–347, 01 2012.

[112] M. Ciorga, A. S. Sachrajda, P. Hawrylak, C. Gould, P. Zawadzki, S. Jullian, Y. Feng, and Z. Wasilewski, "Addition spectrum of a lateral dot from Coulomb and spin-blockade spectroscopy," *Phys. Rev. B*, vol. 61, pp. R16315–R16318, Jun 2000.

[113] L. P. Kouwenhoven, D. G. Austing, and S. Tarucha, "Few-electron quantum dots," *Rep. Prog. Phys*, vol. 64, no. 6, pp. 701–736, 2001.

[114] J. M. Elzerman, R. Hanson, L. H. W. van Beveren, B. Witkamp, L. M. K. Vandersypen, and L. P. Kouwenhoven, "Single-shot read-out of an individual electron spin in a quantum dot," *Nature*, vol. 430, p. 431, 2004.

[115] F. H. L. Koppens, C. Buizert, K. J. Tielrooij, I. T. Vink, K. C. Nowack, T. Meunier, L. P. Kouwenhoven, and L. M. K. Vandersypen, "Driven coherent oscillations of a single electron spin in a quantum dot," *Nature*, vol. 442, pp. 766–771, Jan 2006.

[116] D. Brunner, B. D. Gerardot, P. A. Dalgarno, G. Wüst, K. Karrai, N. G. Stoltz, P. M. Petroff, and R. J. Warburton, "A coherent single-hole spin in a semiconductor," *Science*, vol. 325, no. 5936, pp. 70–72, 2009.

[117] A. Morello, J. Pla, F. Zwanenburg, K. Chan, K. Tan, H. Huebl, M. Mottonen, C. Nugroho, C. Yang, J. van Donkelaar, A. Alves, D. Jamieson, C. Escott, L. Hollenberg, R. Clark, and A. Dzurak, "Single-shot readout of an electron spin in silicon," *Nature*, vol. 467, pp. 687–691, Oct 2010.

[118] Y. Hu, F. Kuemmeth, C. M. Lieber, and C. M. Marcus, "Hole spin relaxation in ge-si core-shell nanowire qubits," *Nat Nano*, vol. 7, pp. 47–50, 01 2012.

[119] T. M. Godden, J. H. Quilter, A. J. Ramsay, Y. Wu, P. Brereton, I. J. Luxmoore, J. Puebla, A. M. Fox, and M. S. Skolnick, "Fast preparation of a single-hole spin in an inas/gaas quantum dot in a voigt-geometry magnetic field," *Phys. Rev. B*, vol. 85, p. 155310, Apr 2012.

[120] J. Levy, "Universal quantum computation with spin-1/2 pairs and Heisenberg exchange," *Phys. Rev. Lett.*, vol. 89, p. 147902, Jan 2002.

[121] J. R. Petta, A. C. Johnson, J. M. Taylor, E. A. Laird, A. Yacoby, M. D. Lukin, C. M. Marcus, M. P. Hanson, and A. C. Gossard, "Coherent manipulation of coupled electron spins in semiconductor quantum dots," *Science*, vol. 309, p. 2180, 2005.

[122] J. R. Petta, A. C. Johnson, A. Yacoby, C. M. Marcus, M. P. Hanson, and A. C. Gossard, "Pulsed-gate measurements of the singlet-triplet relaxation time in a two-electron double quantum dot," *Phys. Rev. B*, vol. 72, p. 161301, Jan 2005.

[123] J. R. Prance, Z. Shi, C. B. Simmons, D. E. Savage, M. G. Lagally, L. R. Schreiber, L. M. K. Vandersypen, M. Friesen, R. Joynt, S. N. Coppersmith, and M. A. Eriksson, "Single-shot measurement of triplet-singlet relaxation in a Si/SiGe double quantum dot," *Phys. Rev. Lett.*, vol. 108, p. 046808, Jan 2012.

[124] D. P. DiVincenzo, D. Bacon, J. Kempe, G. Burkard, and K. B. Whaley, "Universal quantum computation with the exchange interaction," *Nature*, vol. 408, p. 339, Nov 2000.

[125] L. Gaudreau, G. Granger, A. Kam, G. C. Aers, S. A. Studenikin, P. Zawadzki, M. Pioro-Ladrière, Z. R. Wasilewski, and A. S. Sachrajda, "Coherent control of three-spin states in a triple quantum dot," *Nature Physics*, vol. 8, pp. 54–58, Jan. 2012.

[126] T. Hayashi, T. Fujisawa, H. D. Cheong, Y. H. Jeong, and Y. Hirayama, "Coherent manipulation of electronic states in a double quantum dot," *Phys. Rev. Lett.*, vol. 91, p. 226804, Nov 2003.

[127] K. D. Petersson, J. R. Petta, H. Lu, and A. C. Gossard, "Quantum coherence in a one-electron semiconductor charge qubit," *Phys. Rev. Lett.*, vol. 105, p. 246804, Dec 2010.

[128] H. Bluhm, S. Foletti, I. Neder, M. Rudner, D. Mahalu, V. Umansky, and A. Yacoby, "Dephasing time of GaAs electron-spin qubits coupled to a nuclear bath exceeding 200μs," *Nature Physics*, vol. 7, pp. 109–113, Feb. 2011.

[129] W. A. Coish and D. Loss, "Singlet-triplet decoherence due to nuclear spins in a double quantum dot," *Phys. Rev. B*, vol. 72, p. 125337, Sep 2005.

[130] X. Hu and S. Das Sarma, "Charge-fluctuation-induced dephasing of exchange-coupled spin qubits," *Phys. Rev. Lett.*, vol. 96, p. 100501, Mar 2006.

[131] D. Culcer, X. Hu, and S. D. Sarma, "Dephasing of si spin qubits due to charge noise," *Appl. Phys. Lett.*, vol. 95, p. 073102, 2009.

[132] X. Hu, "Two-spin dephasing by electron-phonon interaction in semiconductor double quantum dots," *Phys. Rev. B*, vol. 83, p. 165322, 2011.

[133] T. B. Boykin, G. Klimeck, M. A. Eriksson, M. Friesen, S. N. Coppersmith, P. von Allmen, F. Oyafuso, and S. Lee, "Valley splitting in strained silicon quantum wells," *Appl. Phys. Lett.*, vol. 85, p. 115, 2004.

[134] T. B. Boykin, G. Klimeck, M. Friesen, S. N. Coppersmith, P. V. Allmen, F. Oyafuso, and S. Lee, "Valley splitting in low-density quantum-confined heterostructures studied using tight-binding models," *Phys. Rev. B*, vol. 70, p. 165325, Jan 2004.

[135] D. Culcer, L. Cywinski, Q. Z. Li, X. Hu, and S. Das Sarma, "Realizing singlet-triplet qubits in multivalley Si quantum dots," *Phys. Rev. B*, vol. 80, p. 205302, 2009.

[136] M. Friesen, M. A. Eriksson, and S. N. Coppersmith, "Magnetic field dependence of valley splitting in realistic Si/SiGe quantum wells," *Appl. Phys. Lett.*, vol. 89, p. 202106, 2006.

[137] M. Friesen, S. Chutia, C. Tahan, and S. N. Coppersmith, "Valley splitting theory of SiGe/Si/SiGe quantum wells," *Phys. Rev. B*, vol. 75, p. 115318, 2007.

[138] M. Friesen and S. N. Coppersmith, "Theory of valley-orbit coupling in a Si/SiGe quantum dot," *Phys. Rev. B*, vol. 81, p. 115324, 2010.

[139] A. L. Saraiva, M. J. Calderon, X. Hu, S. Das Sarma, and B. Koiller, "Physical mechanisms of interface-mediated intervalley coupling in Si," *Phys. Rev. B*, vol. 80, p. 081305(R), 2009.

[140] A. L. Saraiva, M. J. Calderón, R. B. Capaz, X. Hu, S. Das Sarma, and B. Koiller, "Intervalley coupling for interface-bound electrons in silicon: An effective mass study," *Phys. Rev. B*, vol. 84, p. 155320, Oct 2011.

[141] V. N. Golovach, A. Khaetskii, and D. Loss, "Spin relaxation at the singlet-triplet crossing in a quantum dot," *Phys. Rev. B*, vol. 77, p. 045328, Jan 2008.

[142] M. Prada, R. H. Blick, and R. Joynt, "Singlet-triplet relaxation in two-electron silicon quantum dots," *Phys. Rev. B*, vol. 77, p. 115438, Mar 2008.

[143] R. Hanson, L. H. W. van Beveren, I. T. Vink, J. M. Elzerman, W. J. M. Naber, F. H. L. Koppens, L. P. Kouwenhoven, and L. M. K. Vandersypen, "Single-shot readout of electron spin states in a quantum dot using spin-dependent tunnel rates," *Phys. Rev. Lett.*, vol. 94, p. 196802, Jan 2005.

[144] D. M. Wood and A. Zunger, "Successes and failures of the $\mathbf{k} \cdot \mathbf{p}$ method: A direct assessment for gaas/alas quantum structures," *Phys. Rev. B*, vol. 53, pp. 7949–7963, Mar 1996.

[145] G. Mahan, *Many-particle physics*. Physics of solids and liquids, Kluwer Academic/Plenum Publishers, 2000.

[146] M. Lundstrom, *Fundamentals of carrier transport*. Cambridge University Press, second ed., 2000.

[147] H. J. Maris and S. Tamura, "Propagation of acoustic phonon solitons in nonmetallic crystals," *Phys. Rev. B*, vol. 84, p. 024301, Jul 2011.

[148] H. J. Maris Private communication.

[149] H.-Y. Hao and H. J. Maris, "Dispersion of the long-wavelength phonons in ge, si, gaas, quartz, and sapphire," *Phys. Rev. B*, vol. 63, p. 224301, May 2001.

[150] B. C. Daly, K. Kang, Y. Wang, and D. G. Cahill, "Picosecond ultrasonic measurements of attenuation of longitudinal acoustic phonons in silicon," *Phys. Rev. B*, vol. 80, p. 174112, Nov 2009.

[151] D. von der Linde, J. Kuhl, and H. Klingenberg, "Raman scattering from nonequilibrium lo phonons with picosecond resolution," *Phys. Rev. Lett.*, vol. 44, pp. 1505–1508, Jun 1980.

[152] D. K. Ferry, "First-order optical and intervalley scattering in semiconductors," *Phys. Rev. B*, vol. 14, pp. 1605–1609, Aug 1976.

[153] J. A. Rowlette and K. E. Goodson, "Fully Coupled Nonequilibrium Electron-Phonon Transport in Nanometer-Scale Silicon FETs," *IEEE Transactions on Electron Devices*, vol. 55, pp. 220–232, Jan. 2008.

[154] G. Ramon and X. Hu, "Decoherence of spin qubits due to a nearby charge fluctuator in gate-defined double dots," *Phys. Rev. B*, vol. 81, p. 045304, Jan 2010.

[155] J. D. Jackson, *Classical Electrodynamics*. Wiley, 3rd ed., 1998.

[156] O. Astafiev, Y. A. Pashkin, Y. Nakamura, T. Yamamoto, and J. S. Tsai, "Quantum noise in the josephson charge qubit," *Phys. Rev. Lett.*, vol. 93, p. 267007, Dec 2004.

[157] M. Thalakulam, C. B. Simmons, B. M. Rosemeyer, D. E. Savage, M. G. Lagally, M. Friesen, S. N. Coppersmith, and M. A. Eriksson, "Fast tunnel rates in Si/SiGe one-electron single and double quantum dots," *Appl. Phys. Lett.*, vol. 96, p. 183104, 2010.

[158] M. Thalakulam, C. B. Simmons, B. J. Van Bael, B. M. Rosemeyer, D. E. Savage, M. G. Lagally, M. Friesen, S. N. Coppersmith, and M. A. Eriksson, "Single-shot measurement and tunnel-rate spectroscopy of a si/sige few-electron quantum dot," *Phys. Rev. B*, vol. 84, p. 045307, Jul 2011.

[159] D. Culcer, A. L. Saraiva, B. Koiller, X. Hu, and S. Das Sarma, "Valley-based noise-resistant quantum computation using si quantum dots," *Phys. Rev. Lett.*, vol. 108, p. 126804, Mar 2012.

[160] Y. Hu, H. O. H. Churchill, D. J. Reilly, J. Xiang, C. M. Lieber, and C. M. Marcus, "A Ge/Si heterostructure nanowire-based double quantum dot with integrated charge sensor," *Nat. Nanotechnol.*, vol. 2, pp. 622–625, Jan 2007.

[161] A. Zinov'eva, A. Nenashev, and A. Dvurechenskii, "Hole spin relaxation in ge quantum dots," *JETP Letters*, vol. 82, pp. 302–305, 2005. 10.1134/1.2130917.

[162] M. V. Fischetti and S. E. Laux, "Band structure, deformation potentials, and carrier mobility in strained si, ge, and sige alloys," *Journal of Applied Physics*, vol. 80, no. 4, pp. 2234–2252, 1996.

[163] M. Xiao, M. G. House, and H. W. Jiang, "Measurement of the spin relaxation time of single electrons in a silicon metal-oxide-semiconductor-based quantum dot," *Phys. Rev. Lett.*, vol. 104, p. 096801, 2010.

[164] R. R. Hayes, A. A. Kiselev, M. G. Borselli, S. S. Bui, E. T. Croke III, P. W. Deelman, B. M. Maune, I. Milosavljevic, J.-S. Moon, R. S. Ross, A. E. Schmitz, M. F. Gyure,

and A. T. Hunter, "Lifetime measurements (T1) of electron spins in Si/SiGe quantum dots," 2009. Preprint at http://arxiv.org/abs/0908.0173.

[165] A. M. Tyryshkin, S. Tojo, J. J. L. Morton, H. Riemann, N. V. Abrosimov, P. Becker, H.-J. Pohl, T. Schenkel, M. L. W. Thewalt, K. M. Itoh, and S. A. Lyon, "Electron spin coherence exceeding seconds in high-purity silicon," *Nat. Mater.*, vol. advance online publication, pp. –, 12 2011.

[166] N. M. Zimmerman, B. J. Simonds, A. Fujiwara, Y. Ono, Y. Takahashi, and H. Inokawa, "Charge offset stability in tunable-barrier Si single-electron tunneling devices," *Appl. Phys. Lett.*, vol. 90, p. 033507, Jan 2007.

[167] C. B. Simmons, M. Thalakulam, B. M. Rosemeyer, B. J. van Bael, E. K. Sackmann, D. E. Savage, M. G. Lagally, R. Joynt, M. Friesen, S. N. Coppersmith, and M. A. Eriksson, "Charge sensing and controllable tunnel coupling in a Si/SiGe double quantum dot," *Nano Lett.*, vol. 9, p. 3234, 2009.

[168] L. A. Tracy, E. P. Nordberg, R. W. Young, C. B. Pinilla, H. L. Stalford, G. A. T. Eyck, K. Eng, K. D. Childs, J. R. Wendt, R. K. Grubbs, J. Stevens, M. P. Lilly, M. A. Eriksson, and M. S. Carroll, "Double quantum dot with tunable coupling in an enhancement-mode silicon metal-oxide semiconductor device with lateral geometry," *Appl. Phys. Lett.*, vol. 97, p. 192110, 2010.

[169] K. A. Slinker, K. L. M. Lewis, C. C. Haselby, S. Goswami, L. J. Klein, J. O. Chu, S. N. Coppersmith, R. Joynt, R. H. Blick, M. Friesen, and M. A. Eriksson, "Quantum dots in Si/SiGe 2DEGs with Schottky top-gated leads," *New J. Phys.*, vol. 7, p. 246, Jan 2005.

[170] T. Berer, D. Pachinger, G. Pillwein, M. Mühlberger, H. Lichtenberger, G. Brunthaler, and F. Schäffler, "Lateral quantum dots in Si/SiGe realized by a Schottky split-gate technique," *Appl. Phys. Lett.*, vol. 88, p. 162112, Jan 2006.

[171] S. J. Angus, A. J. Ferguson, A. S. Dzurak, and R. G. Clark, "Gate-defined quantum dots in intrinsic silicon," *Nano Lett.*, vol. 7, pp. 2051–2055, Jan 2007.

[172] E. P. Nordberg, H. L. Stalford, R. Young, G. A. T. Eyck, K. Eng, L. A. Tracy, K. D. Childs, J. R. Wendt, R. K. Grubbs, J. Stevens, M. P. Lilly, M. A. Eriksson, and M. S. Carroll, "Charge sensing in enhancement mode double-top-gated metal-oxide-semiconductor quantum dots," *Appl. Phys. Lett.*, vol. 95, p. 202102, 2009.

[173] M. Xiao, M. G. House, and H. W. Jiang, "Parallel spin filling and energy spectroscopy in few-electron si metal-on-semiconductor-based quantum dots," *Applied Physics Letters*, vol. 97, no. 3, p. 032103, 2010.

[174] S. Goswami, K. A. Slinker, M. Friesen, L. M. McGuire, J. L. Truitt, C. Tahan, L. J. Klein, J. O. Chu, P. M. Mooney, D. W. van der Weide, R. Joynt, S. N. Coppersmith, and M. A. Eriksson, "Controllable valley splitting in silicon quantum devices," *Nat. Phys.*, vol. 3, pp. 41–45, 2007.

[175] M. G. Borselli, R. S. Ross, A. A. Kiselev, E. T. Croke, K. S. Holabird, P. W. Deelman, L. D. Warren, I. Alvarado-Rodriguez, I. Milosavljevic, F. C. Ku, W. S. Wong, A. E. Schmitz, M. Sokolich, M. F. Gyure, and A. T. Hunter, "Measurement of valley splitting in high-symmetry si/sige quantum dots," *Appl Phys Lett*, vol. 98, p. 123118, Jan 2011.

[176] W. H. Lim, C. H. Yang, F. A. Zwanenburg, and A. S. Dzurak, "Spin filling of valley–orbit states in a silicon quantum dot," *Nanotechnology*, vol. 22, no. 33, p. 335704, 2011.

[177] N. Shaji, C. B. Simmons, M. Thalakulam, L. J. Klein, H. Qin, H. Luo, D. E. Savage, M. G. Lagally, A. J. Rimberg, R. Joynt, M. Friesen, R. H. Blick, S. N. Coppersmith, and M. A. Eriksson, "Spin blockade and lifetime-enhanced transport in a few-electron Si/SiGe double quantum dot," *Nature Physics*, vol. 4, p. 540, 2008.

[178] H. W. Liu, T. Fujisawa, Y. Ono, H. Inokawa, A. Fujiwara, K. Takashina, and Y. Hirayama, "Pauli-spin-blockade transport through a silicon double quantum dot," *Phys. Rev. B*, vol. 77, p. 073310, Jan 2008.

[179] J. Kyriakidis, M. Pioro-Ladriere, M. Ciorga, A. S. Sachrajda, and P. Hawrylak, "Voltage-tunable singlet-triplet transition in lateral quantum dots," *Phys. Rev. B*, vol. 66, p. 035320, Jul 2002.

[180] S. Amasha, K. MacLean, I. P. Radu, D. M. Zumbuehl, M. A. Kastner, M. P. Hanson, and A. C. Gossard, "Electrical control of spin relaxation in a quantum dot," *Phys. Rev. Lett.*, vol. 100, no. 4, p. 046803, 2008.

[181] C. B. Simmons, M. Thalakulam, N. Shaji, L. J. Klein, H. Qin, R. H. Blick, D. E. Savage, M. G. Lagally, S. N. Coppersmith, and M. A. Eriksson, "Single-electron quantum dot in Si/SiGe with integrated charge sensing," *Appl. Phys. Lett.*, vol. 91, p. 213103, 2007.

[182] Y. Hada and M. Eto, "Electronic states in silicon quantum dots: Multivalley artificial atoms," *Phys. Rev. B*, vol. 68, p. 155322, Oct 2003.

[183] J. M. Elzerman, R. Hanson, L. H. W. van Beveren, L. M. K. Vandersypen, and L. P. Kouwenhoven, "Excited-state spectroscopy on a nearly closed quantum dot via charge detection," *Appl. Phys. Lett.*, vol. 84, pp. 4617–4619, Jan 2004.

[184] R. Hanson, L. P. Kouwenhoven, J. R. Petta, S. Tarucha, and L. M. K. Vandersypen, "Spins in few-electron quantum dots," *Rev. Mod. Phys.*, vol. 79, pp. 1217–1265, Jan 2007.

[185] F. A. Baron, *PhD Thesis*. PhD thesis, UCLA, 2006.

[186] D. Culcer, X. Hu, and S. Das Sarma, "Interface roughness, valley-orbit coupling, and valley manipulation in quantum dots," *Phys. Rev. B*, vol. 82, p. 205315, 2010.

[187] A. L. Saraiva, B. Koiller, and M. Friesen, "Extended interface states enhance valley splitting in si/sio$_2$," *Phys. Rev. B*, vol. 82, p. 245314, 2010.

[188] M. D. Shulman, O. E. Dial, S. P. Harvey, H. Bluhm, V. Umansky, and A. Yacoby, "Demonstration of entanglement of electrostatically coupled singlet-triplet qubits," *Science*, vol. 336, p. 202, 2012.

[189] Z. Shi, C. B. Simmons, D. R. Ward, J. R. Prance, T. S. Koh, J. K. Gamble, X. Wu, D. E. Savage, M. G. Lagally, M. Friesen, S. N. Coppersmith, and M. A. Eriksson, "Coherent quantum oscillations in a silicon charge qubit." Preprint at http://arxiv.org/abs/1208.0519.

[190] F. A. Zwanenburg, A. S. Dzurak, A. Morello, M. Y. Simmons, L. C. L. Hollenberg, G. Klimeck, S. Rogge, S. N. Coppersmith, and M. A. Eriksson, "Silicon quantum electronics." Preprint at http://arxiv.org/abs/1206.5202.

[191] M. A. Eriksson, M. Friesen, S. N. Coppersmith, R. Joynt, L. J. Klein, K. A. Slinker, C. Tahan, P. M. Mooney, J. O. Chu, and S. J. Koester, "Spin-based quantum dot quantum computing in silicon," *Quantum Information Processing*, vol. 3, pp. 133–146, Feb 2004.

[192] V. N. Smelyanskiy, A. G. Petukhov, and V. V. Osipov, "Quantum computing on long-lived donor states of li in si," *Phys. Rev. B*, vol. 72, p. 081304, Aug 2005.

[193] A. Baena, A. L. Saraiva, B. Koiller, and M. J. Calderón, "Impact of the valley degree of freedom on the control of donor electrons near a si/sio$_2$ interface," *Phys. Rev. B*, vol. 86, p. 035317, Jul 2012.

[194] S.-y. Shiau, S. Chutia, and R. Joynt, "Valley kondo effect in silicon quantum dots," *Phys. Rev. B*, vol. 75, p. 195345, May 2007.

[195] K. Takashina, Y. Ono, A. Fujiwara, Y. Takahashi, and Y. Hirayama, "Valley polarization in Si(100) at zero magnetic field," *Phys. Rev. Lett.*, vol. 96, p. 236801, Jun 2006.

[196] C. H. Yang, A. Rossi, R. Ruskov, N. S. Lai, F. A. Mohiyaddin, S. Lee, C. Tahan, G. Klimeck, A. Morello, and A. S. Dzurak, "Spin-valley lifetimes in a silicon quantum dot with tunable valley splitting." arXiv:1302.0983, 2013.

[197] E. Nielsen, R. Rahman, and R. P. Muller, "A many-electron tight binding method for the analysis of quantum dot systems," *Journal of Applied Physics*, vol. 112, no. 11, p. 114304, 2012.

[198] N. Kharche, M. Prada, T. B. Boykin, and G. Klimeck, "Valley splitting in strained silicon quantum wells modeled with 2 ° miscuts, step disorder, and alloy disorder," *Appl. Phys. Lett.*, vol. 90, p. 092109, Jan 2007.

[199] S. Ahmed, N. Kharche, R. Rahman, M. Usman, S. Lee, H. Ryu, H. Bae, S. Clark, B. Haley, M. Naumov, F. Saied, M. Korkusinski, R. Kennel, M. McLennan, T. B. Boykin, and G. Klimeck, "Multimillion atom simulations with NEMO 3-D," 2009.

[200] P. Evans, D. Savage, J. R. Prance, C. B. Simmons, M. G. Lagally, S. N. Coppersmith, M. A. Eriksson, and T. U. Schülli, "Nanoscale distortions of Si quantum wells in Si/SiGe quantum-electronic heterostructures," *Advanced Materials*, vol. 24, pp. 5217–5221, 2012.

[201] A. Tucker, *Applied Combinatorics*. John Wiley & Sons, 4 ed., 2004.

[202] F. C. Auluck, "On partitions of bipartite numbers," *Mathematical Proceedings of the Cambridge Philosophical Society*, vol. 49, no. 1, p. 72, 1953.

[203] C. L. Liu, *Introduction to Combinatorial Mathematics*. McGraw-Hill, 1968.

[204] A. Barabási, R. Albert, and H. Jeong, "Mean-field theory for scale-free random networks," *Physica A*, vol. 272, pp. 173–187, 1999.

[205] F. Schaffler, "High-mobility si and ge structures," *Semicond. Sci. Tech.*, vol. 12, pp. 1515–1549, Jan 1997.